

# Investigation of the secondary electron emission characteristics of the KATRIN main spectrometer

Masterarbeit  
von

**Axel Müller**

An der Fakultät für Physik  
Institut für Experimentelle Kernphysik (IEKP)

Erstgutachter:	Prof. Dr. Guido Drexlin
Zweitgutachter:	Prof. Dr. Ulrich Husemann
Betreuender Mitarbeiter:	Dr. Fabian Harms

Bearbeitungszeit: 01. Juni 2015 – 31. Mai 2016



---

Ich versichere wahrheitsgemäß, die Arbeit selbstständig angefertigt, alle benutzten Hilfsmittel vollständig und genau angegeben und alles kenntlich gemacht zu haben, was aus Arbeiten anderer unverändert oder mit Abänderungen entnommen wurde.

**Karlsruhe, 31.05.2016**

**Axel Müller**



# Contents

<b>1</b>	<b>Introduction</b>	<b>1</b>
<b>2</b>	<b>Neutrinos</b>	<b>3</b>
2.1	Neutrino physics - a historical overview . . . . .	3
2.2	Neutrinos in the standard model of particle physics . . . . .	4
2.3	The phenomenon of neutrino flavor oscillation . . . . .	5
2.3.1	The solar neutrino deficit . . . . .	5
2.3.2	The theory of neutrino oscillation . . . . .	6
2.3.3	Neutrino oscillation experiments . . . . .	7
2.4	Experimental approaches to measure the neutrino rest mass . . . . .	9
<b>3</b>	<b>The KATRIN Experiment</b>	<b>13</b>
3.1	The measurement principle . . . . .	13
3.2	The experimental setup . . . . .	15
3.2.1	Tritium source . . . . .	15
3.2.2	Transport section . . . . .	16
3.2.3	Spectrometers . . . . .	16
3.2.4	Focal-Plane detector system . . . . .	17
3.3	The sensitivity of KATRIN . . . . .	18
<b>4</b>	<b>The spectrometer and detector section</b>	<b>21</b>
4.1	Vacuum . . . . .	21
4.2	Magnets . . . . .	22
4.3	High-voltage concept . . . . .	24
4.4	Detector and data acquisition . . . . .	25
<b>5</b>	<b>The background model for the main spectrometer</b>	<b>29</b>
5.1	Stored-particle induced background . . . . .	29
5.1.1	Penning traps . . . . .	29
5.1.2	Magnetically stored particles . . . . .	30
5.1.3	The radioactive decay of radon in the spectrometer . . . . .	32
5.1.4	Radon reduction by a LN <sub>2</sub> -cooled baffle system . . . . .	32
5.2	Characteristics of the non radon-induced background . . . . .	33
5.2.1	Impact of the magnetic shielding . . . . .	33
5.2.2	Impact of the electrostatic shielding . . . . .	33
5.2.3	Impact of a vacuum bake-out . . . . .	35
5.3	The Rydberg background model . . . . .	36
<b>6</b>	<b>Characteristics of secondary electron emission</b>	<b>39</b>
6.1	Measurement principle . . . . .	39
6.2	Spatial distribution of the secondary electrons . . . . .	41
6.3	Spectrometer potential dependence on the secondary electron rate . . . . .	43
6.4	IE dependence on the secondary electron rate . . . . .	44

6.5	Time correlation in secondary electron emission . . . . .	45
6.5.1	Identification of time correlated events . . . . .	45
6.5.2	Axial distribution of single and cluster events in the spectrometer . . . . .	47
6.6	Identification of spatially correlated patterns . . . . .	48
6.6.1	Efficiency of the pattern identification algorithm . . . . .	49
<b>7</b>	<b>Possible generation mechanisms of Rydberg atoms on the main spectrometer surfaces</b>	<b>51</b>
7.1	Cosmic muons . . . . .	52
7.2	Environmental $\gamma$ -radiation . . . . .	54
7.2.1	Attenuation of $\gamma$ -photons using a water shield . . . . .	54
7.2.2	Measurements with an $^{60}\text{Co}$ -source . . . . .	55
7.3	Intrinsic radiation . . . . .	58
7.3.1	Deposited radioactive atoms in the main spectrometer . . . . .	58
7.3.2	Temporal characteristics of large clusters . . . . .	59
7.3.3	Spatial characteristics of large clusters . . . . .	60
7.3.4	Identification of the cluster creating mechanism . . . . .	62
<b>8</b>	<b>Conclusion</b>	<b>67</b>
	<b>List of Figures</b>	<b>69</b>
	<b>List of Tables</b>	<b>71</b>
	<b>Bibliography</b>	<b>73</b>

# 1. Introduction

With the observation of neutrino flavor oscillations, experiments like SNO or Super-Kamiokande found the evidence for a non-vanishing rest mass for at least two of the three neutrino families in contradiction to the standard model of particle physics. Especially for particle physics and cosmology the absolute mass scale of the neutrino has broad implications and for this reason numerous experiments with a variety of concepts are being developed with the aim to determine this crucial parameter.

The Karlsruhe TRItium Neutrino (KATRIN) experiment aims to determine the rest mass of the electron antineutrino in a model-independent way by analyzing the kinetic energy of electrons from the tritium  $\beta$ -decay. With a sensitivity of  $m_{\bar{\nu}} \leq 200 \text{ meV}/c^2$  KATRIN improves this measurement technique by one order of magnitude compared to previous experiments. The experiment combines a high-luminosity windowless gaseous tritium source with a large-scale integrating spectrometer, based on the MAC-E filter principle.

Despite the very high electron rate from the source, only a small amount of the signal electrons has kinetic energies in the end point region of the tritium  $\beta$ -spectrum close to 18.6 keV, at which point a non-zero neutrino mass observably changes the spectral shape. In order to achieve the ambitious sensitivity on the measurement of the neutrino mass, the KATRIN experiment relies on a background level of 10 mcps. With its large dimensions the stainless-steel vessel of the main spectrometer is a major contributor to the background processes in the experiment. Although several background sources have been identified, and partly eliminated, there are still background signals with distinct characteristics observable. The major task of this thesis was to identify the potential creation mechanism of this remaining background.

## Outline

In chapter 2 of this thesis, the historical development of neutrino physics is presented with the postulation and detection of neutrinos until the 1950s and the observation of neutrino flavor oscillation at the end of the 20th century. Subsequently, the theoretical aspects of the neutrino flavor oscillation and the impact on the neutrino characteristics are explained before an overview of the experimental approaches to determine the neutrino mass is given.

Chapter 3 gives an overview of the measurement principle and the setup of the entire KATRIN experiment, followed by a determination of the sensitivity on the neutrino mass. In chapter 4 the specific components of the main spectrometer are explained in more detail as they have a huge impact on the measurements, performed within the context of this thesis.

The focus of chapter 5 is on the background produced by stored particles, which is strongly connected to radon isotopes in the spectrometer vessel. In the following section the characteristics of the non-radon induced background are explained. As the source for this background is not yet identified, a background model based on the hypothesis of Rydberg atoms is established, to explain this novel source of background.

In chapter 6 the measurements to detect secondary electrons from the spectrometer surfaces are explained. It is supposed that these electrons accompany the emission of Rydberg atoms, and since the latter could not yet be observed directly, the electron characteristics are used to get a better understanding on the production mechanism of the Rydberg atoms.

In chapter 7 potential sources of the secondary electrons from the inner spectrometer surfaces and thus, the Rydberg atoms, are investigated. For this purpose sophisticated measurements were performed, which are described in detail, and the results are compared to the given secondary electron signal.

Chapter 8 concludes this thesis with a detailed summary of the results of this work.

## 2. Neutrinos

In this chapter a short historical overview of the postulation and detection of neutrinos is given in section 2.1, followed by the classification in the standard model of particle physics in section 2.2. In section 2.3 the observation and theoretical description of neutrino oscillation is described, which gave the first evidence for massive neutrinos. Finally, in section 2.4 different approaches to determine the mass of neutrinos are presented.

### 2.1 Neutrino physics - a historical overview

At the beginning of the 20th century three forms of radioactivity were discovered:  $\alpha$ -  $\beta$ - and  $\gamma$ -radiation [1]. According to the observations for  $\alpha$ -radiation, the energy spectrum of the  $\beta$ -decay was assumed to have characteristic discrete values, depending on the respective element. In 1914, J. Chadwick investigated the  $\beta$ -decay of radium, using a Geiger-Mueller counter, and found a continuous spectrum for the kinetic energy of the emitted particle [2]. At this time the result was a contradiction to the state of science, as the  $\beta$ -decay was supposed to be a two-body process, not allowing a continuous energy spectrum and thus, violating the fundamental laws of energy and momentum conservation.

In 1930, W. Pauli proposed a new particle, emitted during the  $\beta$ -decay together with the electron, making it a three-body process:



This extension by an electrically neutral, spin- $\frac{1}{2}$  particle solved the problem with the continuous energy spectrum of the emitted electron, as a part of the discrete decay energy is shared by the proposed particle. Pauli estimated the mass of the particle, which he called "neutron", to be smaller than 1 % of the proton mass [3].

In 1932, Chadwick discovered the neutron, as it is known today [4], but it is much too heavy to be the sought particle. Two years later, E. Fermi postulated the theory of the three-body process of the  $\beta$ -decay as a point-like weak interaction, involving four fermions:



Fermi named the particle "neutrino", today, in this context, known as antineutrino [5]. In the same year the interaction cross-section of a MeV-scale neutrino with a nucleus was

calculated by H. Bethe and J. Peierls to be  $\sigma < 1 \cdot 10^{-44} \text{ cm}^2$ , corresponding to a range of  $10^{16} \text{ km}$  in solid matter [6]. This very small cross-section led them to the assumption that neutrinos, created in nuclear transformations, would be impossible to be observed.

This statement has been true for almost twenty years, until C.L. Cowan and F. Reines started their "Project Poltergeist" in 1951, with the aim to detect antineutrinos from nuclear fission reactors. Therefore, they planned to observe the inverse  $\beta$ -decay of an antineutrino and a proton to a neutron and a positron:



The target was a large tank filled with 200l of water and 40 kg of cadmium chloride, which provided the protons needed for the reaction. Both products respectively induced  $\gamma$ -photons with characteristic energies. The generated positrons very quickly annihilated with an electron to pairs of photons with energies of 511 keV. The neutrons were absorbed by cadmium nuclei, after the neutron lost energy due to thermalization in the water. The consequently excited cadmium nucleus emitted  $\gamma$ -photons in the MeV-range. This reaction is relatively slow (a few  $\mu\text{s}$ ), compared to the annihilation of the positrons, allowing to use a delayed coincidence measurement in order to discriminate background signals from the reactor and the atmosphere. In 1956, the observation of the free electron antineutrino could be claimed with the Savannah River Experiment, confirming the theoretically predicted cross section [7].

Six years later, in 1962, the second neutrino flavor, the  $\nu_\mu$ , was detected at Brookhaven National Laboratory, in the decay of pions. The pions were a product of the collision of 15 GeV protons on a beryllium target. By blocking all other particles, created in the fixed target experiment, it was ensured that only neutrinos could reach the spark chamber detector. It could be shown, that only muons were generated in the reactions in the detector, which means that  $\nu_\mu$  and  $\nu_e$  are non-identical particles [8].

In 2001, 25 years after the detection of the  $\tau$ -lepton, the third neutrino flavor was detected with a similar experiment as in Brookhaven. Again the decay of a meson, here the  $D_S$ -meson, which was generated by the collision of high energy protons with a tungsten target, was investigated and all products of the collision were isolated from the detector volume by large iron and lead shields, except the neutrinos. In the detector material, the  $\nu_\tau$  created  $\tau$ -leptons, indicated by a characteristic kink and path length. Although only 4  $\nu_\tau$  were detected, the significance for the detection of the third generation neutrino is unambiguous, due to the very low background signal [9].

## 2.2 Neutrinos in the standard model of particle physics

Due to the scientific achievements during the 20th century it was possible to establish the standard model of particle physics, explaining the composition and interaction of the elementary particles in the universe. It consists of 12 fermions, separated in three generations, four gauge bosons and the Higgs boson. The three fermionic generations respectively consist of two quarks, one with charge  $+\frac{2}{3}$  and one with charge  $-\frac{1}{3}$ , and two leptons, one with charge  $-1$  and the respective neutrino which is electrically neutral. For each of these fermions, an anti-particle exists with the opposite sign in charge. The four gauge bosons represent the strong, weak and electromagnetic interactions of the particles. The Higgs boson, discovered in 2012 at LHC, is the quantum excitation of the Higgs field, an explanation for the elementary particles to be massive [10]. Although the model describes processes and properties of matter and antimatter correctly, some extensions are

necessary, as it cannot cover all discoveries and phenomena, like neutrinos being massive [11].

In the standard model of particle physics neutrinos only react in weak interactions, mediated by the  $W^\pm$ - and  $Z^0$ -bosons. As the  $W^\pm$ - bosons only couple to left-handed fermions and right-handed anti-fermions, in experiments only neutrinos and anti-neutrinos with the respective helicity are detected. The resulting maximum parity violation of weak interactions confirms the existence of massless left-handed antineutrinos and massless right-handed neutrinos only [12]. From the observation of the decay of  $Z^0$ -bosons, produced at collider experiments the total number of light neutrino species can be deduced. This is possible by comparing the width of the  $Z^0$  resonance with the theoretically predicted widths for each lepton generation. For light and only weak interacting neutrinos, according to the standard model, the number of neutrino types was found to be  $N_\nu = 2.984 \pm 0.008$  [13]. Therefore, in the standard model of particles, neutrinos are neutral and massless spin- $\frac{1}{2}$  particles which exist in three different flavors.

## 2.3 The phenomenon of neutrino flavor oscillation

In 1957, B. Pontecorvo proposed the idea of neutrino oscillation, based on the observations for the oscillation of neutral kaons between two states:  $K^0 \leftrightarrow \bar{K}^0$ . As neutrinos also carry no charge he had the idea of the oscillation between neutrinos and anti-neutrinos [14]. However, the oscillation of particle states requires them to be massive and to violate the lepton number conservation, which was a big contradiction for neutrinos at that time.

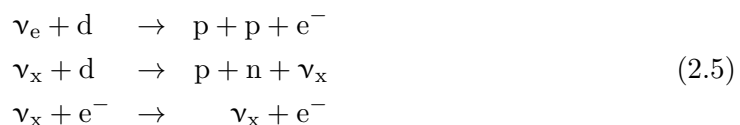
### 2.3.1 The solar neutrino deficit

In 1964, the standard solar model (SSM) was published by J. Bahcall, in order to explain the several fusion processes in the sun [15]. Due to their very small interaction cross sections solar electron-neutrinos were considered to be the ideal particles to investigate the processes in the core of the sun, as they are the only produced particles with a mean free path larger than the dimensions of the star. In the sun there are several processes creating electron-neutrinos. The most dominant one is:



The total energy spectrum of solar neutrinos, expected to be observed on the earth, can be seen in Fig. 2.1. In the same year the SSM was published, R. Davis proposed the Homestake experiment to measure the solar electron-neutrino flux, via the inverse  $\beta$ -decay of chloride, transforming it to argon [16]. The energy threshold of this reaction limited the observations to processes in the sun creating neutrinos with energies larger than 814 keV. The results of the experiment showed a significant deficit of about 30% in the electron neutrino rate from the sun, compared to the predicted value of the SSM. In the following years the energy threshold could be lowered by using other detector materials, however, the solar electron neutrino deficit was also observed for the other neutrino creating processes in the sun [17].

In 2001, the solar neutrino deficit could be resolved by the Sudbury Neutrino Observation (SNO) experiment. The detection of solar  ${}^8\text{B}$  neutrinos is based on the interactions with deuterium, provided by heavy water as detector material:



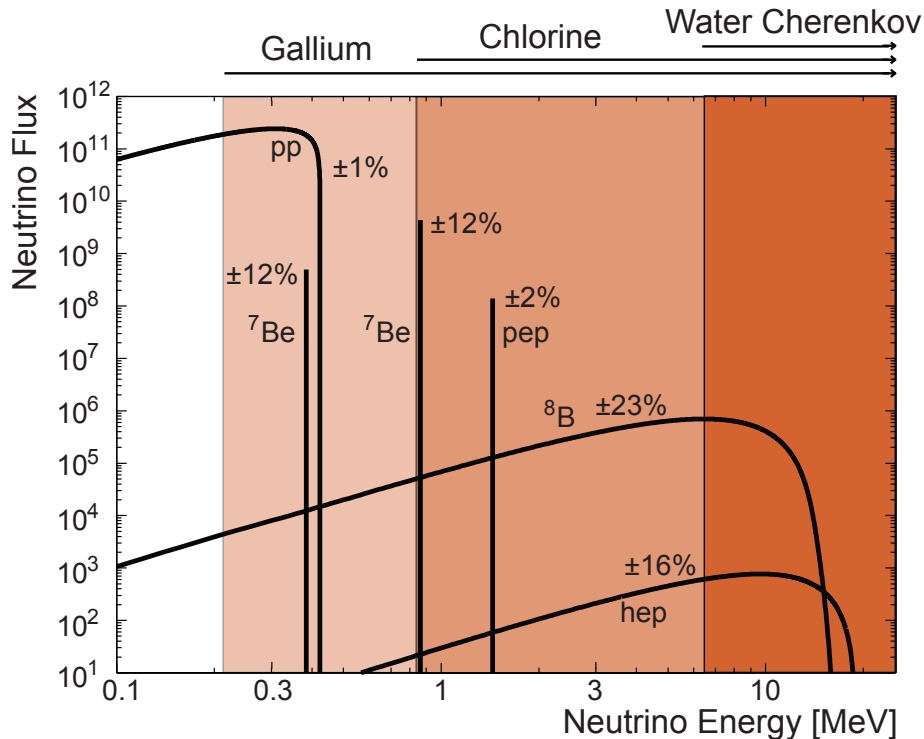


Figure 2.1: **Flux of solar neutrinos generated in the different fusion processes in the sun.** The numbers give the theoretical uncertainties on the fluxes of the process. The coloured areas represent the energy ranges, the respective experiments are sensitive to. Adapted from [18].

with  $x = e, \mu, \tau$ . The reactions respectively represent the charged current and neutral current reactions, as well as the elastic scattering of neutrinos with electrons. The respectively emitted Cherenkov light was detected by about 9500 photomultipliers, in order to identify the reactions. In contrast to previous experiments, the SNO experiment was not only sensitive to electron neutrinos, but to neutrinos of all generations, due to the detection of neutral current reactions and the elastic scattering. The results of the experiment showed an amount of  $\nu_\mu$  in the collected data, which is surprising, as none of the processes of the SSM should create these. However, the total neutrino flux was conform with the theoretical predictions. One explanation for these results is the change of flavour of some of the electron neutrinos to muon or tau neutrinos on their way from the core of the sun to the earth. This phenomenon can be explained with the theory of neutrino flavor oscillation. In the following years further experiments, like BOREXINO and Super-Kamiokande, observing all flavors of the neutrinos, with lower energy thresholds could show similar results for the other neutrino producing reactions in the sun [19].

### 2.3.2 The theory of neutrino oscillation

In order to find an explanation for the oscillation of neutrinos, it was compared to a similar phenomenon in particle physics, the mixing of quark flavors due to the non identical weak- and mass eigenstates [20]. For a non-vanishing neutrino mass and three flavor- and mass eigenstates, the same effect is possible for neutrinos, where their flavor eigenstates  $|\nu_\alpha\rangle$  ( $\alpha = e, \mu, \tau$ ) and the mass eigenstates  $|\nu_i\rangle$  ( $i = 1, 2, 3$ ) are not identical but connected via a  $3 \times 3$  mixing matrix  $U$  with

$$|\nu_\alpha\rangle = \sum_i U_{\alpha,i} |\nu_i\rangle. \quad (2.6)$$

Maki, Nakagawa and Sakata introduced the PMNS matrix using three mixing angles  $\Theta_{12}, \Theta_{23}, \Theta_{23}$  and one CP violating phase  $\delta$  for parametrization [21]

$$\begin{pmatrix} 1 & 0 & 0 \\ 0 & c_{23} & s_{23} \\ 0 & -s_{23} & c_{23} \end{pmatrix} \cdot \begin{pmatrix} c_{13} & 0 & s_{13}e^{-i\delta} \\ 0 & 1 & 0 \\ -s_{13}e^{-i\delta} & 0 & c_{13} \end{pmatrix} \cdot \begin{pmatrix} c_{12} & s_{12} & 0 \\ -s_{12} & c_{12} & 0 \\ 0 & 0 & 1 \end{pmatrix} \quad (2.7)$$

with  $s_{ij} = \sin \Theta_{ij}$  and  $c_{ij} = \cos \Theta_{ij}$  (The "P" in PMNS stands for Pontecorvo). The matrix is split into separate parts, according to the respective mixing angles. The additional CP-violating Majorana phase is neglected, as neutrino oscillation experiments are not sensitive to it. According to equation 2.6 the mass states can be seen as stationary eigenstates of the Hamiltonian  $H$  with eigenvalue  $E$ . When the neutrino is produced at time  $t = 0$ , it is in a pure flavor eigenstate, whereas the dependence on the mass eigenstates along a one-dimensional coordinate can be described by a plane wave:

$$|\nu_i(t)\rangle = e^{-iE_it} |\nu_i\rangle \quad (2.8)$$

Hence follows

$$|\nu_\alpha(t)\rangle = \sum_i U_{\alpha i} e^{-iE_it} |\nu_i\rangle = \sum_{i,\beta} U_{\alpha i} U_{\beta i}^* e^{-iE_it} |\nu_\beta\rangle \quad (2.9)$$

by replacing the mass eigenstates with a superposition of flavor eigenstates. Using equation 2.9, the probability for a neutrino oscillating from flavor  $\nu_\alpha$  to flavor  $\nu_\beta$  over time is calculated via:

$$P_{\nu_\alpha \rightarrow \nu_\beta}(t) = |\langle \nu_\beta(t) | \nu_\alpha(t) \rangle|^2 = \sum_{i,j} U_{\alpha i}^* U_{\beta i} U_{\alpha j} U_{\beta j}^* e^{-i(E_i - E_j)t} \quad (2.10)$$

In the ultra-relativistic case with ( $p_i \gg m_i$  and  $E \approx p_i$ ) it follows:

$$P_{\nu_\alpha \rightarrow \nu_\beta}(L/E) = \sum_{i,j} U_{\alpha i}^* U_{\beta i} U_{\alpha j} U_{\beta j}^* e^{-i \frac{\Delta m_{i,j}^2 L}{2E}}. \quad (2.11)$$

Here,  $L$  represents the distance between the source of the neutrino and the detector,  $E$  is the energy of the neutrino and  $\Delta m_{i,j}^2 \equiv m_i^2 - m_j^2$  represents the difference of the squared masses of the neutrino mass eigenstates. In order to measure the appearance and disappearance of the different neutrino flavors, the distance of the detector compared to the source has to be adapted with respect to the energy of the emitted neutrino and the mass difference and mixing angle of the respective neutrino flavors.

### 2.3.3 Neutrino oscillation experiments

In subsection 2.3.1, two of the numerous experiments to observe the oscillation of solar electron neutrinos to muon and tau neutrinos are presented. In general all of these experiments can be separated in two detection techniques. The radiochemical technique, used by Davis in the Homestake experiment observes the transformation of an atom due to the inverse  $\beta$ -decay. For this purpose, a large amount of the liquid detector material (615 t of tetrachloroethylene) is exposed to the solar neutrino flux for several weeks. In the case of the Homestake experiment, the detector material was liquid  $C_2Cl_4$ , which led to free argon atoms after the reaction with an electron neutrino. After the exposition,

the argon atoms were extracted from the detector material and subsequently counted, in order to determine the flux of solar electron neutrinos through the detector. Because of the lower energy threshold of the reaction, for later experiments like GALLEX, and GNO the transformation from gallium to germanium was observed. The other technique to measure the solar neutrino flux is represented by SNO, which measures the reaction of neutrinos with the detector material in real-time by observing the emitted Cherenkov light. Observing the solar neutrinos led to a further insight on the oscillation effects of neutrinos with energies larger than 1.9 MeV. Due to the coherent forward scattering with the large number of electrons in the sun, electron neutrinos experience a different effective mass than in vacuum, resulting in an increased oscillation probability. This effect is called MSW effect and must be considered in the determination of the mixing angle  $\Theta_{12}$  and the squared mass difference  $\Delta m_{12}^2$  for solar neutrinos [22].

Atmospheric neutrinos are the main final products in cosmic showers, initiated by the interaction of cosmic rays, composed of protons and  $\alpha$ -particles in the GeV-scale, with molecules in the upper atmosphere of the earth. Hereby, the number of produced muon neutrinos is about twice as high as the number of electron neutrinos for energies in the GeV-range, for which the earth remains transparent. This transparency was used for the Super-Kamiokande detector to investigate the up-down symmetry of neutrinos, i.e. the flavor probability of the detected neutrinos in relation to their flight distance through the earth [23]. Therefor a 50 kt water Cherenkov detector with about 11000 photomultipliers was built in Japan in the Kamioka mine. The most important feature is the real-time distinguishability of muon neutrinos and electron neutrinos. In 1998, the oscillation probability dependent on the zenith angle of the detected neutrinos between  $\nu_\mu$  and  $\nu_\tau$  could be proven. It could be shown that the electron neutrino flux is independent from its zenith angle in the detector, whereas the muon neutrino flux is clearly reduced, compared to the theoretical value, for negative zenith angles, corresponding to trajectories of the observed muon neutrino through the earth. From this deviation the mixing angle  $\Theta_{23}$  and the squared mass difference  $\Delta m_{23}^2$  for atmospheric neutrinos can be determined.

A further possibility to measure the respective parameters for the oscillation between muon and tau neutrinos are accelerator experiments, in which a high rate beam of muon neutrinos can be generated. Due to the distinct transparency of the earth, the neutrinos can be detected hundreds of kilometers in distance, where the disappearance of the muon neutrinos can be determined. One example for such long base line accelerator experiments is the CNGS experiment, detecting muon neutrinos, which are created at LHC, at the Gran Sasso Laboratory in Italy [24].

The third possible oscillation is regarding to the electron and tau neutrinos. In order to determine the respective parameters  $\Theta_{13}$  and  $\Delta m_{13}^2$  the electron neutrinos emitted in nuclear power plants are detected by short baseline experiments. The actual neutrino flux, emitted from the reactor, is detected very closely to the power plant. The second detector, located further away (in the range of about 1 km), then determines the disappearance of the electron neutrinos. Due to the relatively short oscillation length of this process, the transformation into a muon neutrino can be neglected. The biggest, and most sensitive, experiment is Daya Bay in China with four close and four far detectors [25].

The recent results of these experiments show non-vanishing results for for all three mixing angles and the mass differences of the neutrino mass eigenstates, however the sign of  $\Delta m_{13}$  was not yet determined. The gathered information allow three scenarios for the total neutrino mass eigenstates: the quasi-degenerated case with  $m_1 \approx m_2 \approx m_3 \gg 10^{-3}$  eV, the normal mass hierarchy with  $m_1 < m_2 \ll m_3$  and the inverted mass hierarchy with  $m_3 \ll m_1 < m_2$ . The latter two cases are illustrated in Fig. 2.2. The flavor composition for each mass eigenstate is indicated by the coloured bars. In order to make

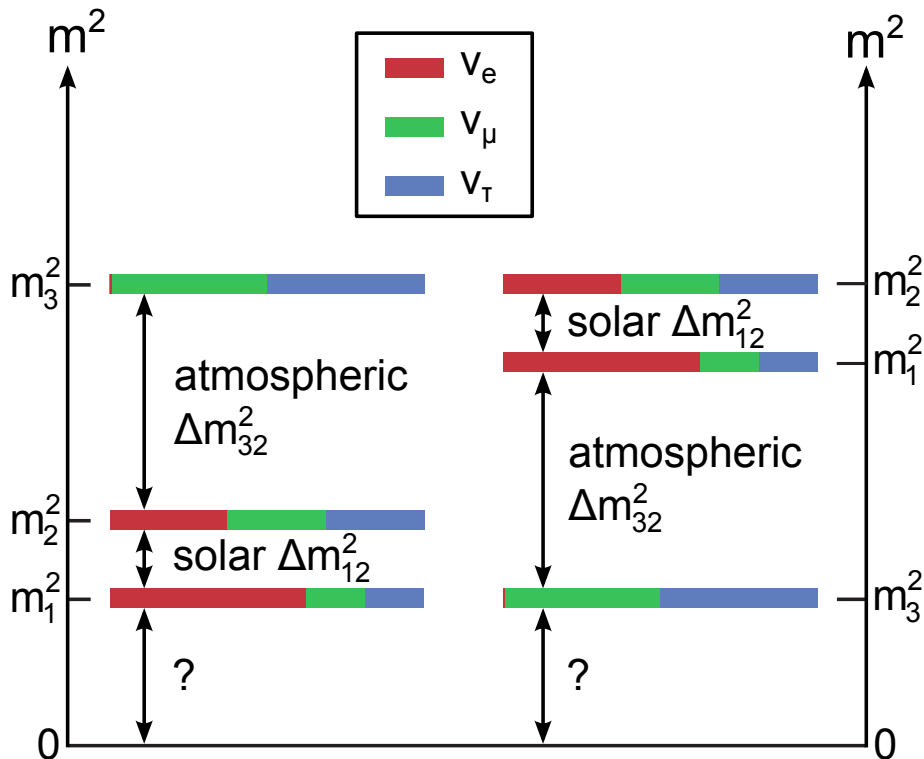


Figure 2.2: **Normal and inverted neutrino mass hierarchy.** The respective contributions of the flavor eigenstates are represented by the colored bars. The total offset of the mass eigenstates cannot be derived from oscillation experiments and has to be determined by direct mass measurements. Taken from [26].

a distinct statement on the absolute mass scale, direct measurements of the neutrino mass are indispensable.

## 2.4 Experimental approaches to measure the neutrino rest mass

The discovery of neutrino flavor oscillation is the irrevocable evidence for neutrinos to be massive. However the oscillation experiments only are sensitive to the mass differences of the neutrino mass eigenstates. In order to determine the total masses of the neutrinos many different approaches are possible. In general they can be separated in model-dependent and model-independent experiments and in the following the most prominent of them are shortly discussed.

### Cosmological investigations

In 2009, the Planck satellite experiment was launched to measure the anisotropies in the temperature of the cosmic microwave background radiation (CMB) with very high precision. The CMB originates from the decoupling of photons from matter about 380 000 years after the Big Bang. According to that, also a cosmic neutrino background exists from the decoupling of neutrinos from matter. Due to their very low energies and small interaction cross-sections, these so-called relic neutrinos have not yet been detected. However, from the cosmological model, based on the insights of the CMB measurements, the density of relic neutrinos  $\Omega_\nu$  can be estimated to  $336 \text{ cm}^{-3}$  and by comparing it to the total energy density of the universe  $\Omega_{\text{tot}}$  the total mass for all three neutrino eigenstates sums to

$$\sum_k m_k = 93\Omega_\nu h^2 \text{ eV} \quad (2.12)$$

with  $h$  as the dimensionless Hubble parameter. With the latest results on the large scale structures in the universe and the power spectrum of the CMB temperature anisotropy the number density of relic neutrinos was determined very precisely, so that the model-dependent upper limit for all neutrino mass eigenstates is [27]

$$\sum_k m_k \leq 0.23 \text{ eV}. \quad (2.13)$$

### Time-of-flight studies of supernova neutrinos

At the end of their stellar evolution, heavy stars with  $m > 40m_\odot$  collapse under their own gravitational force. Almost the entire gravitational energy of the former star is carried away by neutrinos in the MeV-range within a very short time-window. The processes generating the neutrinos are:

$$e^- + p \rightarrow n + \nu_e \quad (2.14)$$

$$e^- + e^+ \rightarrow \nu_i + \bar{\nu}_i. \quad (2.15)$$

From the duration of the detected neutrino signal, the distance of the former star to the detector and the energies of the detected neutrinos and their mass can be calculated. However, this method is strongly model-dependent, as the respective position and time of the generation of the neutrino and the mechanism model of the stellar collapse are assumptions. In 1987, 25 neutrino events from a supernova were detected and measured by underground water Cherenkov detectors like Kamiokande II [28]. Using this data, a detailed analysis set the upper limit of the mass of the electron antineutrino to [29]

$$m_{\bar{\nu}_e} \leq 5.7 \text{ eV}. \quad (2.16)$$

### Investigations of the neutrinoless double $\beta$ -decay

For some isotopes in nuclear physics the single- $\beta$ -decay can be forbidden, due to energetically higher final states in the nucleus. In this case, the very rare double- $\beta$ -decay is observable, in which simultaneously two electrons or positrons and two electron neutrinos or antineutrinos are emitted:

$$2p \rightarrow 2n + 2e^+ + 2\nu_e \quad (2.17)$$

$$2n \rightarrow 2p + 2e^- + 2\bar{\nu}_e \quad (2.18)$$

This decay is observable for several isotopes and the schematic nucleus reaction and the corresponding continuous energy distribution can be seen in Fig. 2.3. In 1937, E. Majorana published his theory, in which neutrinos might be their own antiparticle, theoretically allowed, as they do not carry charge [30]. One consequence of the theory is the potential neutrinoless double  $\beta$ -decay, in which the Majorana neutrino is emitted and absorbed within the nucleus, i.e. being virtual. This process is illustrated on the left side of Fig. 2.3. In this case, the two observable charged leptons share the total energy released in the double- $\beta$ -decay, resulting as a small peak at the endpoint of the energy spectrum, as shown in Fig. 2.3. Although several experiments like GERDA [31] or MAJORANA [32] look for this decay, it has not been detected so far. The measurement parameter of these experiments is the half life  $T_{1/2}^{0\nu\beta\beta}$  given by

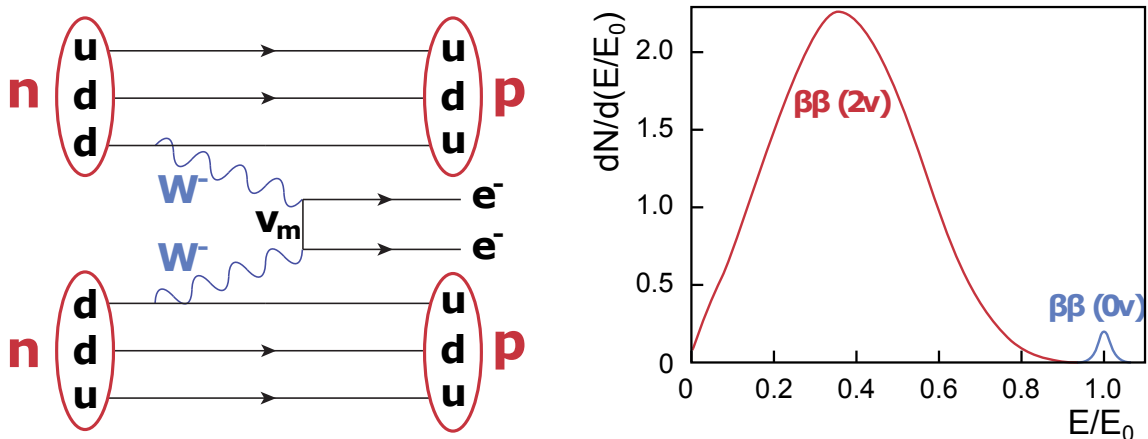


Figure 2.3: **Schematic double  $\beta$ -decay.** **Left:** The Feynman diagram of the neutrinoless double  $\beta$ -decay shows the exchange of a virtual neutrino. In this case only two electrons are emitted from the nucleus. **Right:** The two electrons share the total energy of the decay, resulting in a sharp peak at the endpoint of the spectrum. For overview reasons the peak for the neutrinoless double- $\beta$ -decay was magnified. Adapted from [26].

$$\left(T_{1/2}^{0\nu\beta\beta}\right)^{-1} = G^{0\nu\beta\beta}(Q_{\beta\beta}, Z) \cdot |M_{GT}^{0\nu\beta\beta} - \left(\frac{g_V}{g_A}\right)^2 M_F^{0\nu\beta\beta}|^2 \cdot \langle m_{\beta\beta} \rangle^2, \quad (2.19)$$

which is valid for the simple case of purely left-handed V-A weak currents and light massive Majorana neutrinos. Here,  $G^{0\nu\beta\beta}$  is the phase space factor,  $Q_{\beta\beta}$  is the endpoint energy,  $Z$  is the atomic number of the decaying isotope,  $M_{GT}^{0\nu\beta\beta}$  and  $M_F^{0\nu\beta\beta}$  are the respective Gamov-Teller and Fermi matrix elements and  $g_V$  and  $g_A$  are the axial and vector coupling constants. The factor  $m_{\beta\beta}$  is the coherent sum of the effective Majorana neutrino mass eigenstates with  $m_{\beta\beta} = |\sum_{i=1}^3 U_{ei}^2 \cdot m_i|$ . Hence, the discovery of a neutrinoless double- $\beta$ -decay would not only reveal the characteristics of the neutrino, being a Majorana or a Dirac particle, but also give a strongly model-dependent value for the neutrino mass. As until today, only the lower boarder of the half life with  $T_{1/2}^{0\nu\beta\beta} \geq 2.1 \cdot 10^{25}$  a is given, for the Majorana neutrino mass follows  $m_{\beta\beta} < (0.2 - 0.4)$  eV.

### Investigations on the kinematics of the single- $\beta$ -decay

The model-independent way to determine the mass of the electron antineutrino is the investigation of the single  $\beta^-$ -decay by kinematic means. As this process is a three-body-decay reaction, according to

$$n \rightarrow p + e^- + \bar{\nu}_e \quad (2.20)$$

the energy spectrum of the emitted electron shown in Fig. 2.4 carries information on the mass of the electron antineutrino due to the laws of energy and momentum conservation. By determination of the kinetic energy distribution of electrons at the endpoint of the spectrum, where relativistic effects on the neutrino are negligible, the effective mass of the electron antineutrino can be measured.

The energy spectrum of the  $\beta$ -electron can be derived from Fermi's Golden Rule [33]

$$\frac{d^2 N}{dE dt} = \frac{G_F^2 \cos^2 \Theta_C}{2\pi^3 c^5 \hbar^7} \cdot |M|^2 \cdot F(E, Z+1) \cdot p_e \cdot (m_e c^2 + E) \cdot (E_0 - E) \cdot \sqrt{(E_0 - E)^2 - m_{\bar{\nu}_e}^2 c^4} \quad (2.21)$$

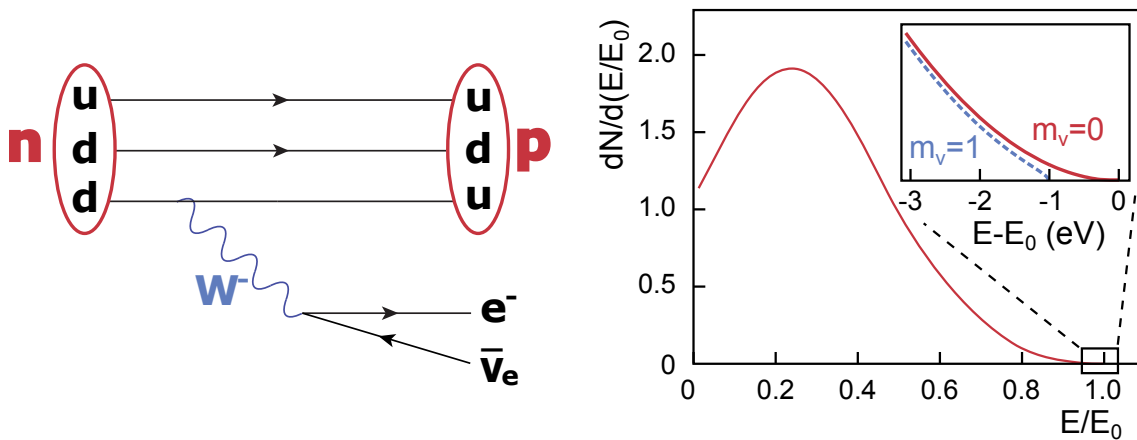


Figure 2.4: **Schematic single  $\beta$ -decay.** **Left:** The Feynman diagram of the single  $\beta$ -decay shows the transformation of a neutron to a proton by emitting a  $W^-$ -boson, which subsequently decays to an electron and an antineutrino. **Right:** The characteristic shape of the electron energy spectrum is illustrated. The zoom into the endpoint of the spectrum shows the spectrum for a vanishing neutrino mass (solid red line) and a non-zero neutrino mass of exemplary  $m_{\nu_e} = 1$  eV (dashed blue line). Adapted from [26]

Here,  $G_F$  is the Fermi coupling constant,  $\Theta_C$  is the Cabibbo angle,  $M$  is the hadronic matrix element,  $F$  is the Fermi function,  $p_e$ ,  $m_e$  and  $E$  are the momentum, mass and energy of the emitted electron and  $E_0$  represents the theoretical endpoint of the electron energy spectrum for a massless neutrino and a negligible recoil on the daughter nucleus.

From this equation  $m_{\nu_e}$  follows as experimental observable in single- $\beta$ -decay experiments. It represents the mass of the flavor eigenstates of an electron antineutrino, given by the averaged and weighted masses of the neutrino mass eigenstates. A non-zero neutrino mass leads to the deformation of the electron energy spectrum and a lower endpoint energy, indicated in the endpoint region in Fig. 2.4.

The best model-independent limits on the electron anti-neutrino mass are set by experiments in Mainz [34] and Troitsk [35]. They observed the  $\beta$ -decay of tritium and used a MAC-E filter to determine the energy spectrum of the emitted electron. A combined analysis for both experiments yields [36]

$$m_{\nu_e} < 2.0 \text{ eV (95\% C.L.)}. \quad (2.22)$$

The limits of the experiments were caused by systematic uncertainties and restricted source statistics. In order to observe the mass of the electron antineutrino in the sub-eV scale the KATRIN experiment is constructed in Karlsruhe at the Campus North site of the KIT. By using a windowless gaseous tritium source and a large-scale MAC-E filter spectrometer it has the aim to surpass the sensitivity of the previous experiments by a factor of 10 [37].

## 3. The KATRIN Experiment

In 2001, the KATRIN collaboration was founded. It consists of several institutes and universities from all over the world with a significant participation from Germany and the USA. The goal of KATRIN is to determine the mass of the electron antineutrino model-independently with a sensitivity of  $m_{\bar{\nu}_e} \leq 200 \text{ meV}/c^2$  (90 % C.L.) by analyzing the  $\beta$ -decay of tritium. The experiment is located on Campus North of the Karlsruhe Institute of Technology (KIT), where the Tritium Laboratory Karlsruhe (TLK) has the knowledge and the license to handle the required amount of tritium.

In this chapter the general measurement principle based on a MAC-E filter will be given (section 3.1), followed by a short overview of the entire experiment and its principal components (section 3.2). Finally, the dependence of the sensitivity of the KATRIN experiment on the systematic and statistical uncertainties is discussed (section 3.3).

### 3.1 The measurement principle

The rate of electrons with kinetic energies near the endpoint of the  $\beta$ -decay energy spectrum, which is observed by the KATRIN experiment, is very low. In order to combine very high statistical and systematic precision, required for the goals of the experiment, the MAC-E filter (Magnetic Adiabatic Collimation combined with an Electrostatic Filter) principle [38] is used for the determination of the electron energies. The operating principle of such a spectrometer is based on the combination of magnetic and electric fields, as illustrated in Fig. 3.1. Superconducting solenoids at each end of the spectrometer provide the magnetic field necessary to adiabatically transport the decay electrons through the MAC-E filter. The electric field, parallel to the magnetic field lines, is generated by elevating the spectrometer vessel to a negative potential  $U_0$  and acts as a barrier for the incoming electrons. To pass this barrier and subsequently being detected at the detector, electrons need a longitudinal kinetic energy of  $E_{\parallel} \geq eU_0$ . By varying the potential of the spectrometer, the energy spectrum of the observed  $\beta$ -decay can be scanned in an integral way.

Since the kinetic energy of the decay-electrons is not exclusively aligned in longitudinal direction, the transverse kinetic energy  $E_{\perp}$  must be transformed into longitudinal energy in order to analyze their full energy. This is realized via varying magnetic field strengths  $B$  along their path through the spectrometer. If the field strength varies slowly enough (adiabatic), the magnetic moment  $\mu$  of the electrons follows the relation:

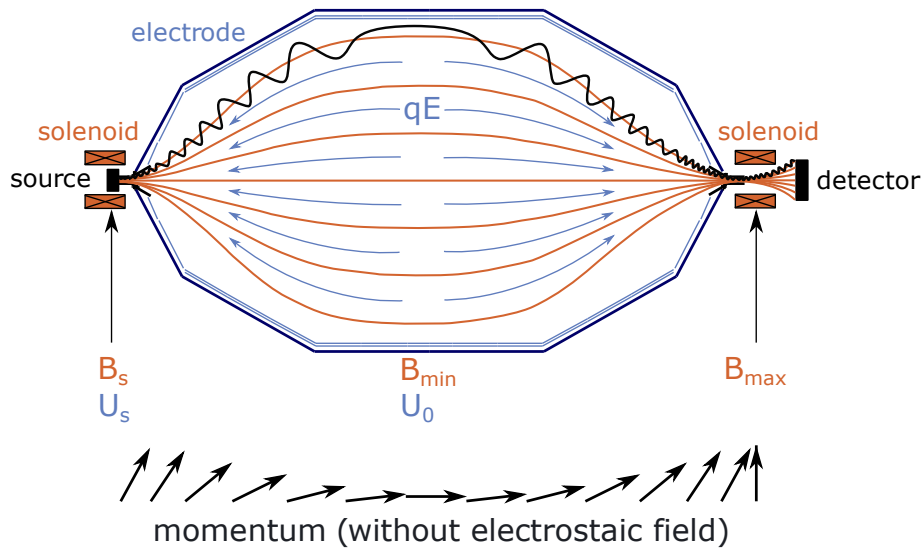


Figure 3.1: **Illustration of the MAC-E filter principle.** The electrons reach the filter on cyclotron trajectories (black), and the transverse component of their momentum gets transformed into a longitudinal component by the decreasing magnetic flux density (red). The electric field (blue), induced by electrodes on the walls, retards the incoming electrons. The black arrows beneath illustrate the direction of the electron's momentum, in dependence of the magnetic flux density. Adapted from [39].

$$\mu = \frac{E_{\perp}}{B} = \text{const.} \quad (3.1)$$

The magnetic field inside the spectrometer decreases until the magnetic flux density reaches a minimum at the analyzing plane, so the transverse kinetic energy must reach its minimum there, too. Without this transformation of energy, only electrons with maximum energy in longitudinal direction could be analyzed and the required luminosity could not be reached. The opposite effect of this so-called magnetic adiabatic collimation is the magnetic mirror effect, describing the reflection of electrons moving from a weak into a strong magnetic field. As the maximum magnetic field strength in the KATRIN experiment is provided by the pinch magnet (6 T), which is located between the spectrometer and the detector, a fraction of the electrons will be reflected. Within this thesis, electrons created in the spectrometer volume or on its surface play a major role. As inside the spectrometer and on its inner surface the magnetic field is very small the magnetic mirror has a big effect on their arrival probability on the detector. For electrons, emitted in the source the requirement, not to be reflected is given by [26]

$$\Theta_{\max} = \arcsin \sqrt{\frac{B_{\text{S}}}{B_{\max}}} \quad (3.2)$$

where  $\Theta_{\max}$  is the maximum polar angle for the emission of electrons in the source,  $B_{\text{S}}$  is the magnetic field strength in the source and  $B_{\max}$  is the maximum magnetic field, the electron experiences. In the case of electrons starting at the spectrometer surface, the arrival probability is no longer given in an analytical way, but has to be derived from simulations, as shown in section 6.2. It will be shown, that the arrival probability not only depends on the emission angle, but also on the initial kinetic energy and the location of the electron.

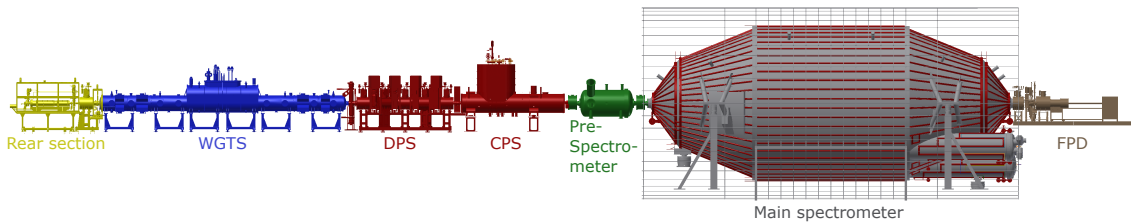


Figure 3.2: **Illustration of the KATRIN experiment** with its different subsystems. It has a total length of about 70 m and the maximum diameter measures 10 m at the main spectrometer. The electrons are emitted in the WGTS, are guided magnetic adiabatically through the transport section, are energetically filtered in the two spectrometers and detected by the Focal-Plane Detector. The rear section monitors the source parameters. Adapted from [40]

In the center plane of the spectrometer the magnetic field reaches its minimum strength  $B_{\min} \neq 0$  T. Consequently the transversal component of the kinetic electron energy is not fully transformed to longitudinal kinetic energy, and thus, is analyzed incorrectly by the MAC-E filter. This limitation determines the energy resolution of the KATRIN spectrometer to:

$$\Delta E = \frac{B_{\min}}{B_{\max}} \cdot E_{\perp, \max} \quad (3.3)$$

with  $E_{\perp, \max}$  as the maximum kinetic energy in transversal direction.

## 3.2 The experimental setup

The KATRIN setup is about 70 m long and consists of several components (see Fig. 3.2). The electrons are emitted in the Windowless Gaseous Tritium Source (WGTS) (see section 3.2.1) and guided adiabatically through a Transport Section (see section 3.2.2) to two electrostatic retarding spectrometers. The pre-spectrometer and the main spectrometer (see section 3.2.3) maintain the function of a highpass filter for the  $\beta$ -decay electrons. The transmitted electrons are counted in the Focal-Plane Detector System (FPD) (see section 3.2.4) with high detection efficiency and nearly background free.

### 3.2.1 Tritium source

As in the Troitsk neutrino experiment, the KATRIN experiment utilizes a Windowless Gaseous Tritium Source (WGTS) [41], limiting the energy loss of the emitted  $\beta$ -electrons to scattering effects with tritium only. It consists of a pipe with a length of 10 m and a diameter of 9 cm. The source is cooled to a temperature of about 30 K by liquid neon. The gaseous tritium molecules are injected through cones in the middle of the pipe at a rate of  $q = 1.853 \text{ mbar} \cdot \text{l/s}$ . The temperature and the injection rate have a very high influence on the systematic uncertainty of KATRIN. Therefore, a high temperature stability ( $\pm 3$  mK), to minimize Doppler-broadening from thermal fluctuations, and a high stability of the injection rate (0.1%) to reduce turbulences of the gas, are necessary. At both ends of the pipe there are differential pumping systems, reducing the tritium flow by a factor of 100 and transporting the molecules out of the pipe and back into a tritium refurbishing loop. Within the tritium loop system, a Laser Raman-spectroscope [42] is located to monitor the isotopic purity of the tritium gas, before it is reinjected into the WGTS.

The  $\beta$ -decay electrons are guided adiabatically out of the source by a magnetic field of  $B_{\text{WGTS}} = 3.6$  T, provided by 7 superconducting solenoids. As KATRIN observes the end point of the  $\beta$ -decay energy spectrum, only a small part of the emitted electrons

is important and therefore, a high luminosity electron source is required. This is why KATRIN uses a windowless tritium source. Here, more electrons leave the source and there is no loss of energy by passing a window or a membrane, reducing systematic effects. The WGTS emits about  $10^{11}$   $\beta$ -electrons per second [37].

The rear section system is located at the upstream end of the WGTS and is used to control and monitor the process parameters in the source, such as the source activity, the electric potential of the tritium plasma and the column density of the tritium gas.

### 3.2.2 Transport section

The transport section, that connects the WGTS to the spectrometers, consists of the Differential Pumping Section (DPS2-F) [43] and the Cryogenic Pumping Section (CPS) [44]. Their main goal is to return the tritium gas to the source while adiabatically guiding the  $\beta$ -decay electrons towards the two retarding spectrometers. The tritium flow has to be reduced by 14 orders of magnitude to avoid tritium molecules reaching the spectrometers as they would add an immense background contribution if decaying inside the spectrometers.

The DPS2-F consists of four turbomolecular pumps, which reduce the tritium flow by a factor of  $10^5$ . In order to increase the pumping efficiency, the beam tube of the DPS is arranged with two  $20^\circ$ -chicanes, inducing a reduction of the tritium flux. The tritium, pumped out by the DPS2-F behind the WGTS, is fed back to the tritium laboratory via the so called "outer loop" [45]. The signal electrons are guided adiabatically through the chicanes by five superconducting solenoids, each generating a magnetic field of  $B = 5.6$  T.

The following CPS is designed to reduce the flow by another factor of  $10^7$ . Its functionality is based on the adsorption of the tritium gas on argon frost which covers its inside walls. Therefore the tube is cooled to 4.5 K via liquid helium. For regeneration of the CPS, the systems is warmed up to 100 K, flushed with helium and the argon frost gets renewed. This procedure happens every 60 days, between two measurement phases. To increase the trapping efficiency, the beam tube of the CPS is tilted by  $20^\circ$  in two chicanes, so there is no direct line of sight for the tritium molecules to the spectrometers [44]. The magnetic adiabatical electron transport is realized via 22 superconducting solenoids.

### 3.2.3 Spectrometers

The transport section is followed by the pre-spectrometer [46] and the main spectrometer [37], building a tandem setup of two electrostatic retardation spectrometers, based on the MAC-E filter principle. In order to minimize the background from decaying tritium molecules in the spectrometer and to minimize the scattering of electrons from the observed  $\beta$ -decay with residual gas molecules the pressure in the spectrometer system is in the UHV regime with about  $10^{-11}$  mbar.

The pre-spectrometer connects the transport section to the main spectrometer. It has a length of 3.4 m and a diameter of 1.7 m, with two superconducting magnets PS1 and PS2 at each end to provide the magnetic field, required for the MAC-E filter. Both magnets will be operated at fields of 4.5 T resulting in an energy resolution of  $\Delta E \approx 70$  eV for electrons with the maximum kinetic energy from the decay. In the tritium scanning mode the pre-spectrometer will act as a filter for decay-electrons with relatively low energies. Therefore, its retarding potential will be set to  $-18.3$  keV, resulting in a reduction of the electron flux from the source by 7 orders of magnitude. This reduction of electrons is important to lower the background generated by low energetic  $\beta$ -electrons scattering with rest gas molecules inside the main spectrometer. Furthermore, the electron rate would also overwhelm the detector, which cannot handle rates larger than  $10^6$   $e^-/s$ .

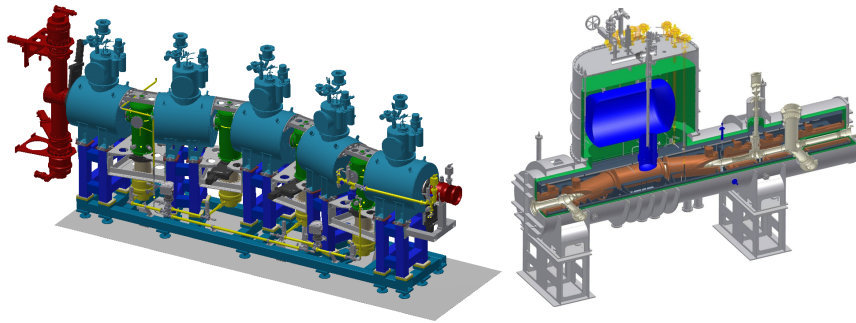


Figure 3.3: **The KATRIN transport section components.** **Left: Differential pumping section (DPS)** The differential pumping section follows the WGTS and reduces the tritium gas flux by five orders of magnitude with four turbomolecular pumps (yellow). The five superconducting magnets (blue) guide the electrons adiabatically through the beam tube (red), which is arranged in two chicanes. Figure from [26]. **Right: Cryogenic pumping section (CPS)** The cryogenic pumping section follows the DPS and reduces the tritium gas flow by another seven orders of magnitude, by adsorbing them to the inner surface of the beam tube, which is covered by argon frost. To ensure the collision of the tritium molecules with the surface again two chicanes are integrated into the beam tube. The electrons are guided adiabatically through the CPS via seven superconducting magnets. The CPS is followed by the pre-spectrometer in the experimental setup. Adapted from [39]

The main spectrometer is 23.3 m long and has a maximal diameter of 10 m. The magnetic field inside the vessel is provided by the PS2 magnet on the upstream side and the Pinch magnet on the downstream side with 6.0 T. The magnetic flux density in the analyzing plane reaches  $B_{min} = 0.3$  mT, resulting in an energy resolution of  $\Delta E = 0.93$  eV for electrons with a kinetic energy of  $E_0 = 18.6$  keV. To compensate the earth's magnetic field and to further fine shape the field inside the vessel a system of air coils surrounds the main spectrometer. On the inner surface of the vessel a two-layer wire system is installed to adjust the electrostatic behavior of the spectrometer on a very detailed level. An additional requirement of this system is to prevent low-energy electrons, emitted on the surface, from entering the volume of the spectrometer. In the tritium scanning mode the retarding potential of the main spectrometer will be varied in the range from  $E_0 - 30$  eV to  $E_0 + 5$  eV in order to observe the endpoint of the tritium decay spectrum.

### 3.2.4 Focal-Plane detector system

The main spectrometer is followed by the Focal-Plane Detector (FPD) system [26] [47]. Its major task is to count the electrons, which passed the MAC-E filter with high detection efficiency and nearly background free. During neutrino mass measurements only a few signal electrons per second will pass the analyzing plane of the main spectrometer. Nevertheless, the detector has to be able to handle rates of several kHz during calibration measurements.

Figure 3.4 shows the main components of the FPD system. Most conspicuous are the two superconducting magnets which guide the electrons through the FPD system. The detector wafer is located inside the warm bore of the Detector magnet. It consists of a monolithic segmented 148-Pixel PIN diode array, fabricated onto a single silicon wafer of 90 mm in diameter and 500  $\mu\text{m}$  thick. A post-acceleration electrode, located in front of the wafer, can be used to accelerate the signal electrons coming from the main spectrometer by theoretically up to 30 keV. This allows for a shift of the electron energy spectrum to

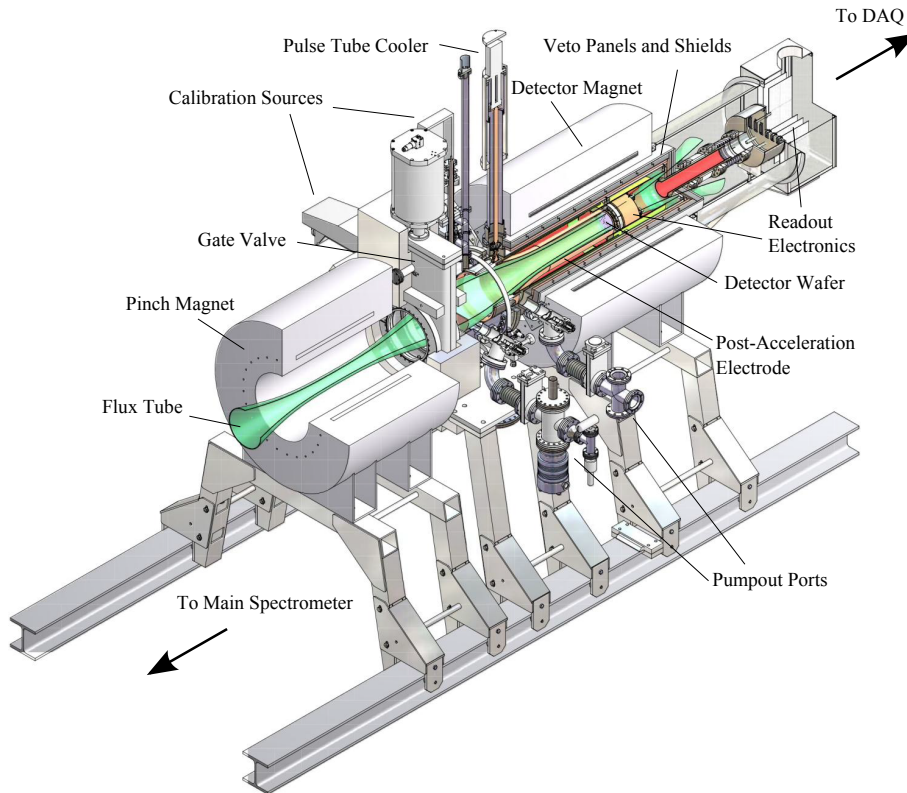


Figure 3.4: **Illustration of the Focal-Plane Detector system.** Adapted from [47].

higher energies where less background is expected. To calibrate and test the FPD system independently, it possesses two calibration sources, a  $^{241}\text{Am}$ -Source and a titanium disc. Both can be moved in and out of the flux tube without breaking the UHV. By using the  $^{241}\text{Am}$ -Source, the characteristics and signals of the detector with respect to monoenergetic  $\gamma$ -photons can be observed. The titanium disc can be set on high voltage of up to 25 kV and illuminated with a UV-photodiode. The resulting electrons, emitted by the photoeffect principle, are monoenergetic and can also be used for the characterization of the detector response. The detector signals are processed by readout electronics. Since the readout electronics floats at the PAE voltage, the readout electronics are connected to the Data Acquisition System (DAQ) via fiber optics. The signals are then digitized and processed under the control of the KATRIN DAQ software ORCA [48].

In addition to passive copper and lead shields, an active muon veto system surrounds the detector beamline to further detect and reduce background, induced by cosmic muons. All materials used in the detector system have been selected to be of low intrinsic radioactivity.

### 3.3 The sensitivity of KATRIN

The sensitivity of the KATRIN experiment to the mass of the electron antineutrino depends on several parameters that have to be set and observed carefully. It consists of the systematic and statistical uncertainties on the measurement and must not exceed

$$\sigma = \sqrt{\sigma_{sys.}^2 + \sigma_{stat.}^2} = 0.025 \text{ eV}^2 \quad (3.4)$$

For a vanishing neutrino mass this total uncertainty results in a sensitivity of

$$m_{\nu_e} \leq 200 \text{ meV} \quad (3.5)$$

with a confidence level of 90 %.

The systematic uncertainty, limited to  $\sigma_{\text{sys.}} = 0.017 \text{ eV}^2$ , mainly depends on the accuracy, with which the physical parameters of the experiment can be set and the energy loss mechanisms due to transport properties of the electrons. In order to minimize the systematic uncertainties the generation and transport conditions must be as similar as possible for all signal electrons. For this reason, the pressure and temperature in the WGTS and the purity of the molecular tritium must be known with a precision of 0.1 %. The transport of the electrons is mainly dominated by scattering with tritium molecules in the source and residual gas molecules in the spectrometer and radiation induced energy losses of the electrons on their cyclotron trajectory.

The statistical uncertainty of the experiment obviously depends on the effective measurement time  $t_{\text{meas.}}$ . In order to achieve a value in the same range as the expected systematic uncertainty,  $t_{\text{meas.}} = 3$  years is chosen, resulting in  $\sigma_{\text{stat.}} = 0.018 \text{ eV}^2$ . Including maintenance and calibration recesses, the total run time of KATRIN is expected to be 5 years. The main parameters on the statistical uncertainty are a good energy resolution of the spectrometer and a large signal-to-background ratio. Therefore, on the one hand, a very high luminosity of the electron source is necessary. In order to achieve a optimized ratio of signal electrons from  $\beta$ -decay and a low scattering probability of these electrons with tritium molecules a tritium column density of  $5 \cdot 10^{17} \text{ molecules/cm}^2$  was chosen. Additionally, the source and spectrometer was designed to allow a polar emission angle of  $51^\circ$  for the electrons, to arrive at the detector. The other factor to increase the signal-to-background ratio, is a very low overall background signal of  $R_{\text{bg}} = 0.01 \text{ cps}$ , whereby the spectrometer is expected to be the major contributor, due to the large surfaces.



## 4. The spectrometer and detector section

From October 2014 to September 2015 the second commissioning phase of the spectrometer and detector section (SDS) was carried out. It was split into two phases, whereby the major difference was the vacuum bake-out of the main spectrometer before the second phase. All relevant measurements for this thesis were carried out during this second measurement phase SDS-IIb, which had the goal to gain a better understanding of the background processes in the main spectrometer.

Fig. 4.1 shows the total experimental setup of the SDS-IIb measurement phase which is presented more precisely in this chapter. In section 4.1 the vacuum system of the main spectrometer and of the FPD system are outlined, followed by the magnet system in section 4.2 and the high-voltage system of the SDS system in section 4.3. Finally, the data acquisition and processing of the FPD system is presented in section 4.4.

### 4.1 Vacuum

In order to reduce the scattering of signal electrons to a minimum, the vacuum system of the main spectrometer and the detector system is designed to achieve a pressure of about  $10^{-11}$  mbar. The major gas source, that disturbs the vacuum is the outgassing of hydrogen from the stainless steel surfaces inside the spectrometer, totaling of  $1240\text{ m}^2$ , consisting of the vessel wall with about  $690\text{ m}^2$  and the inner electrode system with its support structures. According to [49], the outgassing rate of the hydrogen is estimated to  $1.4 - 2.5\text{ mbar}\cdot\text{l/s}$  into the  $1240\text{ m}^3$  volume of the spectrometer.

The vacuum setup of the FPD system contains two separate chambers, the ultra high vacuum chamber (UHV) and the high vacuum chamber (HV). The UHV chamber is directly connected to the spectrometer and closed up by the detector wafer on the downstream side. The HV chamber of the detector system partially surrounds the UHV chamber and houses the cooled front-end electronics of the detector read out system. It is usually operated at a pressure of about  $10^{-6}$  mbar in order to provide thermal insulation for the cooled electronics.

For the initial pump-down of the spectrometer from ambient air pressure, for example after a maintenance phase, a temporary screw pump is used. To reach the vacuum quality required for the standard operation mode, three different types of vacuum pumps are used. The major contributor to the pump capacity is the non-evaporable getter (NEG) material, located in three pump ports on the downstream end of the spectrometer (see Fig. 4.1).

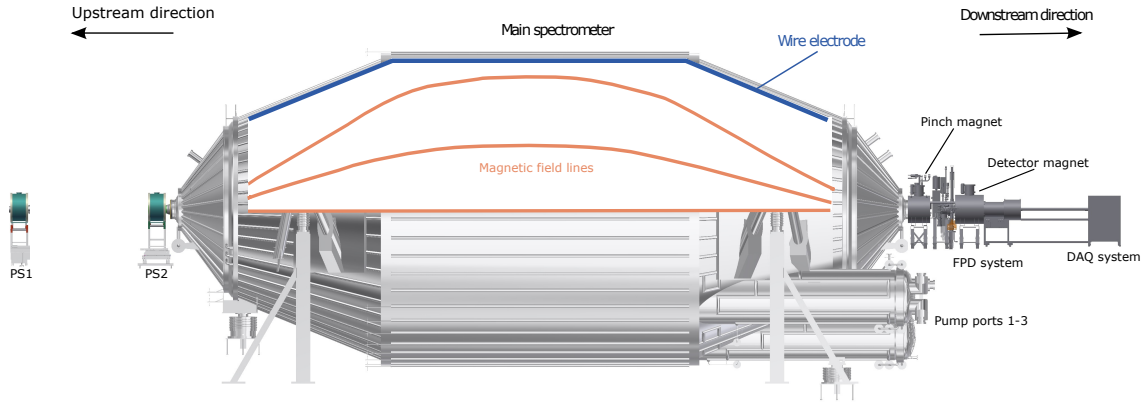


Figure 4.1: **Overview of the SDS-IIb experimental setup** including the main spectrometer, the FPD system and the two pre-spectrometer magnets. The air coil system, that surrounds the spectrometer is not shown here. Shown in blue is the inner electrode system that covers the entire inner surface of the spectrometer. Shown in red are the magnetic field lines inside the spectrometer induced by the PS2 and Pinch magnets. The shape of the field lines can be fine tuned by the air coil magnets.

The total effective getter surface adds up to  $167\text{ m}^2$ , providing a pumping speed of  $10^6\text{ l/s}$  for hydrogen. The activation of the getter material is achieved by increasing the material temperature to  $400\text{ }^\circ\text{C}$ , by a electrical heating of the getter strips. One disadvantage of the getter material is the emanation of radon. As radon is a major contributor to the KATRIN background (see section 5.1.3) a counter measure, in form of a liquid nitrogen cooled baffle system was installed in each NEG pump port, to trap the radon atoms before they can enter the sensitive spectrometer volume and decaying there.

The non-getterable gases, such as the noble gases and methane, are pumped out by six sets of cascaded pumping systems, consisting of two turbomolecular pumps (TMP) and one scroll pump. Each of these pump systems has a pumping speed of  $400\text{ l/s}$  for hydrogen and they are located on the NEG pump ports one and three.

In order to be in the position to run the FPD system separately from the spectrometer system, cryogenic pumps are used to achieve the vacuum in the two vacuum chambers, as TMPs can not be operated in the magnetic stray fields of the detector system. The initial pump-down of the detector vacuum chambers is performed with a pair of mobile TMPs, which are moved away before any magnet operation.

Prior to the SDS-IIb measurement phase a bake-out of the main spectrometer was performed by heating it to a temperature of  $200\text{ }^\circ\text{C}$  for eight consecutive days. This is achieved by pipes that surround the vessel and contain a heat-transfer fluid, which is heated and circulated by a heating device with a power of  $440\text{ kW}$ . Smaller parts of the spectrometer, are baked out with electrical heating tapes. Residual gas measurements made before and after the bake-out showed that the water layer, covering the inner surface of the spectrometer had been considerably reduced. As a consequence the pressure was improved from  $3 \cdot 10^{-10}\text{ mbar}$  to  $6 \cdot 10^{-11}\text{ mbar}$  and was stable for the entire measurement phase.

## 4.2 Magnets

At the upstream side of the SDS setup, the two superconducting magnets PS1 and PS2, as seen in Fig. 4.1 provide the magnetic field necessary for the MAC-E filter principle of

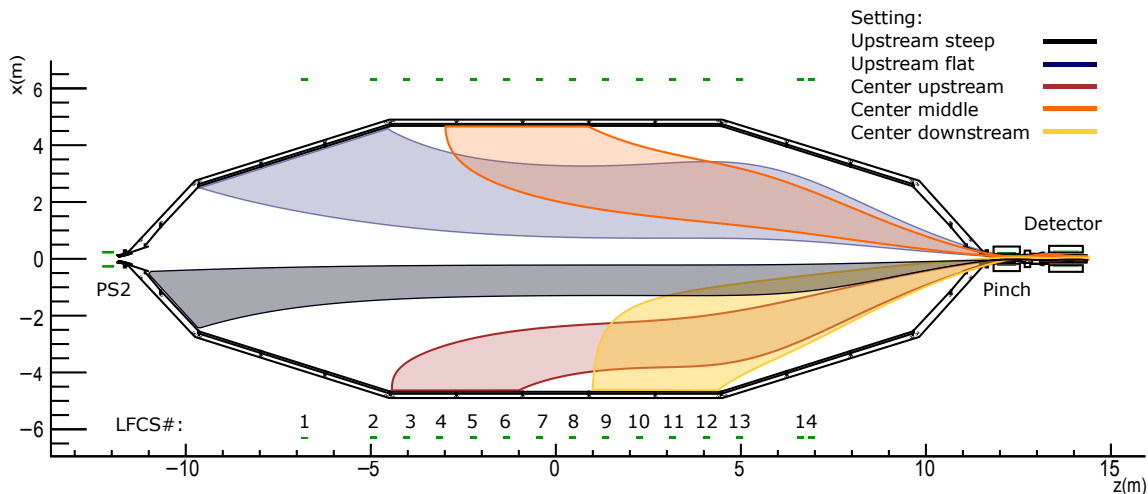


Figure 4.2: **Observed spectrometer surface areas for the asymmetric magnetic field settings in SDS-IIb.** The observed areas of the respective magnetic field settings (see Tab. 4.1) are derived from field simulations with KASSIOPEIA for an aligned setting. For overview reasons the observed areas are respectively shown on the upper and the lower spectrometer surface in this picture. The coils of the magnetic system are illustrated in green, whereby the PS1 magnet is not drawn.

the pre-spectrometer and are operated at a nominal Field of  $B_{PS} = 4.5$  T. In order to reach the very high fields, the magnets are cooled down to an operation temperature of less than 4.2 K, using a two-stage cryo-cooler device [26]. Both magnets are operated in driven mode. Although, the pre-spectrometer vessel was not installed during measurement phase SDS-IIb, to create the final field configurations, both magnets were placed to their nominal positions in the final measurement setup. However, due to maintenance operations in the spectrometer building the PS1 magnet had to be switched off during some of the measurements. As these were performed for asymmetric magnetic field settings the absence of the PS1 magnet had only minor effects on the shape of the magnetic field and is negligible. On the downstream side of the spectrometer, two superconducting magnets are located, the Pinch magnet, which, together with the PS2 magnet, is responsible for the magnetic field of the MAC-E filter principle inside the main spectrometer, and the Detector magnet, which leads to the imaging of the magnetic flux tube on the detector wafer. The maximum magnetic field of both magnets is 6 T. However, the nominal field of the detector magnet will be 3.6 T in the measurements [50] [51].

The very small magnetic field in the analyzing plane of the main spectrometer makes it very sensitive to external influences. One major interference factor is the earth magnetic field with a contribution of  $43.6 \mu\text{T}$  in vertical direction and  $5 \mu\text{T}$  in horizontal direction, relative to the axis of the spectrometer [52]. These fields are canceled by a system of compensatory coils, arranged around the spectrometer vessel, called the Earths Magnetic Field Compensation System (ECMS). The induced fields are adjusted carefully and were not varied during the of SDS-IIb measurement phase.

Fourteen further air coils surround the spectrometer vessel coaxially with a diameter of 12.6 m, called the Local Field compensation System (LFCs). The LFCs is used to fine-tune the shape of the magnetic flux tube inside the spectrometer and to change the magnetic field strength in the analyzing plane in the range from 3.3 G to 10 G by adjusting the currents in the coils up to 100 A. The coil, located closest to the Pinch magnet, is used as a counter measure to compensate the influence of the maximum field of the Pinch magnet on the symmetry of the flux tube in the spectrometer [53] [54]. In the case of asymmetric

Table 4.1: **Magnet currents of the asymmetric magnetic field settings used in the SDS-IIb measurement phase.** The respectively observed areas of the inner spectrometer surface are illustrated in Fig. 4.2. In order to exclude irrelevant areas in the respective magnetic field settings only distinct detector pixel rings are considered in the data analysis.

Magnet	Upstr. steep	Upstr. flat	Center upstr.	Center mid.	Center downstr.
	Currents (A)				
PS1	0.0	0.0	157.0	157.0	157.0
PS2	0.0	0.0	157.0	157.0	157.0
LFCS 1	98.0	0.0	-98.0	-98	-98.0
LFCS 2	98.0	0.0	-70.0	-98.0	-98.0
LFCS 3	98.0	0.0	0.0	98.0	-98.0
LFCS 4	98.0	98.0	0.0	-70.0	-80.0
LFCS 5	98.0	98.0	30.0	0.0	-60.0
LFCS 6	98.0	98.0	60.0	0.0	-60.0
LFCS 7	98.0	98.0	60.0	0.0	-60.0
LFCS 8	98.0	98.0	60.0	0.0	-30.0
LFCS 9	98.0	98.0	60.0	0.0	0.0
LFCS 10	98.0	98.0	60.0	40.0	40.0
LFCS 11	98.0	0.0	0.0	40.0	40.0
LFCS 12	98.0	0.0	0.0	60.0	40.0
LFCS 13	50.0	0.0	0.0	60.0	40.0
LFCS 14	0.0	0.0	0.0	0.0	0.0
EMCS vert.	50.0	50.0	50.0	50.0	50.0
EMCS horiz.	9.0	9.0	9.0	9.0	9.0
Pinch	87.15	87.15	87.15	87.15	87.15
Detector	56.154	56.154	56.154	56.154	56.154
Det. rings	0-5	2-13	4-13	2-13	1-13

measurements, as partially performed during the SDS-IIb measurement phase, the LFCS is used to adjust the area of the inner surface of the main spectrometer that is imaged onto the FPD, as shown in Fig. 4.2. The respective magnetic field settings are listed in Tab. 4.1.

### 4.3 High-voltage concept

The entire spectrometer vessel can be elevated to negative voltages down to  $-35$  kV, in order to provide the retarding potential, required for the MAC-E filter measurement principle. For this reason the vessel support structure contains ceramic insulators, preventing the vessel from being electrically grounded. Furthermore, ceramic cones on both ends of the spectrometer isolate it from the pre-spectrometer and the FPD system, which are on different electrical potentials. In order to fine-shape the potential in the spectrometer and to compensate inhomogenities an electrode system was installed on the inner surface of the vessel. It consists of 248 modules, one shown in Fig. 4.3, containing a total of 23 000



Figure 4.3: **A photograph of a double-layer wire electrode module** from the cylindrical part of the main spectrometer. The wires are stretched between the comb-like structures. From [26].

wires, arranged coaxially around the axis of the spectrometer. In the center and flat cone parts of the spectrometer the modules contain two wire layers with respectively 15 cm and 22 cm distance to the spectrometer surface. In the steep cone parts, only one wire layer is installed.

A further task of the inner electrode system is to prevent electrons emitted from the surface of the spectrometer from entering the sensitive volume, by operating the system on a slightly more negative potential than the retarding potential of the spectrometer. The maximum possible potential difference between the spectrometer and the inner electrode system is 1 kV. For measurements with asymmetric fields the shielding of secondary electrons from the surface, due to the inner electrode system is important, as the magnetic shielding is not provided in this case. For the SDS-IIb measurement phase, experiments were conducted to use the inner electrode system as a retarding potential for electrons from the surface, in order to determine their kinetic energies. For this purpose, a modified arbitrary waveform generator (Agilent 33220a [55]) was used, to apply the very small potential offsets.

On both ends of the spectrometer a titanium anti-Penning electrode and an aluminum ground electrode are installed to prevent Penning traps, induced by the very high electric and magnetic fields in this regions.

A further high-voltage component is part of the FPD system. The post-acceleration electrode (PAE) is a trumpet-shaped copper electrode, accelerating electrons arriving from the spectrometer by up to 30 keV [50]. It is located directly in front of the detector and has two primary purposes. Firstly, increasing the kinetic energy of electrons from the spectrometer allows them to be distinguished from the ambient electron backgrounds. Secondly, the boost in axial direction leads to a decreased incident angle of the electrons on the detector, reducing the probability of backscattering from the wafer. Although, the post-acceleration electrode is designed for voltages up to 30 keV, this potential could not be reached, due to break-downs, the cause of which is not yet understood. For this reason, the post-acceleration electrode was operated at a potential of 10 keV during the entire SDS-IIb measurement phase.

## 4.4 Detector and data acquisition

The electrons, that pass the retarding potential of the spectrometer and the magnetic mirror, induced by the Pinch magnet, are counted by a monolithic array of PIN diode

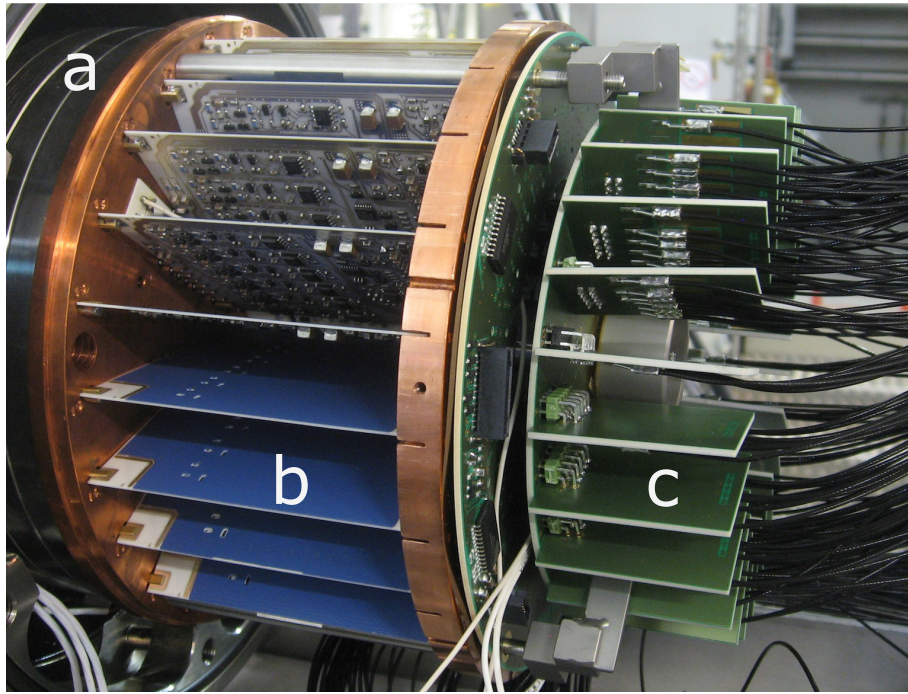


Figure 4.4: **A photograph of the detector readout electronic in the HV chamber** with a) the signal feedthrough flange, mounted to the post-acceleration electrode, b) the 24 preamplifier cards and c) the power distribution boards and cable harness. Adapted from [26].

detectors fabricated on a wafer with a thickness of  $500\ \mu\text{m}$  and a diameter of  $125\ \text{mm}$ . The semiconductor is realized with a  $n^{++}$ -type side, facing the spectrometer and a p-type backside which is segmented into 148 pixels. The pixels have an area of  $44.1\ \text{mm}^2$  and are arranged in twelve concentric rings, each containing twelve pixels, and four bulls-eye pixels in the center. The charge, induced by an electron, arriving on a detector is collected on the backside of the wafer, due to the applied bias voltage of nominally  $100\ \text{V}$ . Each pixel is read out separately via electrical feedthrough pins. These pins are mounted on a feedthrough flange, shown in Fig. 4.4, that separates the UHV and HV chamber and is directly mounted to the post-acceleration electrode. On the backside of the feedthrough flange 24 preamplifier cards are directly connected to the pins. 24 power distribution boards and a cable harness connect the modules to a further feedthrough flange, that connects the HV chamber with the ambient air electronics. As the entire detector read-out components are on the same potential as the post-acceleration electrode, the signals are converted to optical signals, so they can be led via optical fiber links to the grounded data acquisition (DAQ). The ambient-air electronics additionally contains the second amplification stage in the read-out chain. In the DAQ rack, the optical signals are again transformed to analog, before they are finally digitized in the DAQ system.

The DAQ system consists of eight first-level trigger (FLT) cards and one second-level trigger (SLT) card. Each FLT card serves eight detector channels and determines the event energy and event time from the incoming data with very high precision. All FLT cards are initialized, synchronized and coordinated by a single computer housed on the SLT card. The transfer of the signal data from the SLT card to the DAQ computer is the final step in the data acquisition chain of the FPD system. On the DAQ computer, the software package ORCA serves to control the FLT and SLT cards and to process the incoming data in real-time.

During the SDS-IIb measurement phase one of the preamplifier cards, directly connected to

the feedthrough pins, induced a very high noise signal. For this reason, the respective pixels are excluded in the analysis. The maintenance of the FPD system after the measurement phase showed that the preamplifier module was broken due to mechanical stress [50] [51].



## 5. The background model for the main spectrometer

In chapter 3 it is shown that the influence of a non-zero neutrino rest mass on the shape of the  $\beta$ -spectrum of tritium is largest at the endpoint at about 18.6 keV. However, the rate of  $\beta$ -electrons with such energies is very small such that the background rate in this energy region must be reduced to 10 mcps in order to achieve a reasonable signal-to-noise ratio[37]. With its large volume of about 1240 m<sup>3</sup> and an inner surface of about 1240 m<sup>2</sup> the main spectrometer represents the largest contributor to the total background rate in the KATRIN experiment. In this chapter the current background model for the main spectrometer is discussed, based on measurement results of the two commissioning phases SDS-I and SDS-II. Section 5.1.1 focuses on a background contribution due to stored particles and the effectiveness of potential countermeasures. In section 5.2 a model, based on secondary electrons emitted from inner surfaces, and the characteristics of the remaining non-radon induced background are described. Finally, a recently established theory, which links background generation in the main spectrometer to Rydberg atoms is presented in section 5.3.

### 5.1 Stored-particle induced background

In spectrometers of the MAC-E filter type the electromagnetic fields can cause electrons to be trapped over long timescales. Due to the ionization of residual gas molecules, these electrons can generate low-energy background electrons. In the following, the two storage mechanisms of relevance for the main spectrometer, namely Penning traps and the magnetic bottle effect are introduced, before the origin of the stored particles is discussed and potential countermeasures are presented.

#### 5.1.1 Penning traps

A Penning trap is a combination of an electric and a magnetic field in an explicit volume as shown in Fig. 5.1. Electrically charged particles are trapped inside this volume due to the applied fields: The electric field between the two cathodes traps a free low-energy electron to the center of the volume in longitudinal direction, while the magnetic field prevents a motion in radial direction due to the Lorentz force. Therefore, electrons with low kinetic energies are forced on cyclotron trajectories along the magnetic field lines, bouncing back and forth between the two cathodes. While stored, the electrons can ionize

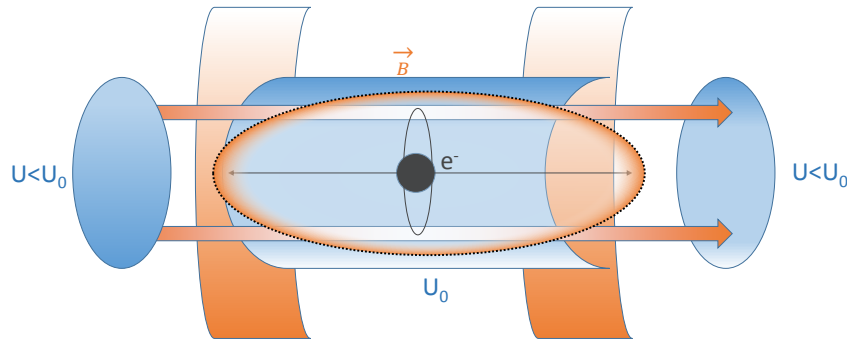


Figure 5.1: **Schematic drawing of a penning trap.** The electrodes (blue) and coils (orange) generate the electromagnetic fields which trap the electrons in the central volume (dotted line).

residual gas molecules, thus, generating secondary electrons and positively charged ions. The generated electrons are also stored in the Penning trap whereas the ions can leave, resulting in a negative space charge in this small volume. The resulting unstable plasma can lead to a vacuum breakdown, releasing a large number of electrons. The result are large background rates which can in extreme cases damage the experimental setup, especially the detector [56].

### 5.1.2 Magnetically stored particles

While the inhomogeneous magnetic fields of the main spectrometer result in the desired adiabatic collimation of the momentum of signal electrons into longitudinal direction (see chapter 3), they form a highly effective magnetic bottle for low-energy electrons that are created in the central volume of the main spectrometer. Fig. 5.2 illustrates the trajectory of such a stored electron. While being reflected on both ends of the spectrometer due to the magnetic mirror effect the cyclotron motion of the electron around the magnetic field line is superimposed by the characteristic magnetron motion around the center axis of the spectrometer, caused by the  $\nabla \vec{B} \times \vec{B}$ -drift in the inhomogeneous fields. According to [26] the trapping condition for a particle of charge  $q$  generated at position  $\vec{x}$  in such a magnetic bottle is given by

$$\theta > \theta_{\max} = \arcsin \left( \sqrt{\frac{qU(\vec{x})}{E_{\text{kin}}(\vec{x})} \cdot \frac{B(\vec{x})}{B_{\max}}} \right), \quad (5.1)$$

where  $\theta$  is the polar starting angle of the particle with respect to the magnetic field lines,  $U(\vec{x})$  is the electrostatic potential, and  $B(\vec{x})$  is the magnetic field strength.

There are two possible ways for an electron to leave the magnetic bottle. Firstly, the stored electron can collide with a part of the spectrometer geometry or secondly, it breaks the storage condition given in Eq.5.1.2. This can happen in two ways, either by a change of the electron's kinetic energy or its polar angle. For energies lower than 10 eV [39], the cross-sections for elastic and inelastic scattering of the electrons with residual gas molecules gets dominant compared to the emission of synchrotron radiation and becomes the major cool down mechanism. In inelastic scatterings low-energy secondary electrons are created,

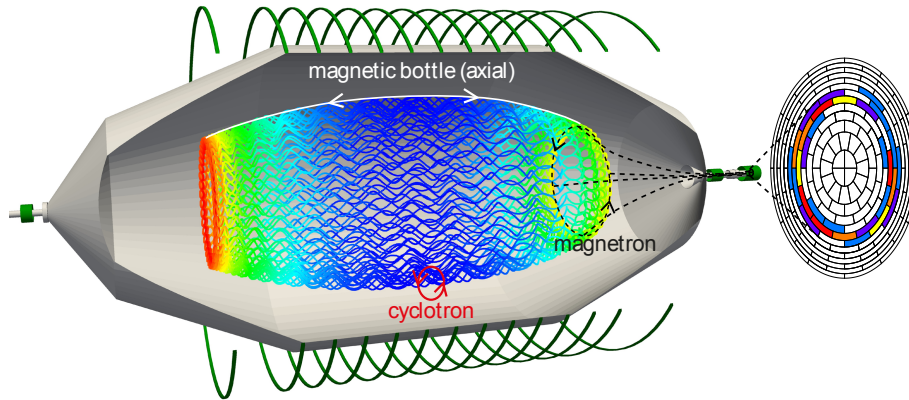


Figure 5.2: **Trajectory of a stored electron in the KATRIN main spectrometer and the associated characteristic event pattern on the detector.** The motion of the electron is a superposition of the reflection between the two magnetic mirrors on both sides of the spectrometer, the fast cyclotron motion around the magnetic field line, and the slow magnetron drift around the spectrometer axis. The electron cools down due to cyclotron radiation and scattering with residual gas molecules. The latter can lead to the ionization of the molecules, generating secondary electrons along the trajectory of the stored primary electron. When leaving the trap, these low-energy secondaries form a ring shaped event pattern on the detector. Adapted from [51].

which can, depending on their initial kinetic energy and polar angle, be stored as well and create further tertiary electrons and so on. All electrons created in this way share the same magnetron radius as the primary electron. If these time correlated low-energy electrons leave the trap towards the detector they create a characteristic ring shaped event pattern as shown in Fig. 5.2. However, due to the UHV conditions, the cool-down process of the primary electron can take minutes to hours, such that the secondary electrons created by one stored primary arrive on the detector over a long period of time and cannot be differentiated from other background electrons on an event by event basis. For a pressure of  $p \approx 10^{-10}$  mbar, the average storing time of the electrons ranges from 10 s to 3 h [51].

In order to preserve the correlation between the events from one stored particle, the cool-down mechanism must be accelerated. Therefore, during the spectrometer commissioning measurements, the pressure in the vessel was artificially increased to a constant value of  $p \approx 10^{-8}$  mbar via He or Ar injection. According to [39] the mean time between two scatterings of a stored electron with residual-gas molecules scales antiproportional with the pressure in the spectrometer. Thus, by increasing the pressure in the spectrometer by a factor of 100 the average storing time of a high-energy electron is reduced by two orders of magnitude to the (sub-)second scale. This allows to identify all background events from one stored primary electron as short bursts of events on the detector with the characteristic ring shaped event pattern.

Fig. 5.3 shows the rate on the detector as a function of time for nominal and for elevated pressure. One can clearly see the bursts of events for elevated pressure. In the latter case, each spike in the event rate corresponds to at least one stored electron in the spectrometer and can be differentiated from the remaining uncorrelated background in the analysis. In the following these spikes will be denoted as event clusters.

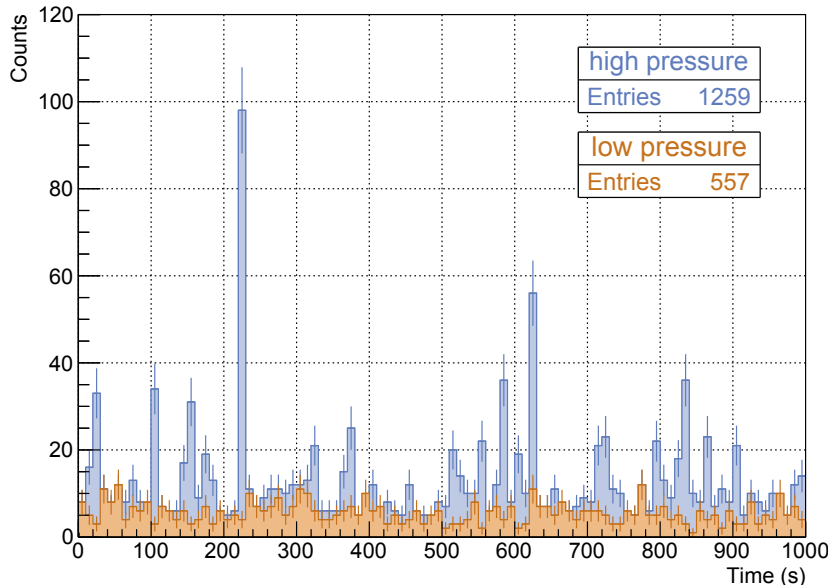


Figure 5.3: **Background rate measured at normal and elevated spectrometer pressure.** The event rate on the detector at normal ( $\approx 10^{-10}$  mbar) pressure appears flat, while short event bursts are observed at elevated ( $\approx 10^{-8}$  mbar) pressure. Each burst can be identified as a single Rn-decay in the spectrometer volume. Adapted from [26].

### 5.1.3 The radioactive decay of radon in the spectrometer

The main source for stored electrons in the spectrometer are radioactive decays in the vessel volume. The major contributors here are the Radon isotopes  $^{219}\text{Rn}$ ,  $^{220}\text{Rn}$ , and  $^{222}\text{Rn}$  which decay via an  $\alpha$ -decay that is accompanied by the emission of electrons with energies in the eV-keV regime [39]. However, due to its rather long half-life of 3.82 days the naturally most abundant  $^{222}\text{Rn}$  is essentially pumped out by the main spectrometer turbo-molecular pumps, long before it can decay. There are two main emanation sources for the short-lived  $^{219}\text{Rn}$  ( $T_{frac12} = 3.96$  s) and  $^{220}\text{Rn}$  ( $T_{frac12} = 55.6$  s) in the main spectrometer: Firstly, the emanation of both isotopes from the stainless-steel surfaces in the spectrometer vessel and secondly, the emanation of  $^{219}\text{Rn}$  from the NEG material of the getter pumps (see section 4.1). According to [26], the latter represent the main source of Rn-emanation.

Since the Radon atoms are electrically neutral they are not influenced by the electromagnetic fields in the main spectrometer and enter the magnetic flux tube undisturbed. When they decay, the produced electrons are very likely to be stored in the spectrometer volume generating the characteristic stored-particle induced background discussed previously.

### 5.1.4 Radon reduction by a LN<sub>2</sub>-cooled baffle system

In order to prevent the radon atoms that emanate from the NEG material from entering the spectrometer, a LN<sub>2</sub>-cooled baffle-system is installed in each of the three main pump ports of the spectrometer (see section 4.1). It blocks the direct line-of-sight from the NEG pumps to the spectrometer volume. In this way, radon atoms will stick to its copper surfaces, which are cooled down to LN<sub>2</sub>-temperature and will decay there, far outside the sensitive flux-tube. In SDS-II this baffle system was fully operational for the first time such that its effectiveness as a passive radon countermeasure could be investigated

in a series of dedicated background measurements at elevated pressure. It was found that the radon-induced stored-particle background is reduced with an efficiency of  $95.1 \pm 0.3\%$  when all three baffle systems are operated cold. However, even with cold baffles a remaining background level of:

$$R = \frac{142 \text{ pixels}}{148 \text{ pixels}} \cdot (691 \pm 1) \text{ mcps} = (664 \pm 1) \text{ mcps} \quad (5.2)$$

was observed for 142 working detector pixels in SDS-IIA which cannot be related to stored particles.

## 5.2 Characteristics of the non radon-induced background

With the enormous dimensions compared to its predecessor experiments, the KATRIN main spectrometer not only covers a large volume, but also about  $1240 \text{ m}^2$  of inner surfaces. Being unshielded, these surfaces are exposed to a large flux of cosmic muons and  $\gamma$ -photons from environmental radiation. Prior to the SDS-II measurements, the immense number of low-energy electrons generated at the inner spectrometer surfaces due to the interaction of the muons and  $\gamma$ -photons with the stainless steel were suspected to be responsible for the remaining background with cold baffles.

In order to characterize the remaining background in detail, several key operating parameters of the spectrometer and detector section were varied during SDS-IIa background measurements. While a detailed overview of these measurements can be found in [26], the most valuable findings are summarized in the following and are compared to the expectations for a direct background contribution by secondary electron emission.

### 5.2.1 Impact of the magnetic shielding

One parameter that was varied in the SDS-IIa background measurements is the magnetic field strength in the main spectrometer in order to investigate the impact of the magnetic shielding on the non-radon induced background. The variation of the magnetic field also changes the observed volume in the spectrometer, which is determined by the shape of the magnetic flux tube. This shape is defined by the superconducting solenoids on the up- and downstream side of the spectrometer and the air coil system (see section 4.2). The upper part of Fig. 5.4 shows the observed magnetic flux tube for a 3.8 G and a 9 G magnetic field strength in the analyzing plane. The measured rates are  $890 \pm 5$  mcps for the 3.8 G setting and  $349 \pm 3$  mcps for the 9 G setting [26]. The lower part of Fig. 5.4 shows the background rate per detector pixel ring, normalized to the respective observed flux tube volume. The x-axis is scaled to the radial extension of the flux tube in the analyzing plane of the main spectrometer. Surprisingly, there are only small differences in the two distributions, that can be traced back to rate fluctuations. This observation leads to two insights: Firstly, the difference in the magnetic mirror effect, due to the two chosen settings, has an almost insignificant influence on the measured background rate, which has the consequence that the observed background signal consists of low-energy electrons, as the magnetic mirror effect is negligible for the latter. Secondly, this measurement shows that the non-radon induced background scales with the flux tube volume. As a consequence, the background electrons seem to be generated homogeneously distributed in the spectrometer volume, an observation which stands in contrast to low-energy secondary electrons emitted from the vessel walls as main background source.

### 5.2.2 Impact of the electrostatic shielding

One essential reason for installing the advanced inner electrode system (IE) in the KATRIN main spectrometer is the shielding of low-energy secondary electrons emitted from the walls

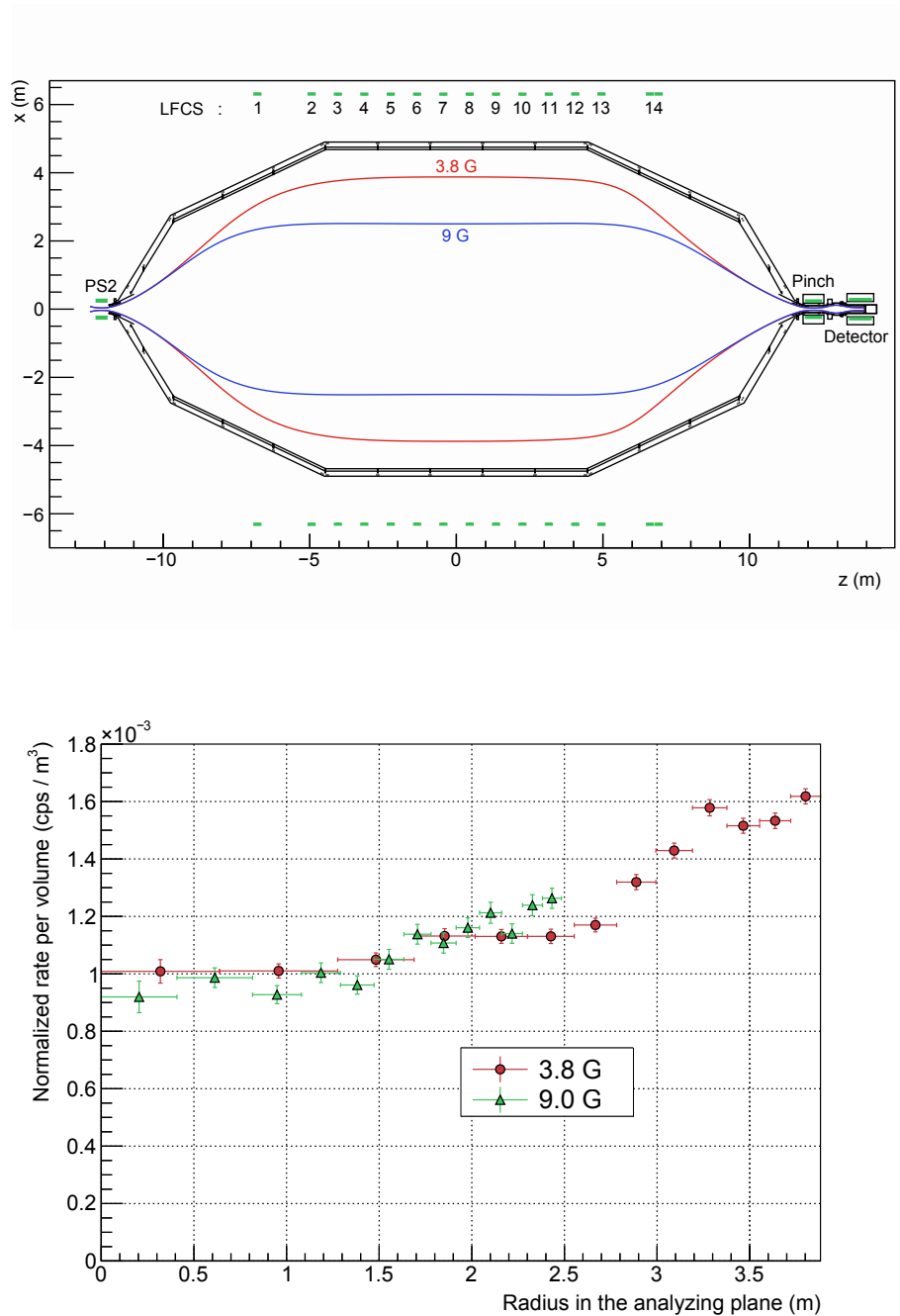


Figure 5.4: **Dependency of the background rate on the magnetic field strength in the analyzing plane. Top:** Extension of the observed magnetic flux tube for two different magnetic field strengths in the analyzing plane, simulated with KASSIOPEIA. **Bottom:** The radial dependence of the volume-normalized background rate for the 3.8 G and the 9 G magnetic field strength in the analyzing plane. The volumes are calculated using KASSIOPEIA. Adapted from [26]

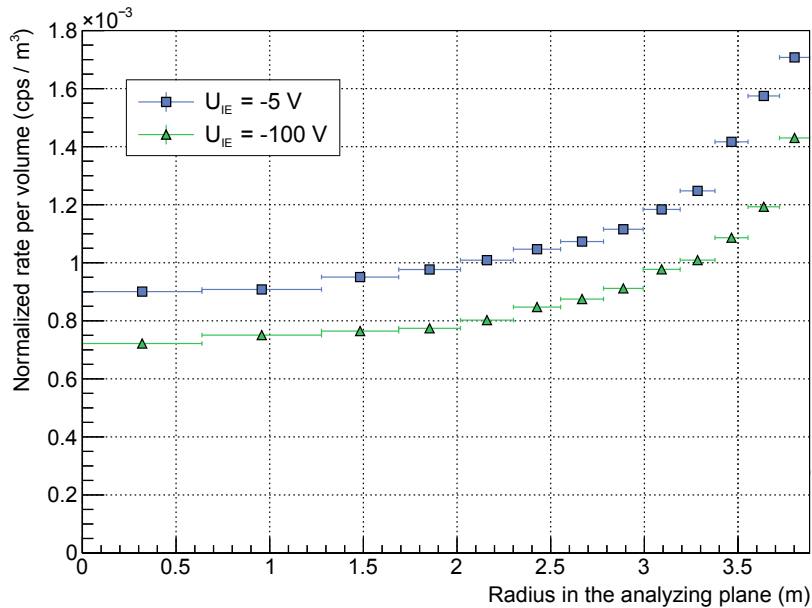


Figure 5.5: **Influence of the IE offset potential on the measured background rate.** The radial dependence of the volume-normalized background rate in the analyzing plane for two inner electrode potentials are shown. The reduction of the background due to a higher shielding potential appears almost independent of the radius in the analyzing plane. Adapted from [26]

of the vessel. For measurements with a symmetric magnetic field setting the electrostatic shielding of secondary electrons from the surface is supplemented by the magnetic shielding effect. Therefore, the background reduction effect an increased IE offset potential should be less than in an asymmetric measurement configuration. Fig. 5.5 shows the volume-normalized electron rate per pixel-ring on the detector for two different negative offset potentials on the inner electrode and the respective radius of the observed flux tube in the analyzing plane. While the total background rate decreases with increasing IE offset potential as expected for a secondary electron induced background, both measurements show a similar radial dependence of the background. This observation is rather surprising as one would expect to see a larger rate reduction on the outer detector rings than in the central part of the magnetic flux tube which can hardly be reached by the low-energy secondary electrons from the spectrometer walls via the slow radial drift processes. More likely, these electrons will break their storage condition at an early stage of the drift and will arrive on the outer detector rings. Thus, the radially independent reduction effect of the inner electrode shielding potential points to a background source, other than low-energy secondary electrons from the spectrometer walls.

### 5.2.3 Impact of a vacuum bake-out

In this section the influence of the conditions on the inner spectrometer surfaces on the non-radon induced background is investigated. Therefore, the data from before and after the vacuum bake-out of the spectrometer are compared. The main aim of a vacuum bake-out is to reduce the amount of water molecules adsorbed on the inner surfaces of the spectrometer to achieve a better vacuum in the vessel. While the impact of an improved pressure in the spectrometer on the background is discussed in detail in [26], the changed surface conditions in the spectrometer also influence the background level as it is shown in in Fig. With the pressure in the spectrometer being the same for both measurements,

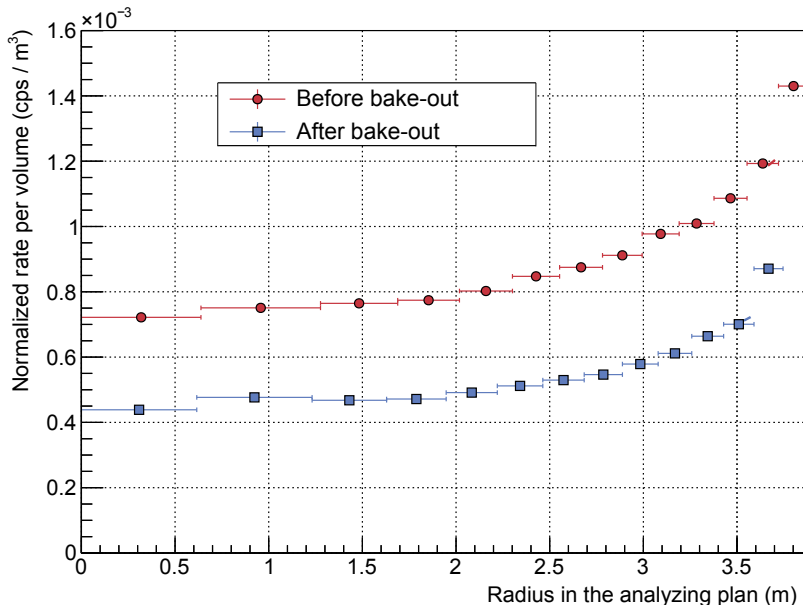


Figure 5.6: **Influence of the vacuum bake-out on the background in the spectrometer.** The volume-normalized background rate per detector ring before and after the vacuum bake-out of the main spectrometer is shown. Both measurements were carried out at a 3.8 G magnetic field strength in the analyzing plane and a  $-100$  V potential on the inner electrode, and most importantly at comparable pressures in the spectrometer. Adapted by [26]

one can see that the background is reduced by about 40% [26]. Interestingly, the radial shape of the background distribution remains the same before and after the bake-out. This points out that the background level in the main spectrometer is still dominated by the same source after the bake-out.

### 5.3 The Rydberg background model

Summarizing the results of the detailed background characterization performed during the SDS-IIa measurements one can state that the remaining background with cold baffles is being produced homogeneously distributed in the whole spectrometer volume but is at the same time linked to the conditions on the spectrometer surfaces. This observation together with the radial independent reduction of the background with increasing IE offset potential excludes secondary electrons emitted from the spectrometer surfaces as main source of the background. Instead it will be shown in the following that a newly established background model with neutral messenger particles emitted from the spectrometer walls, entering the magnetic flux tube and emitting low-energy electrons can explain all of the previously discussed characteristics of the non-radon induced background in the main spectrometer. For simplicity reasons the model will be explained for highly excited Rydberg atoms as messenger particle.

In this model, the Rydberg atoms are highly excited hydrogen atoms, as atomic hydrogen is adsorbed in large quantities in the stainless steel surfaces of the main spectrometer. This assumption can be affirmed with the impact of the vacuum bake-out of the spectrometer as it reduced both, the total background rate and the amount of adsorbed hydrogen on the inner surfaces of the spectrometer. As the Rydberg atoms have no electrical charge, they are not shielded from the sensitive volume of the spectrometer, due to the magnetic

and electrostatic shielding mechanisms. This fits well with the findings on the behavior of the observed background to the impact of the applied IE potential and the magnetic field strength in the analyzing plane.

The production mechanisms of Rydberg atoms are based on charge exchange with ions, electron impact, or photoexcitation [57]. Electrons, colliding with the hydrogen molecules spectrometer surfaces and hence creating Rydberg atoms require kinetic energies of  $E > 20$  eV. However, the number of electrons in this energy range is not sufficient to explain the current background in the main spectrometer. Furthermore, UV-photons are excluded as mechanism for the production of Rydberg atoms, as no observation of photons in the respective energy range was made during several measurements. For this reason, cosmic muons, high-energetic  $\gamma$ -radiation and ions are remaining as potential excitation processes for the Rydberg atoms.

The high excitation of Rydberg atoms implies very high dipole moments, the consequence being that they are very sensitive to electromagnetic fields, such as black body radiation photons [58]. In the case of an ionization of the Rydberg atom due to black body radiation at room temperature, the energy of the emitted electron is in the meV-regime [57], what agrees with the results of the measurement with varied magnetic field configurations. In order to investigate the ionization of the Rydberg atoms by photons from black-body radiation the temperature in the spectrometer was varied. In fact a change in the background rate could be measured, but it is not totally clear, if the reduction is an outcome of the changed black-body radiation properties or the changed pressure in the spectrometer, which depends on the temperature [26].

Another mechanism to ionize the Rydberg atoms is the selective field ionization. In the center of the spectrometer, the static electric field strength is very small, whereby the black-body radiation is the dominant effect for ionization. However, on both ends of the spectrometer and between the vessel wall and the wire layers of the inner electrode system, the influence of the electric fields is stronger. The presence of an electric field changes the Coulomb potential of the Rydberg atoms, resulting in lower ionization energies. Thus, highly excited states are ionized without the interaction of a photon. This can explain the characteristics of the non-radon background measurements in dependence on the inner electrode potential.

One can see that the newly established background model with Rydberg atoms fits the characteristics of the non-radon induced background very well. However the generation mechanism of the Rydberg atoms on the spectrometer surface is still not understood. For that reason, in the following the characteristics of secondary electrons from the spectrometer surface are investigated as they might be a byproduct in the Rydberg atom emission from the spectrometer walls and therefore, give further information on the latter.



## 6. Characteristics of secondary electron emission

In the previous chapter it is shown that besides the radon-induced background an additional source in the spectrometer creates low-energy electrons which are detected at the FPD in the energy region of interest for the KATRIN experiment. Due to several characteristics of the remaining background, derived from various measurements, a background model based on Rydberg atoms, created on the inner spectrometer surface was established. In order to test this model the emission of secondary electrons, likely accompanying the Rydberg production process, is investigated.

Therefore, specific measurements were performed, described in section 6.1. After investigating the spatial distribution (section 6.2) of the secondary electrons, the impact of the inner electrode offset potential (section 6.4) and the spectrometer potential (section 6.3) on their rate are examined, in order to determine further information on their characteristics. From the temporal analysis (section 6.5) of the secondary electron emission a distinct spatial coherence could be found. As a main part of this thesis an algorithm was developed to identify the spatial distributions and to facilitate further analysis methods (section 6.6).

### 6.1 Measurement principle

In summer of 2015 the measurement phase SDS-IIb was conducted which had the aim to investigate potential sources of the background based on the newly established Rydberg model. In order to characterize and identify the production mechanism of the Rydberg atoms, this thesis concentrates on the analysis of secondary electrons, generated at the spectrometer surfaces as a byproduct of the Rydberg atom generation. Therefore, the main spectrometer and detector section was operated at the standard high voltage mode. The mean pressure during the entire measurement phase was about  $6 \cdot 10^{-11}$  mbar. Additionally the baffle system was fully operational so the radon induced background was set to a minimum of  $36 \pm 18$  mcps, according to [26]. In contrast to the previous measurement phase SDS-IIa a vacuum bake-out of the spectrometer was performed in order to reduce the amount of water on the stainless-steel surface so the condition of the main spectrometer surface is different for the two periods. The PAE potential was set to a constant value of +10 kV. The offset potential of the inner electrode was fully operational and due to the operation with a modified waveform generator (Agilent 33220a [55]) it was possible to set very small offset potentials (from +300 mV to  $-10$  V in 10 mV-steps).

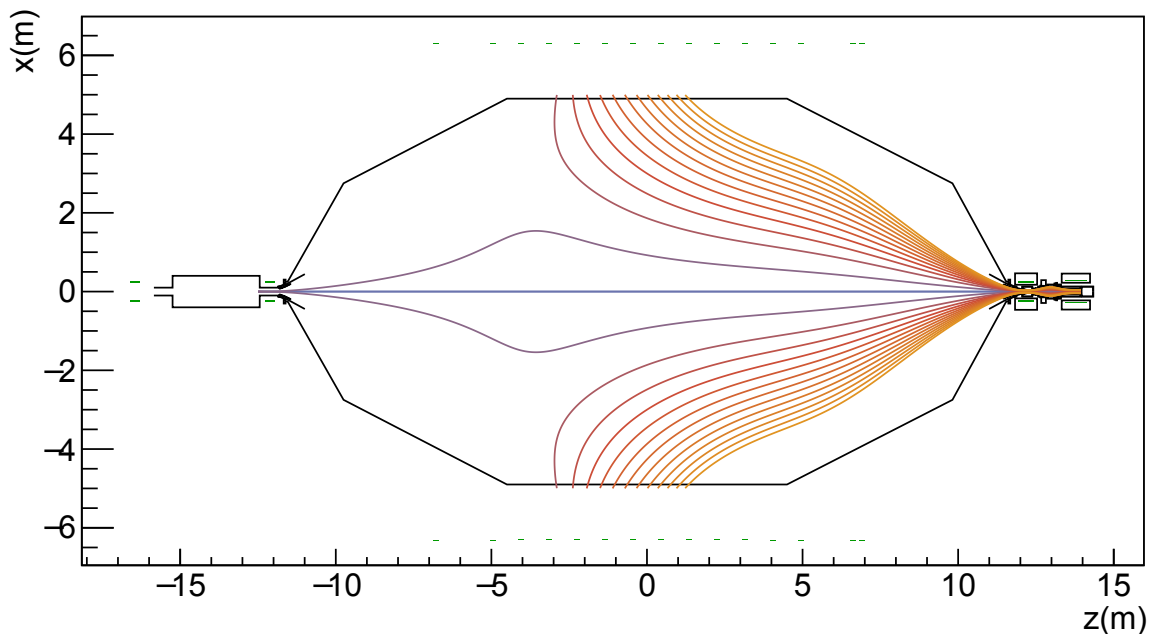


Figure 6.1: **Asymmetric magnetic field setting "middle"**. The colored lines represent the magnetic field lines impinging on the boundary between detector rings simulated with KASSIOPEIA. The coils of the pre spectrometer magnets and the detector magnets, as well as the LFCS system are shown in green.

Table 6.1: **Measurement settings to characterize the secondary electron emission from the inner spectrometer surface.** All measurements were performed during the SDS-IIb measurement phase at a pressure of  $p_0 \approx 5 \cdot 10^{-11}$  mbar and cold baffles. The currents of the pre spectrometer and detector magnets and the air coil system were set such that different spectrometer areas were projected on the detector (see chapter 4). The inner electrode offset potential was operated with a waveform generator in order to provide the required small voltages.

Measurement set	Magnetic field setting	$U_{\text{vessel}}$ (kV)	$U_{\text{IE}}$ (V)	Runs
A	Center middle	-18.6	variable (0.1 - -10.0)	#25104 - #25119 & #25132 - #25143
B	Center upstream	-18.6	variable (-0.0 - -5.0)	#25120 - #25122
C	Center downstream	-18.6	variable (-0.0 - -5.0)	#25123 - #25125
D	Center middle	variable (-2.0 - -18.6)	-0.0/-5.0	#25144 - #25153

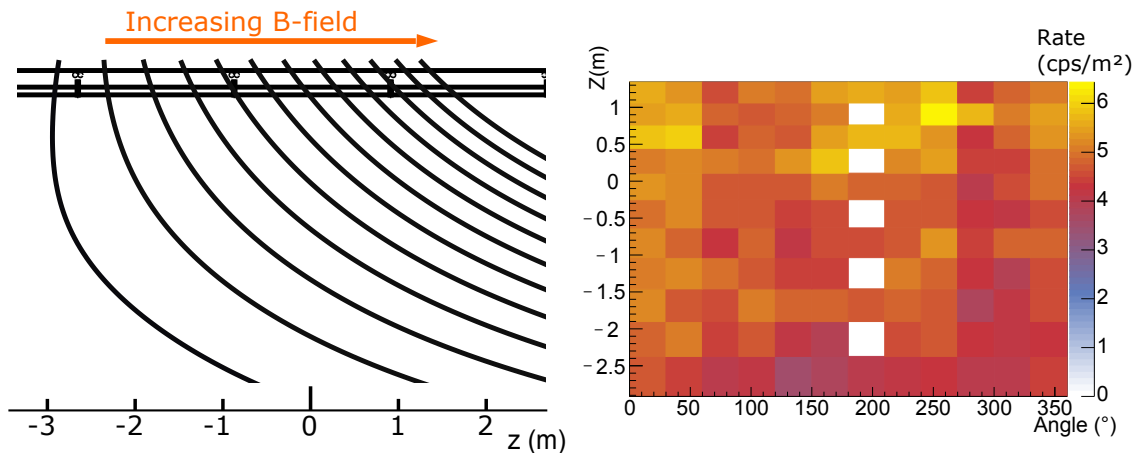


Figure 6.2: **Emission of secondary electrons on the inner main spectrometer surface.** **Left:** The extract of the spectrometer is shown, that is projected on the focal plane detector, due to the asymmetric magnetic field setting of measurement set B. Areas between two field lines correspond to the related detector ring. The orange arrow indicates the increasing magnetic field for locations closer to the Pinch magnet. ( $B(z = -3\text{ m}) = 0.02\text{ mT}$ ;  $B(z = 1.5\text{ m}) = -0.25\text{ mT}$ ) **Right:** The event rate, measured on the detector is translated to a two-dimensional surface map of the spectrometer for secondary electron emission. The rate is normalized with the respectively observed area. The five white pixels, are excluded from the analysis, due to a broken pre amplifier module. The increased rate towards the downstream side may be explainable with the magnetic mirror effect.

In order to observe the secondary electrons from the spectrometer surface an asymmetric magnetic field setting was used, schematically shown in Fig. 6.1. By changing the magnetic setting the observed surface of the spectrometer can be shifted into up- and downstream direction. The observed secondary electron rate from the spectrometer surface for the magnetic field setting "Center middle" and 142 working pixels is:

$$R = (666.7 \pm 0.5)\text{ cps} \quad (6.1)$$

Comparing this electron rate to the radon induced background leads to the insight that the latter can be neglected in this analysis, especially since the observed volume is smaller than in measurements with a symmetric magnetic field setting. Furthermore, the asymmetric magnetic field prevents the storage of charged particles, which is essential for the background signal based on radon decays.

## 6.2 Spatial distribution of the secondary electrons

Due to the segmentation of the detector wafer into 148 pixels a good resolution on the projection of the observed surface of the spectrometer onto the FPD can be achieved. Fig. 6.2 shows the rate of the secondary electrons from the spectrometer surface measured on the detector for the individual detector pixels. The translation in spectrometer coordinates was derived from field line simulations using KASSIOPEIA. The exclusion of the five pixels at  $180^\circ$  are due to a broken pre amplifier module (section 4.4). As apparent from the left picture in Fig. 6.2 the areas projected on the detector have different sizes, resulting in an increased rate for pixels on the inner detector rings, which observe areas further upstream

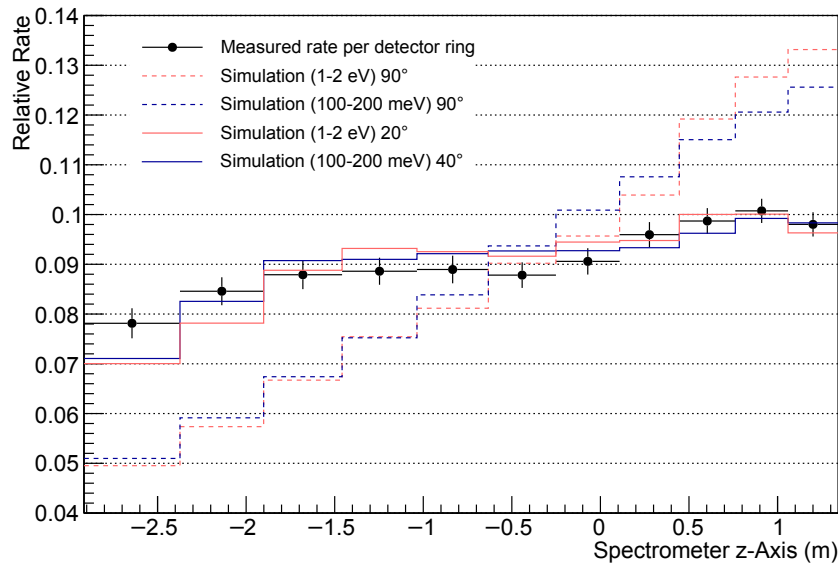


Figure 6.3: **Axial secondary electron emission from the spectrometer surface.**

The axial dependence of the area normalized rate per detector ring is shown, as well as the simulated arrival probabilities for different initial kinetic energies and maximum starting angles respective to the normal vector of the surface. The decreased rate in the first and the last bin is explainable with border effects, as not all electrons emitted in the respective areas of the spectrometer are transported to the detector. This is valid for both, the measurement data and the simulations. The probability distributions for an isotropic emission ( $90^\circ$  starting angle) show no dependence on the initial kinetic energy and do not represent the actual detector data. In the case of a restricted emission cone, the maximum starting angle depends on the kinetic energy range. In order to make the data and the simulation agree, the initial kinetic energy and the maximum starting angle of the simulated secondary electrons appear to anti-correlate.

in the spectrometer. In order to correct this discrepancy, the actual observed area per pixel was calculated, again with KASSIOPEIA field line simulations, and used for the normalization of the detected rates.

The result is the map of the secondary electron emission rate on the central part of the spectrometer, here shown for measurement set B. However, despite the normalization to the observed areas a rate trend in axial direction towards the detector is recognizable. This trend is explainable with the effect of the magnetic mirror depending on the magnetic field at the start position of the electron, which is stronger the closer the starting position gets to the detector, as the Pinch magnet has the biggest influence in this area of the spectrometer. In order to find the impact of the magnetic mirror and to normalize the measured data for the different arrival probabilities per detector ring, particle simulations, using KASSIOPEIA, were performed.

As no information on the initial kinetic energy distribution or the initial momentum direction is known, several simulations on the arrival probability of secondary electrons emitted on the spectrometer surface were performed. Therefore, electrons were created on the surface of a cylinder, corresponding to the observed area in the measurements. In order

to achieve a reasonable computation time, several simplifications were made, such as the neglecting of the inner electrode system and an adiabatic approximation for the trajectory of the electrons. Furthermore, the radius of the cylinder, the electrons are starting on is smaller than the radius of the spectrometer vessel, so the electrons start 10 cm above the real spectrometer surface, but the effects on the results should be small. The initial kinetic energy of the simulated electrons is set in several intervals in the low-energy range, due to expectations on the secondary electron properties. The arrival probability is finally derived from the ratio of electrons arriving on each detector ring and the number of started electrons in the respective area of the spectrometer. For the determination of the starting angle a simple cut in the analysis of the simulated electrons is applied.

In Fig. 6.3 the arrival probability per detector ring, normalized to the entire number of arriving electrons and translated to the respective position in the main spectrometer, for several energy and angular distributions are shown. Obviously, the energy distribution of the simulated electrons does not have an influence on the arrival probability for an isotropic starting angle, as the trend is the same for all simulations. However, the initial starting angle, respective to the normal vector of the spectrometer surface, can be adjusted in such a way that the arrival probability distribution for each energy range can be aligned to the normalized event rate per detector ring. It shows that for higher initial kinetic energies of the simulated electron, the starting angle must be chosen smaller to make the measured rate and the simulated arrival probability agree. Therefore, it is not possible to make a clear statement on the initial momentum direction and, especially, the initial kinetic energy of the secondary electrons.

### 6.3 Spectrometer potential dependence on the secondary electron rate

A series of measurements at different spectrometer potentials was carried out to investigate the impact on the rate of secondary electrons from the spectrometer surface. Therefore, the offset potential of the inner electrode was set to zero. Fig. 6.4 shows the dependence of the measured secondary electron rate to the applied vessel potential. At the nominal vessel potential  $U_{\text{vessel}} = -18.6 \text{ kV}$  the rate is  $R = (666.7 \pm 0.5) \text{ cps}$ . For lower spectrometer potential values the measured rate of the electrons from the surface decreases. One can clearly see that the rate does not depend linearly to the vessel potential, but is suppressed more strongly for lower vessel potentials. For comparison, the arrival probability of electrons on the detector for a comparable setup is simulated. The simulated electrons are starting randomly on a cylinder surface, according to the observed spectrometer section in the measurements and isotropically as no clear statement could be made about the angle in section 6.2.

In order to find a correlation between the vessel potential and the initial kinetic energy of the secondary electrons from the spectrometer surfaces, the simulations were performed for five fixed values ( $-18.6 \text{ kV}$ ,  $-12 \text{ kV}$ ,  $-8 \text{ kV}$ ,  $-4 \text{ kV}$  and  $-2 \text{ kV}$ ). The dependence of the arrival probability on the initial kinetic energy can be explained with the effect of the magnetic mirror. Electrons with low energies more likely pass the Pinch magnet and arrive on the detector. The dependence of the arrival probability on the vessel potential also can be explained with the effect of the magnetic mirror. In this case, the electrons are accelerated at the end of the main spectrometer due to the magnetic field. The resulting additional kinetic energy in axial direction favors electrons to overcome the magnetic mirror. In order to obtain comparable values for the measured rate of secondary electrons and the simulated arrival probability, all values are normalized to the respective value at  $-18.6 \text{ kV}$ . The comparison of the trends for measured data values and the simulated values indicates that the energy of the secondary electrons from the spectrometer surface

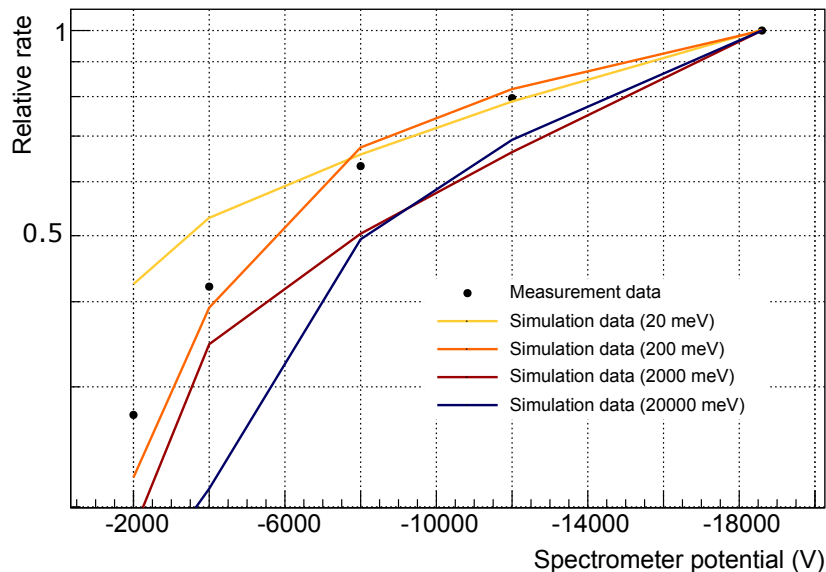


Figure 6.4: **Impact of the spectrometer potential on the measured secondary electron rate.** The measured rate of secondary electrons depends on the vessel potential. Due to the high statistics, the error bars are not visible. Additionally the arrival probability of electrons, simulated with KASSIOPEIA, is plotted. The simulations were carried out for the respective vessel potentials and for four different initial kinetic energies. In the simulation the electrons are started in the respective area observed in the measurements. In order to facilitate the comparison of the data all values are normalized to the respective value for  $U_{\text{vessel}} = -18.6 \text{ kV}$ .

is in the few hundred meV-range. However this only applies insofar as the initial kinetic energy of the electrons is not spread over a wide range, which is expected to be the case.

## 6.4 IE dependence on the secondary electron rate

A series of measurements at different inner electrode offset potentials  $U_{\text{IE}}$  was carried out in order to investigate the impact on the measured rate of secondary electrons from the spectrometer surface. Over the entire measurement period the vessel potential was on a constant value of  $U_{\text{vessel}} = -18.6 \text{ kV}$ . Fig. 6.5 shows the integral and differential measured rate of electrons in dependence on  $U_{\text{IE}}$ . The integral data shows a plateau for the rate trend for low offset potentials and a distinct decrease starting from  $U_{\text{IE}} \approx -200 \text{ mV}$ . The differential spectrum is derived from the integral one by subtracting the value of the next higher IE potential step. It shows a clearly increased rate for electrons in the region from  $U_{\text{IE}} \approx -200 \text{ mV}$  to  $U_{\text{IE}} \approx -4 \text{ V}$  with a maximum at  $U_{\text{IE}} \approx -700 \text{ mV}$ . In contrast to the analysis of the energy of the secondary electrons in the previous sections, this trend indicates higher energies for the secondary electrons. However it must be considered that for this measurements a waveform generator provided the potential on the inner electrode system in order to achieve the required small values. As the system is designed for high voltages and the actually applied voltage could not be read out externally, the accuracy of this measurement is not totally clear and must be considered carefully.

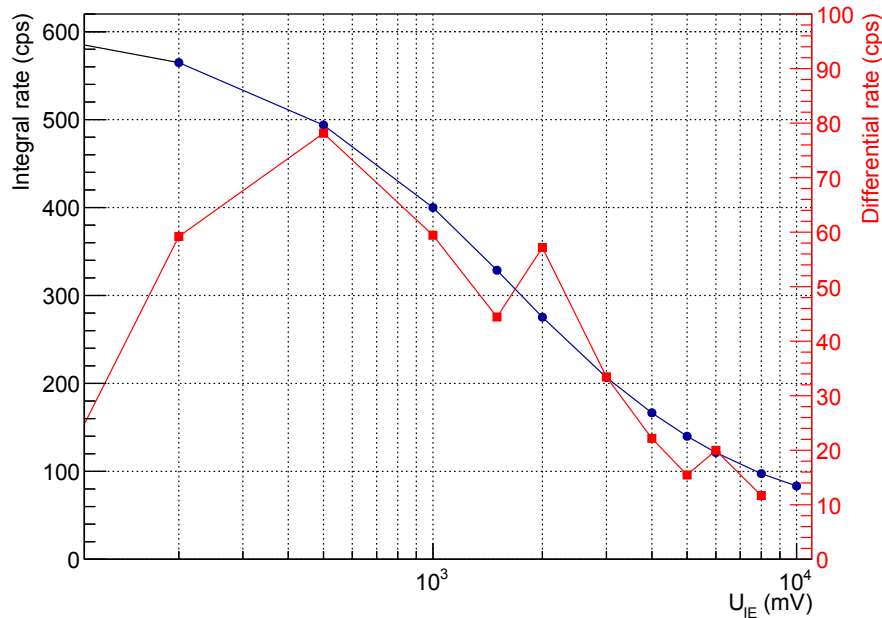


Figure 6.5: **Impact of the inner electrode potential on the measured secondary electron rate.** The blue values represent the measured rate for the respectively set inner electrode offset potential. The red values represent the differential rate spectrum dependent on the offset potential. This can be translated to an energy spectrum of the secondary electrons, as the counter-potential determines the minimum kinetic energies to pass the inner electrode.

## 6.5 Time correlation in secondary electron emission

For a deeper understanding of the characteristics of the secondary electrons the temporal behavior is investigated. Due to the high timing resolution of the detector of about 100 ns [59] a high-precision analysis is possible. In order to find temporal correlations in the secondary electron signal the time between two consecutive detector events is investigated.

### 6.5.1 Identification of time correlated events

Fig. 6.6 shows the distribution of this so-called interarrival times. The exponential distribution above 0.2 ms corresponds to Poisson-distributed single events. For smaller interarrival times a distinct increase in the rate is observed which can be interpreted as the detection of numerous events within short time-scales. These highly correlated events are called cluster events which form, taken together, so-called clusters. In order to characterize these clusters an algorithm was used to separate them from the non-correlated event signal also used in the analysis of the radon induced background [26]. A time-window  $\Delta t$  is defined after each detected event. If there is detected a further event within  $\Delta t$  both belong to the same cluster. This procedure is applied until no further event is detected within  $\Delta t$  whereby the cluster is complete. For the measurements it is found that most of the secondary electrons appear on the detector in clusters. For measurement setting A, the rate for single electrons is  $R_S = 191.9 \pm 0.3$  cps, for cluster events it is  $R_{CE} = 406.8 \pm 0.4$  cps and the rate for clusters itself is  $R_C = 125.9 \pm 0.2$  cps. Therefore, a first approximation yields that the clusters consist of  $C_{\text{Size}} = \frac{R_{CE}}{R_C} = 3.23 \pm 0.01$  events in average.

Due to the relatively small amount of single electrons and the short time window  $\Delta t$  for the cluster search, single electrons accidentally considered as cluster events only play a

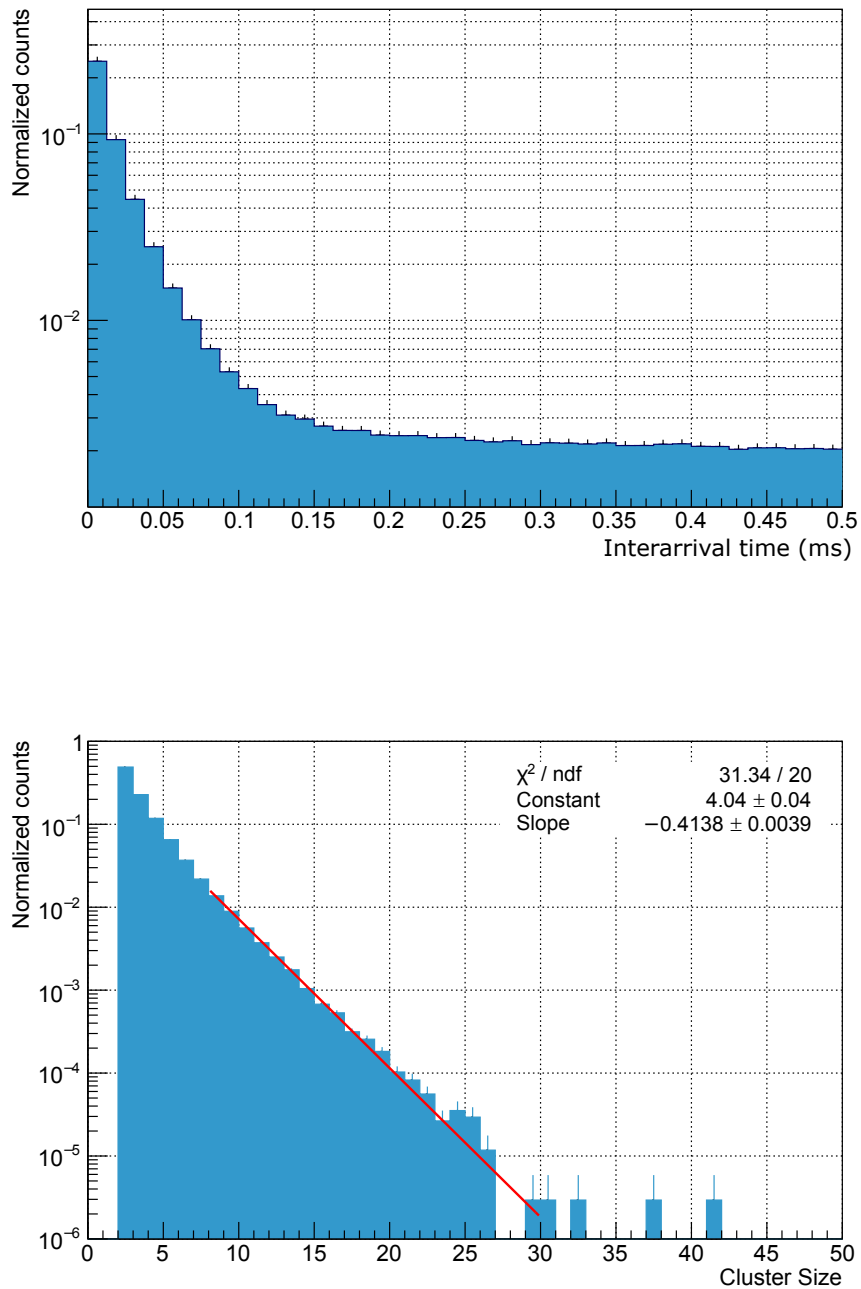


Figure 6.6: **Temporal behavior of the secondary electrons from the spectrometer surface.** **Top:** The interarrival time spectrum of subsequent detector events can be classified in two sections. For times below 0.2ms a non-exponential distribution is found, indicating correlated events. Arrivaltimes larger than 0.2ms appear to be poisson-distributed and therefore, can be classified as uncorrelated. **Bottom:** The number of correlated events within short time-scales, grouped as so-called clusters, shows an exponential behavior, indicating a stochastic selection-process, suppressing larger cluster sizes. This behavior is explainable with the magnetic mirror effect, caused by the Pinch magnet. For smaller cluster sizes the the number of entries does not correspond to the fit, which can be associated with single electrons, accidentally included to a cluster, or a different generation mechanism for the clustered electrons.

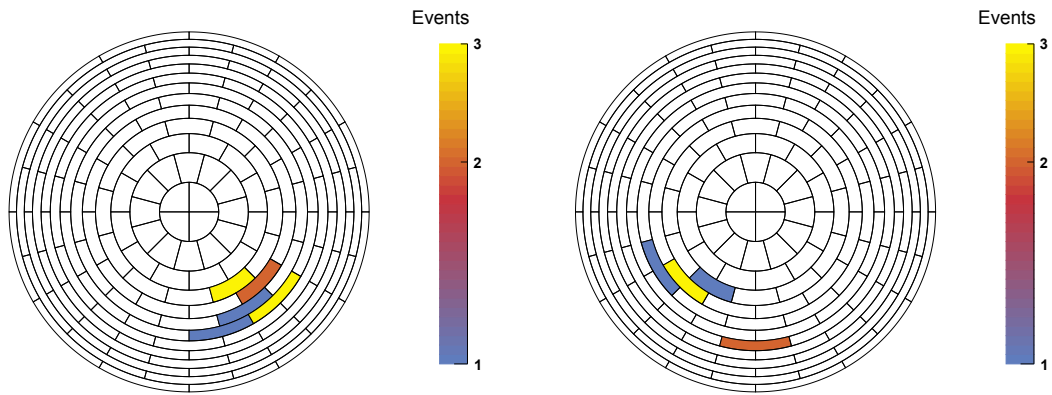


Figure 6.7: **Typical cluster event distribution on the focal plane detector.** Shown are two event distributions on the detector for cluster events with a time-window cut of  $\Delta t = 0.2$  ms. The events are not spread arbitrary on the detector, but grouped in spatially defined patterns. **Left:** Ten cluster events are grouped in one pattern, distributed over five pixels. **Right:** Seven cluster events are grouped in two patterns.

minor role. In Fig. 6.6 the cluster size threshold distribution of the secondary electrons is shown. Surprisingly, there are clusters with sizes of up to 40 events within short time scales. Furthermore, it has to be considered that due to the magnetic mirror effect of the MAC-E filter larger cluster sizes are strongly suppressed. Regarding the pixel distribution of the cluster events on the detector it is apparent that they are not distributed uniformly on the detector, but manifest in spatially confined areas, so-called patterns. Fig. 6.7 shows exemplary the pixel distribution of two clusters with one (a) and two (b) patterns.

### 6.5.2 Axial distribution of single and cluster events in the spectrometer

According to the ring-wise analysis in section 6.2, the same analysis method is used to identify potential characteristics of single and cluster electrons by comparison with simulations. Fig. 6.8 shows the axial distribution of single events, small clusters with cluster size threshold  $N_0 = 2$  and larger clusters with  $N_0 = 8$  in the spectrometer. Although all cluster sizes are considered in the data cut for  $N_0 = 2$ , the small clusters are clearly dominating as seen in Fig. 6.6, so it is reasonable to consider the data as small cluster composed. Apparently the distributions of single electrons and small clusters are similar to the distribution of the total background in Sec.: 6.2. This is quite understandable as both data sets respectively make a large contribution to the total measured background. However the distribution of larger clusters with  $N_0 = 8$  shows a different behavior, as the normalized rate decreases the closer the observed area is located to the detector, which is opposing to the expected trend, determined by the magnetic mirror effect. Although the trend of the simulated arrival probability is determined by the initial angular distribution and kinetic energy, it is not possible to find an appropriate distribution by changing these parameters, indicating that the performed simulations do not totally reflect the real emission conditions of larger clusters. Possible influences might be an increased emission of secondary electron clusters on the upstream side of the spectrometer or a production mechanism for secondary electrons appearing in larger clusters, that is not covered by the performed simulation procedure.

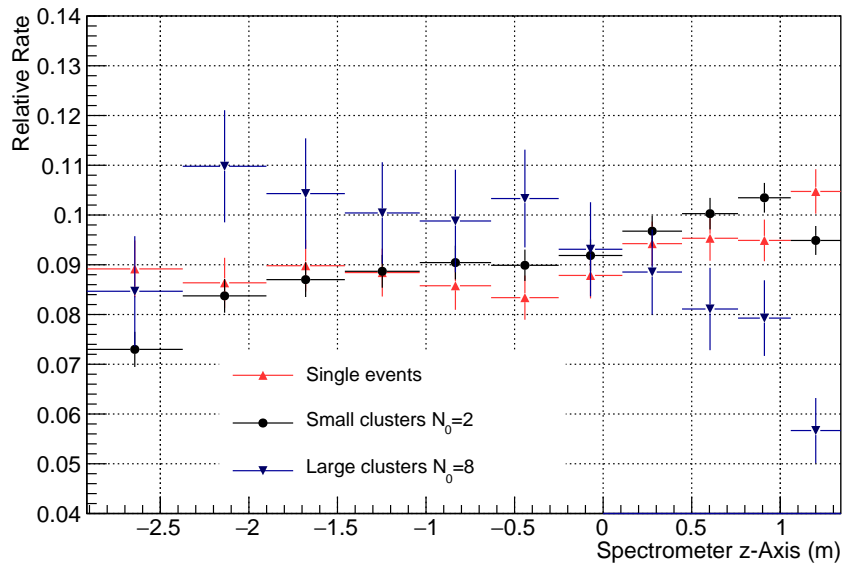


Figure 6.8: **Axial dependence of the emission of single and clustered secondary electron from the spectrometer surface.** According to Fig. 6.3 the axial rate distribution of secondary electrons is shown, respectively for single events and clusters with a cluster size threshold of  $N_0 = 2$  and larger clusters with  $N_0 = 8$ . The decreased rate in the first and the last bin can be explained with boundary effects, however it appears more pronounced for larger clusters. Apparently the distribution of single events and of small clusters follows the distribution of the total rate distribution, which is reasonable, as they are the major contributors as seen in Fig. 6.6. In contrary, the axial rate distribution of larger clusters shows an opposed trend, and is decreasing for locations closer to the detector.

## 6.6 Identification of spatially correlated patterns

Regarding the spatial correlation of the clustered events as shown in Fig. 6.7 a more profound analysis of the cluster characterization is necessary. Therefore, within the context of this work, an analysis algorithm to identify these so-called patterns was implemented. Here, patterns are defined as spatially resolved accumulation of cluster events. The basis of the algorithm is the pre-machined and rehashed event data acquired with the focal plane detector. Therefore, the events are encapsulated to the respective cluster, ordered by the point in time they are detected. The search algorithm processes each cluster separately to identify the contained patterns and to assign each individual event within a cluster to the respective pattern. Analyses of particular clusters showed that the electrons do not arrive consecutively on the detector, but the patterns appear on the detector almost simultaneously. Therefore, it is necessary to consider all events of one cluster, otherwise pattern information might be missed, as shown in the following explanation of the algorithm on the basis of the exemplary event distribution in Fig. 6.9 a).

For each cluster that is analyzed a two-dimensional square array with boolean values  $b_{ij}$  is initialized, with the number of cluster events  $N_0$  as size. Each cluster event  $x$  is allocated to one column. Subsequently, for each cluster event, the algorithm examines all other events  $y$  of the cluster if they are detected on an adjacent or the same pixel of the detector. If applicable, the entry  $b_{xy}$  is set "true", otherwise it is set "false". The result is a symmetric

Table 6.2: **Results of the pattern identification test.** In order to test the propriety and efficiency of the pattern identification algorithm clusters with one to three patterns were created, each pattern consisting of three events on adjacent pixels. The number of one- and two-pattern clusters exceeds the number of created ones clearly. However it can be shown with statistical deliberations that the deviation of about 18 % is totally conform with the allocated input data.

Number of patterns per cluster	created	found	deviation
1	3241	3792	+17 %
2	3394	4039	+19 %
3	3365	2169	-35 %

matrix with "true" entries for  $b_{xy}$ , if event  $x$  and event  $y$  are detected on adjacent or the same detector pixel (Fig. 6.9 b)). The next step is to analyze, if some events are connected to others via an intermediate one, otherwise information on the pattern structure of the cluster might be missed. Therefore, each column  $x$  is scanned for "true" entries. If element  $b_{xa}$  is "true", the entire line  $a$  is scanned for "true" entries. Assumed, element  $b_{ba}$  is found to be "true" it is set to "false" and element  $b_{xb}$  is set true instead (Fig. 6.9 c)). This procedure is continued for all columns, until there are no further changes in the two-dimensional array.

The remaining columns containing "true" elements represent the patterns (Fig. 6.9 d)). As the "true" values only were shifted, the event information, like hit pixel and time of arrival, still can be connected to the initial cluster event. Therefore, detailed information on the pattern distribution like the position on the detector and the temporal characteristics can be calculated.

For the analysis of the patterns, events, without a further event on a adjacent or the same pixel are considered to be accidental single electrons and therefore, are excluded from the analysis. Thus, the event distribution in Fig. 6.9 a) represents a cluster containing two patterns. Regarding data set A, the ratio of the number of patterns depends on the minimum size of the considered clusters. For small multiplicities, clusters with one pattern are dominant. For larger minimum cluster sizes, the amount of two-pattern events increases. Clusters with three or more patterns are strongly suppressed and can be considered as compound of one- and two-pattern clusters.

### 6.6.1 Efficiency of the pattern identification algorithm

In order to examine the efficiency and the reliability of the pattern search algorithm a Monte-Carlo generator was used to produce virtual cluster events with a random number of patterns on the detector. For each pattern, one event on a random detector pixel is chosen and additionally two events on adjacent pixels, so each simulated pattern has a spatial extension of three pixels on the wafer. This data is analyzed with the pattern search algorithm in order to determine the number of patterns found per cluster. The result is shown in Tab. 6.2

The high deviation in the result is explainable with the likelihood that two patterns are generated such that they appear, and are identified by the algorithm, as one pattern. The calculated probability for this case is about 18 %, which perfectly explains both, the increased count of clusters with one and two patterns, as well the reduced count of clusters with three patterns.

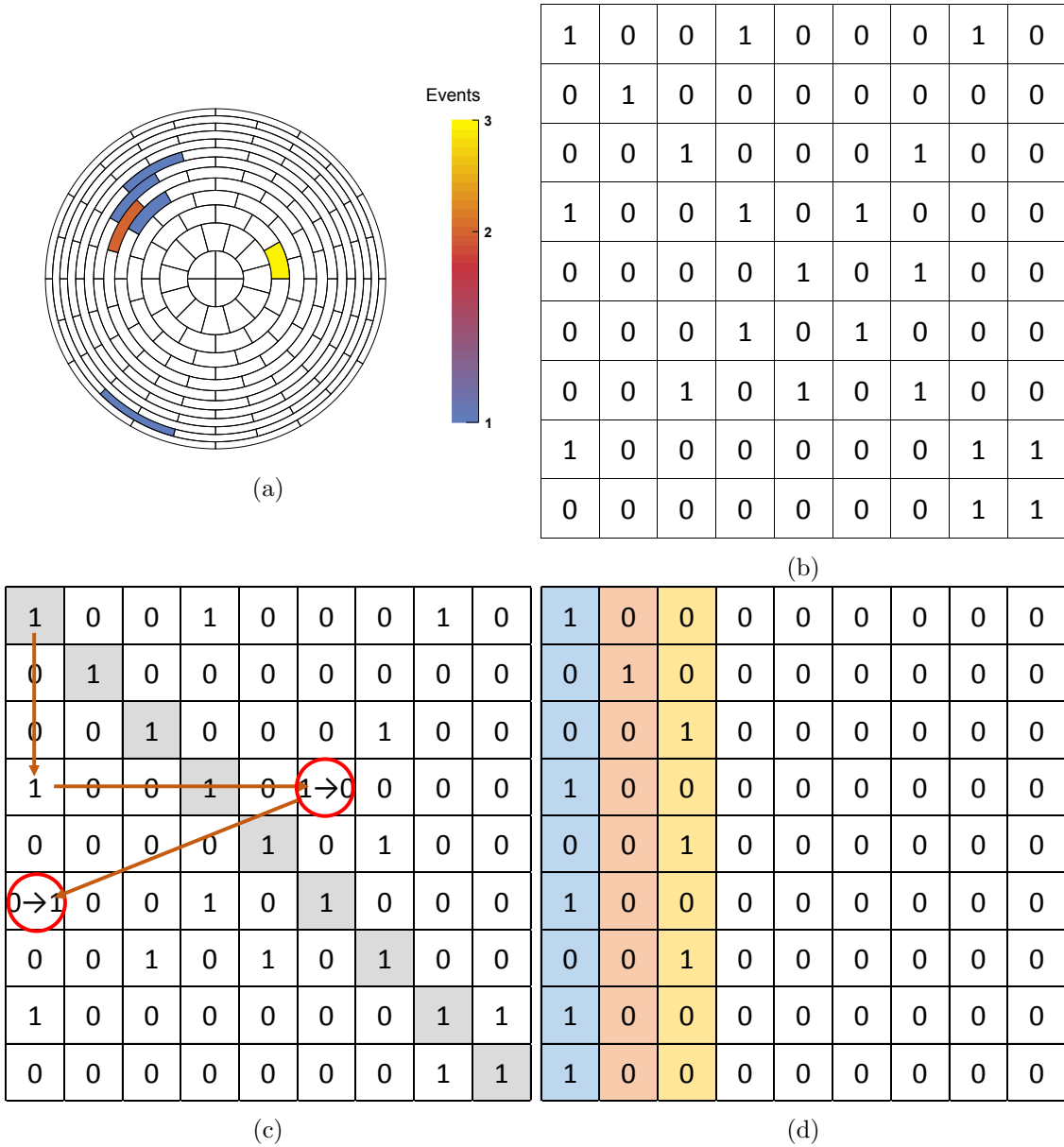


Figure 6.9: **Graphical representation of the pattern identification algorithm.** a)

A typical event distribution of a cluster is shown with spatially defined events. In order to find the exact number of patterns and to allocate the events to the correct pattern a sophisticated algorithm is needed. b) In order to gather every pattern correctly each event must be compared with the other events of the cluster regarding the spatial coherence, realized with a boolean two-dimensional array with  $N_0$  entries. Each line and each column represents an event, sorted by the time of arrival. The algorithm compares all events of the cluster if they are detected on adjacent pixels or on the same pixel and if so the respective entry is set "true", otherwise "false". Self-evidently each element of the main diagonal is "true" and can be neglected in the further analysis. c) In the following the algorithm must find events that are not directly adjacent, but via other events, otherwise the result is not correct. Therefore, in each column the "true" entries are detected and subsequently all "true" elements in the corresponding line. These "true" elements are then transferred to the corresponding entry in the initial column. d) By adopting this procedure to the entire array the entries are arranged in such a way that each column, containing "true" entries represents one pattern with the respective events.

## 7. Possible generation mechanisms of Rydberg atoms on the main spectrometer surfaces

As shown in chapter 5, there are many indications that the remaining background, after countermeasures on the radon background were established, is based on Rydberg atoms. This hypothesis is based on the assumption that Rydberg atoms are generated on the inner surface of the main spectrometer vessel. Until now, this could not be confirmed or disproved and also the production mechanism of the Rydberg atoms is still unknown. In chapter 6 the emission of large clusters of low-energetic electrons from the inner spectrometer surface is described which probably accompany the emission of Rydberg atoms. From theory it is known, that Rydberg atoms are excited by various physical sources. In the case of the KATRIN background, it is assumed, that hydrogen atoms, located at the spectrometer surface in form of a thin water layer, are excited to very high states and emitted into the spectrometer volume. UV-photons and free electrons from field emission in the spectrometer could be excluded very early as production source during measurement phase SDS-IIb.

In the planning phase of KATRIN, secondary electrons emitted by cosmic muons were expected to be the major background source of the experiment. Although this could be excluded in earlier investigations, the possible production of electron clusters and Rydberg atoms is investigated in section 7.1.

A further production mechanism is based on the impact of  $\gamma$ -photons from isotopes in the concrete of the spectrometer hall building. For the investigations massive arrangements were made, like the realization of a water shielding in the basement of the building (section 7.2.1) or reference measurements with a  $^{60}\text{Co}$ -source (section 7.2.2).

The impact of  $^{210}\text{Pb}$ -atoms, implanted into the stainless-steel of the spectrometer, on the production of electron clusters and Rydberg atoms is investigated in section 7.3. First, the description of the implantation and the decay of implanted  $^{210}\text{Pb}$ -atoms is given in subsection 7.3.1. Following, the temporal (subsection 7.3.2) and spatial characteristics (subsection 7.3.3) of the induced secondary electron clusters are investigated. Finally, the identification of the major contributor to the emission of clusters with large multiplicities, and potentially the production mechanism of the Rydberg atoms, in the KATRIN main spectrometer is described in subsection 7.3.4.

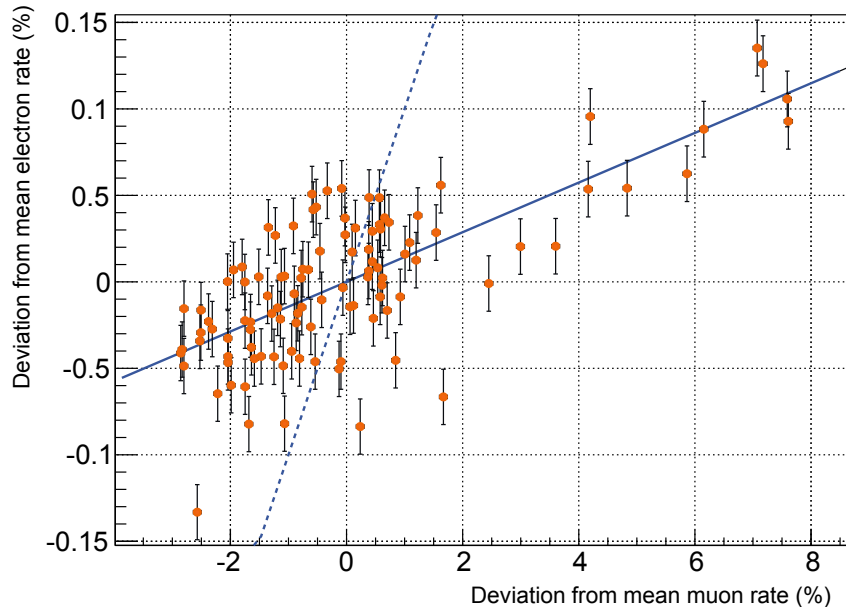


Figure 7.1: **Correlation between the measured muon rate and the total electron rate** for an asymmetric magnetic field setting. The slope of the solid blue line indicates that a fraction of  $a = 14.4 \pm 0.7\%$  of the detected electrons on the detector wafer are muon induced, with a correlation of  $r = 0.72 \pm 0.06$ . The dashed blue line represents the slope for a totally muon induced background. Adapted from [60].

## 7.1 Cosmic muons

Based on the exclusion of radon-induced background after the first SDS measurement phase the remaining dominant background source in the main spectrometer was expected to be secondary electrons from the spectrometer surface induced by cosmic muons. In order to measure the muon flux in the main spectrometer a muon detector system, consisting of nine organic-plastic scintillator modules, was installed on several sites of the spectrometer hall. In combination with spectrometer background measurements the correlation of muon flux and secondary electron rate was investigated explicitly in [60]. It could be shown that muon induced secondary electrons have no direct influence on the measured background signal in the main spectrometer. As part of this thesis, the measurements are reconsidered with the goal to investigate the influence of cosmic muons on the potential production of Rydberg atoms.

The measurement settings for the muon correlation measurements of the spectrometer are comparable to the settings of SDS-IIb regarding the asymmetric magnetic field setting, which covers almost the same area of the spectrometer, and the applied spectrometer potential of  $U_{\text{vessel}} = -18.6 \text{ kV}$ . Relevant differences in the measurements are the higher shielding potential of the inner electrode system and the properties on the inner surface of the spectrometer as there was no vacuum bake-out before the measurements. Additionally, measurements with a symmetric magnetic field were performed according to the 3.8 G-setting in Fig. 5.4.

During measurement phase SDS-IIa a large fluctuation in the muon rate was detected, benefited by a low-pressure system over Karlsruhe. The deviation in the rate of almost 8% enables to perform very precise correlation studies of the muon-induced background. Fig. 7.1 shows the calculated correlation for the measurements with the asymmetric magnetic

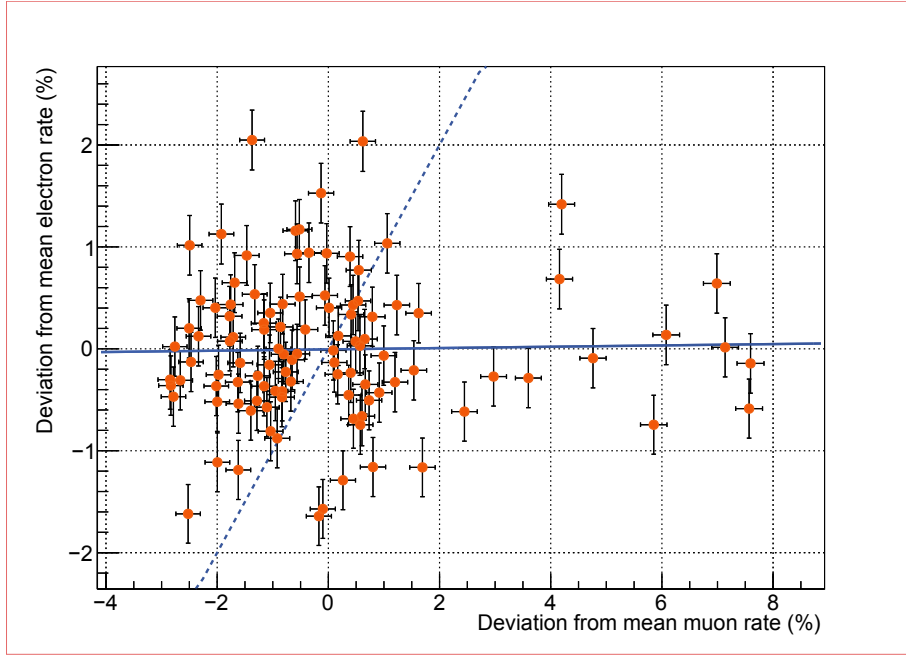


Figure 7.2: **Correlation between the measured muon rate and the clustered electron background rate** with an asymmetric magnetic field setting. For the cluster identification time window of  $\Delta t = 0.2$  ms and a cluster size threshold of  $N_0 = 3$  are used. The slope of the solid blue line indicates a fraction of muon induced, clustered secondary electrons from the spectrometer surface of  $a = 0.7 \pm 1.3$  %. The dashed blue line represents the slope for a totally muon induced background. Adapted from [26].

field setting and  $U_{IE} = -5$  V. For the asymmetric measurements only  $14.4 \pm 0.7$  % of the secondary electrons are induced by cosmic muons, which indicates that there must be a more potent source for secondary emission of electrons from the spectrometer walls. Furthermore, the high kinetic energy of muon-induced secondary electrons to pass the inner electrode offset potential is not compatible with the discoveries in chapter 6, where lower kinetic energies were found. In the case of a symmetric magnetic field setting the influence of muons on the production of Rydberg atoms can be investigated directly. As mentioned in chapter 5 the Rydberg atoms created on the spectrometer surface enter the magnetic flux tube, unaffected by the latter or the electric retarding potential of the inner electrode. Hence, for muon-induced Rydberg atoms, a distinct correlation between the muon rate and the background rate is expected for measurements with a symmetric magnetic field configuration. The correlation factor for these measurements is  $r = -0.01 \pm 0.11$  which is consistent with zero and therefore, muons can be excluded as source of the Rydberg atoms.

Furthermore, a cluster analysis, corresponding to section 6.5, was performed for the respective data of the measurements with an asymmetric magnetic field setting. The correlation plot for the clustered events with  $N_0 = 3$  is shown in Fig. 7.2. The ratio of muon-induced clusters with a minimum cluster size of  $N_0 = 2$  is calculated to  $a = 6.2 \pm 0.9$  %. For larger clusters with  $N_0 = 3$  the ratio decreases to  $a = 0.7 \pm 1.3$  % and therefore, is consistent with zero. Following this trend, muons appear to induce only small clusters of secondary electrons on the spectrometer surface. Regarding the cluster size distribution in Fig. 6.6, there must be a more effective mechanism as source for secondary electron clusters with high multiplicities.

Table 7.1: **Background rates of the measurements with water shielding in the basement of the spectrometer hall.** The measurements were performed with an asymmetric magnet field setting (setting comparable to measurement set C) and no offset potential on the inner electrode system. For the analysis of the measurement two different cluster size thresholds  $N_0$  were applied. The comparison of the respective values shows only a small reduction due to the shielding of  $\gamma$ -photons by the water shielding.

Rate (cps)	$N_0 = 2$			$N_0 = 8$		
	w/o water	w water	red.(%)	w/o water	w water	red.(%)
Total event rate	$625.9 \pm 0.1$	$623.3 \pm 0.1$	0.4	$625.9 \pm 0.1$	$623.3 \pm 0.1$	0.4
Single electron rate	$159.2 \pm 0.1$	$157.8 \pm 0.1$	0.9	$542.93 \pm 0.2$	$540.4 \pm 0.1$	0.5
Cluster event rate	$466.8 \pm 0.1$	$465.4 \pm 0.1$	0.2	$83.0 \pm 0.1$	$82.80 \pm 0.04$	0.2
Cluster rate	$129.2 \pm 0.1$	$128.7 \pm 0.1$	0.4	$8.01 \pm 0.02$	$8.00 \pm 0.01$	0.1

## 7.2 Environmental $\gamma$ -radiation

As mentioned in section 5.3, one excitation mechanism for Rydberg atoms is based on the absorption of photons by an atom. In the case of hydrogen the required photon-energy is in the few eV-Range, which corresponds to UV radiation. Despite very extensive and sophisticated measurements in the spectrometer hall and the vessel itself, no evidence was found for radiation in the respective wavelength range which was observed with a UV PMT, attached to one end of the spectrometer. As opposed to this, a significant rate of  $\gamma$ -photons was detected in the entire building, mainly emitted by the isotope  $^{40}\text{K}$ , which exists in small quantities in the concrete of the spectrometer hall building. Measurements with a CaI-scintillation detector and lab analyses of the used concrete yield an activity of  $A \approx 500 \text{ Bq/m}^3$  of  $\gamma$ -photons. With a penetration probability of about 30 % this results in a rate of 2000 – 3000  $\gamma/\text{s}\cdot\text{m}^3$  from  $^{40}\text{K}$  on the inner surface of the spectrometer.  $^{40}\text{K}$  is a naturally occurring isotope with a half-life of  $1.3 \cdot 10^9$  a that emits photons 1.46 MeV-range. This exceeds the required energy for the excitation of a hydrogen Rydberg atom to a Rydberg state by far [61]. However, the  $\gamma$ -photons might interact with the stainless steel of the main spectrometer, resulting in the production of the highly excited states. For that reason two measurements were performed in order to investigate the influence of  $\gamma$ -radiation on the generation of Rydberg atoms, expected to be expressed in clusters of electrons.

### 7.2.1 Attenuation of $\gamma$ -photons using a water shield

In order to investigate the influence of  $\gamma$ -radiation emitted in the concrete, used in the spectrometer hall, a water shielding was installed in the basement. For this purpose, the oil retention basin below the main spectrometer was filled with 25 t of water, corresponding to an area of  $A_{\square} \approx 140 \text{ m}^2$  and an thickness of  $h = 20 \text{ cm}$ . The attenuation of  $\gamma$ -radiation in the respective energy range can be estimated with a factor of four in this area. Additionally two water bags respectively containing 12.5 t of water were installed on each side of the basin. The bags covered an area of  $A_{\square} \approx 80 \text{ m}^2$  and provided a water column of  $h \approx 60 \text{ cm}$  resulting in an according attenuation factor of 64. In order to investigate the influence of the expected reduced secondary electron rate emitted from the spectrometer surface an asymmetric magnetic field configuration, according to measurement set C, without an offset potential on the inner electrode, was used.

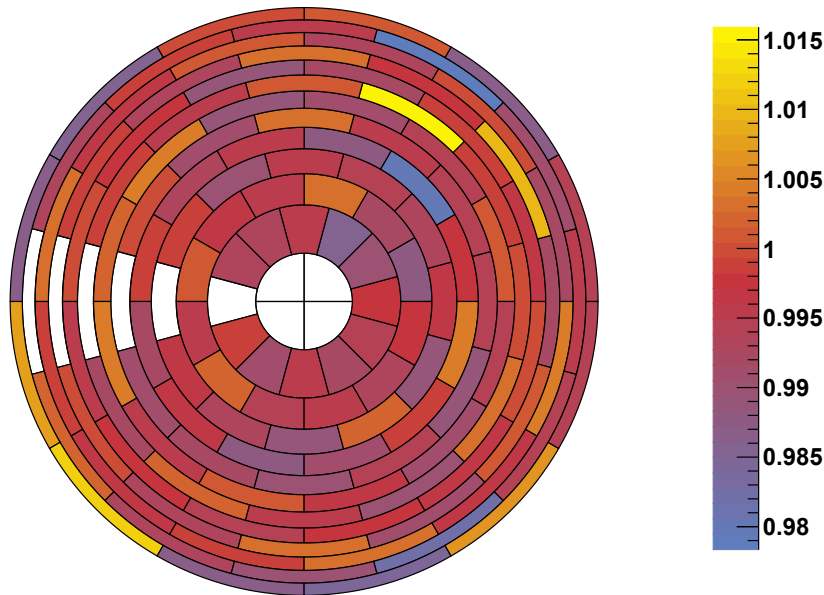


Figure 7.3: **The relative rate change per pixel due to the water shielding** with an asymmetric magnetic field setting shows no significance in any polar direction inside the spectrometer. If the water shielding had a major effect on the production of secondary electrons from the spectrometer surface, a distinct top-bottom discrepancy in the rate would be expected.

The results of the measurements with (runs 25833 - 25843) and without (runs 25864 - 25870) the water shielding below the spectrometer are shown in Tab. 7.1 for two different cluster size thresholds  $N_0$ . No significant differences in the rates are observable in the respective settings with and without the water shielding. Regarding the number of cluster events,  $\gamma$ -radiation appears to induce clusters with small multiplicities, but seems not to be the dominant production mechanism therefore, as the rate reduction, due to the water shielding is very small. Additionally, in Fig. 7.3 the relative rate changes for each pixel are shown for the different analysis settings. The changes in the rate seem to be arbitrary and cannot be connected to the effect of a shielding of  $\gamma$ -photons from the floor. It has to be mentioned that for the basement of the spectrometer hall a special low-radiation concrete was used, resulting in a 40 % lower  $\gamma$ -photon emission in contrast to the walls, built with ordinary concrete. However, a change in the rate, especially for pixels in the lower half of the detector should be visible, if photons from the  $^{40}\text{K}$ -decay had a major influence on the secondary electron emission on the inner surface of the spectrometer [62].

### 7.2.2 Measurements with an $^{60}\text{Co}$ -source

For a better understanding of the influence of  $\gamma$ -radiation on the secondary electron emission and the potentially corresponding Rydberg atom generation an  $^{60}\text{Co}$ -source was installed on several sites in the basement of the main spectrometer building. The source has an activity of about 53 MBq and emits photons with energies of 1.17 MeV and 1.33 MeV. The housing of the  $^{60}\text{Co}$ -source provides a shielding mechanism, which allows to reduce the photon flux by a factor of about 1000. For the measurement setting discussed in the following the source was placed at the axial position of the analyzing plane (between air-coils 8 and 9) of the spectrometer on the west side of the spectrometer basement and the magnetic field configuration is comparable with measurement set A. Due to the geometry and position of the  $\gamma$ -source, about 10 % of the emitted photons hit the spectrometer and about 2 % react with the stainless-steel, corresponding to a rate of about  $10^6$  cps.

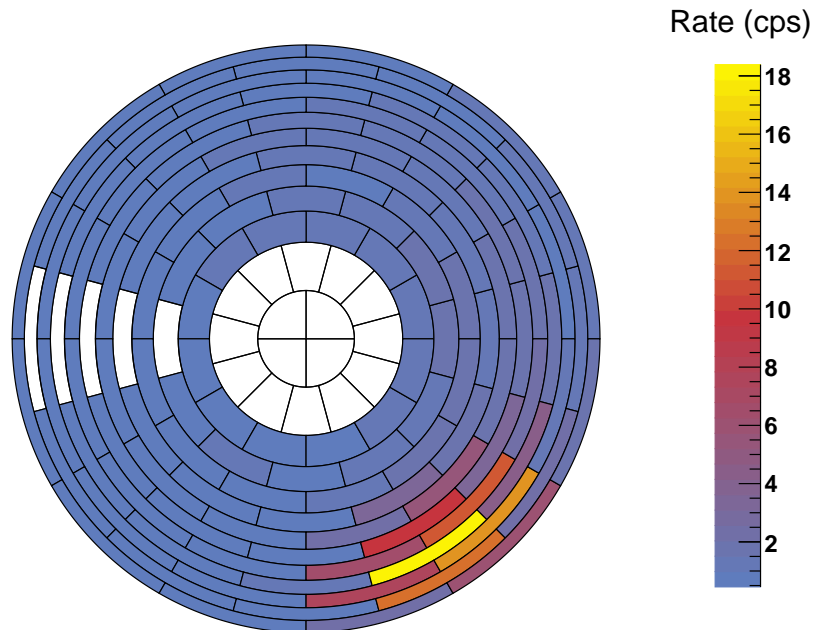


Figure 7.4: **The rate change per detector pixel, induced by a  $^{60}\text{Co}$ -source** shows an increased rate of secondary electrons from the spectrometer surface in the area, the source was located.

Fig. 7.4 shows the rate difference of secondary electrons on the detector for the asymmetric measurement with the source being shielded (run 25557) and unshielded (run 25574). The position of the area with increased electron detection on the detector is clearly visible on the right bottom side of the detector and matches the position of the  $^{60}\text{Co}$ -source in the basement of the building. The influence of the open  $^{60}\text{Co}$ -source corresponds to an additional emission of secondary electrons of  $222.3 \pm 0.7$  cps for an inner electrode potential of  $U_{\text{IE}} = 0$  V (see Tab.: 7.2). An offset potential of  $U_{\text{IE}} = 100$  V on the inner electrode reduces the rate difference to  $26.9 \pm 0.2$  cps (run 25558/25575). In Fig. 7.5 the rates of the respective cluster sizes in the data sets for both, the shielded and the open  $^{60}\text{Co}$ -source is shown and a distinct differences can be seen for small cluster sizes from  $N_0 = 2$  to  $N_0 = 8$ . For larger multiplicities the differences in the rate are very small and contain large statistical errors, indicating that  $\gamma$ -radiation only produces clusters with relatively small cluster sizes, compared to the total cluster size threshold spectrum. The multiplicity analysis of the measurements with  $U_{\text{IE}} = 100$  V shows a similar behavior for small cluster sizes as seen in Fig. 7.5. However, there are no clusters with large sizes observable ( $N_0 > 10$ ), due to the effect of the retarding potential of the inner electrode system.

In Tab. 7.2 the cluster rates for both measurements, with and without a retarding potential on the inner electrode, respectively for an open and a shielded source are shown, as well as the relative rate reduction due to the shielding. In both cases, the reduction is in a similar range, indicating that for the high offset potential the secondary electrons, that arrive on the detector, are emitted at the holding structures of the inner electrode system, which is not electrically shielded. As for this setting no clusters with sizes larger than  $N_0 = 10$  are observable, this result indicates that the emission of large clusters is restricted to the surface of the vessel, excluding the inner electrode system. Furthermore, the limitation to small cluster sizes in both multiplicity distributions, excludes  $\gamma$ -photons as the major contributor to the secondary electron emission, described in the previous chapter.

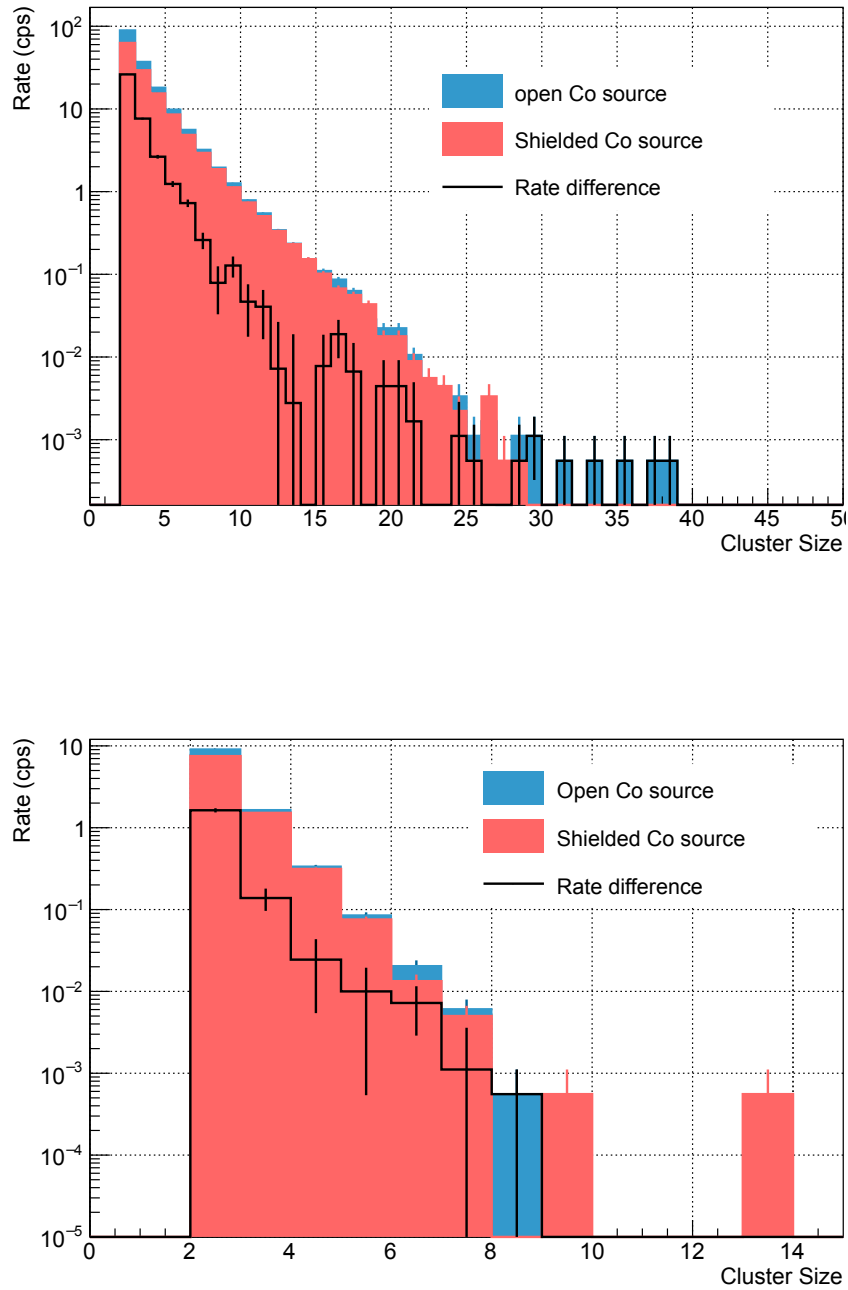


Figure 7.5: **Multiplicity distributions for the measurements with an artificial  $^{60}\text{Co}$ -source.** The clusters are defined by a time window of  $\Delta t = 0.2$  ms. **Top.:** The multiplicity distribution for measurements with no offset potential on the inner electrode is shown. The rate change of the respective cluster sizes, due to the impact of the  $^{60}\text{Co}$ -source is significant up to a threshold of  $N_0 \approx 10$ . **Bottom:** The distribution shows the cluster sizes of the secondary electrons for an inner offset potential of  $U_{\text{IE}} = 100$  V. Compared to the the distribution above, no significant entries for cluster sizes differences larger than  $N_0 \approx 6$  are observable.

Table 7.2: **Background rates of the measurements with a  $^{60}\text{Co}$ -source in the basement of the spectrometer hall** The measurements were performed for two different offset potentials on the inner electrode side, respectively with the source being open or shielded. The clusters are defined by a time window of  $\Delta t = 0.2$  ms and a cluster size threshold of  $N_0 = 2$ . For both settings, a distinct reduction of the rates are observable, indicating a wide energy range of the emitted secondary electrons from the spectrometer surface.

Rate (cps)	IE = 0 V			IE = 100 V		
	open	shielded	red.(%)	open	shielded	red.(%)
Total event rate	$837.9 \pm 0.7$	$615.6 \pm 0.6$	26.5	$91.8 \pm 0.2$	$66.1 \pm 0.2$	27.9
Single electron rate	$316.2 \pm 0.4$	$195.3 \pm 0.3$	38.2	$66.7 \pm 0.2$	$44.8 \pm 0.2$	32.8
Cluster event rate	$521.7 \pm 0.5$	$420.2 \pm 0.5$	19.4	$25.2 \pm 0.1$	$21.3 \pm 0.1$	15.4
Cluster rate	$168.3 \pm 0.1$	$129.1 \pm 0.3$	23.3	$11.2 \pm 0.1$	$9.4 \pm 0.1$	16.1

### 7.3 Intrinsic radiation

As shown in the previous sections, muons and  $\gamma$ -photons are not the major contributors to the secondary electron emission in the main spectrometer as the respectively produced clusters have relatively small sizes, compared to the cluster size distribution in Fig. 6.6. Another production mechanism of secondary electrons might be based on intrinsic radiation, thus the radioactivity of atoms inside the spectrometer. In this section the data from measurement set A, with no offset potential on the inner electrode is discussed.

#### 7.3.1 Deposited radioactive atoms in the main spectrometer

It is known from previous experiments that the long-term exposure of large stainless steel surfaces to ambient air can cause surface-related background due to the amount of radioactive isotopes of radon in the ambient air. In the case of the KATRIN main spectrometer the total stainless steel surface aggregates to  $1240 \text{ m}^2$ , containing the vessel surface, support structures and the inner electrode system. In order to avoid radioactive contamination all surfaces were electropolished after the installation and only high-purity materials were used for the realization of the spectrometer system. However, during the installation of the spectrometer and the inner electrode system, the vessel was exposed to filtered air for more than five years. Due to the ventilation of the spectrometer the total air volume inside the spectrometer was exchanged every 15 to 20 minutes. Based on the activity of  $50 \text{ Bq/m}^3$  and the half-life of 3.8 days of  $^{222}\text{Rn}$ , as well as the spectrometer volume and the air volume exchange due to the ventilation, about  $10^{13}$  decays of  $^{222}\text{Rn}$  can be estimated for the 5-year maintenance inside the spectrometer.

The  $\alpha$ -decay of  $^{222}\text{Rn}$  is followed by several relatively fast  $\alpha$ - and  $\beta$ -decays until  $^{210}\text{Pb}$  is reached in the decay chain, which has a half-life of 22.2 years. Due to several transportation effects, like diffusion, the indirect transportation on aerosols or by electrostatic charges the  $^{222}\text{Rn}$  atoms and its progenies are very likely transported to the surfaces of the main spectrometer vessel, where they are deposited [26]. The  $\alpha$ -decay of  $^{214}\text{Po}$ , located directly on the spectrometer surface, can lead to an implantation of the remaining  $^{210}\text{Pb}$ -nucleus into sub-surface layers of the stainless steel surface of the spectrometer due to the recoil energy of 146 keV. In Fig. 7.6 the implantation profile of these  $^{210}\text{Pb}$ -atoms for an isotropic emission of an  $\alpha$ -particle and the resulting recoil, simulated with the SRIM software package, is shown. The mean implantation depth of the  $^{210}\text{Pb}$ -nuclei is 12.37 nm, but ranges from 0 nm up to 35 nm. The implanted  $^{210}\text{Pb}$ -atoms decay via two  $\beta$ -decays

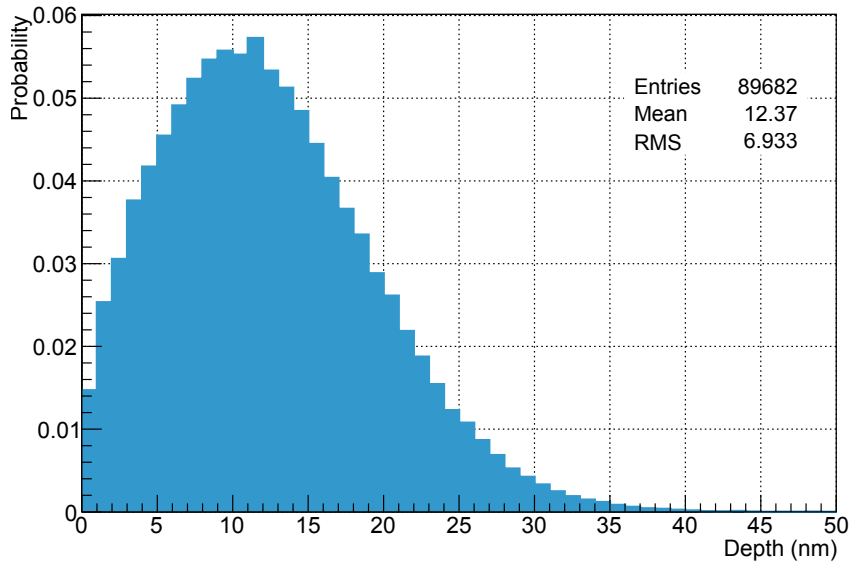


Figure 7.6: **Simulated implantation profile of the  $^{210}\text{Pb}$  recoil nuclei.** The distribution is derived from simulations with the SRIM program package. Therefore,  $^{210}\text{Pb}$ -nuclei were started isotropically on a stainless-steel surface with a recoil kinetic energy, according to the  $\alpha$ -decay of  $^{214}\text{Po}$ .

to  $^{210}\text{Po}$ . Due to the implantation of the emitting atoms, the energy spectrum of the  $\beta$ -electrons should show a blurred energy distribution. These electrons, as well as the expected blurred energy peaks could be observed and analyzed in [26], which is a strong evidence for the implantation theory of  $^{210}\text{Pb}$ -atoms in the surface of the main spectrometer. With a half-life of 138 days  $^{210}\text{Po}$  decays via an  $\alpha$ -decay to the stable  $^{206}\text{Pb}$ . In the following sections, this decay will be investigated with regard to the emission of secondary electrons, especially in clusters.

### 7.3.2 Temporal characteristics of large clusters

In the previous sections, muons and external  $\gamma$ -radiation could be identified with relatively small cluster sizes. In order to exclude these influences from the further analysis, the cluster size threshold is set to  $N_0 = 8$ . Interestingly, the trend of the axial rate in the spectrometer in section 6.5.2 is decreasing for cluster size thresholds  $N_0 \leq 7$  and is not explainable with according simulations. This behavior is a first evidence for a new production mechanism of secondary electrons.

In order to get a better understanding of the characteristics and the origin of the large clusters, the arrangement of the cluster electrons in patterns is investigated. For a cluster size threshold of  $N_0 = 8$ , the rate for single-pattern clusters is  $R_{SP} = 2.52 \pm 0.03$  cps whereas for two-patterns clusters it is  $R_{SP} = 1.18 \pm 0.02$  cps. In order to examine, if the latter are two accidental one-pattern clusters it is assumed that the inter-arrival times are poisson-distributed. With a time window of  $\Delta t = 0.2$  ms the probability for two single-pattern clusters arriving within the time interval  $\Delta t$  is:

$$P = \frac{\int_0^{\Delta t} \exp^{-R_{SP}t} dt}{\int_0^{\text{inf}} \exp^{-R_{SP}t} dt} = 1 - \exp^{-R_{SP}\Delta t} = 0.05\% \quad (7.1)$$

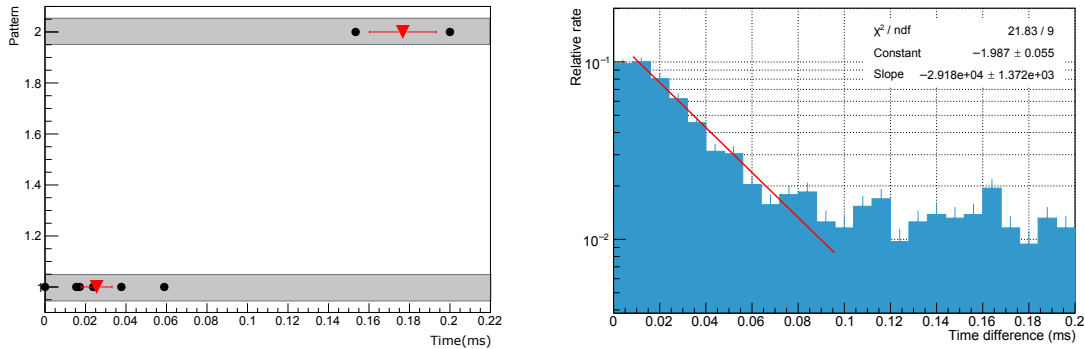


Figure 7.7: **Temporal characteristics of the secondary electron background with larger cluster sizes.** **Left:** The time distribution of the electrons, composing one cluster, is shown, separated for the patterns they belong to. The red triangle shows the temporal barycenter of each pattern. In this case, the patterns arrive on the detector consecutively. However, for other clusters, the arrival times of the patterns may overlap, making it more difficult to determine the first and the second pattern. **Right:** The distribution shows the interarrival time of the two patterns for clusters with a size threshold of  $N_0 = 8$ . The distribution can be separated in two areas, one with an exponential decay up to  $\Delta t \leq 0.1$  ms and a poissonian time distribution for  $\Delta t > 0.1$  ms.

This result indicates an actual mechanism inside the spectrometer generating two correlated patterns of secondary electrons with relatively high multiplicities. In order to get a better understanding of the two-pattern clusters the temporal behavior of detector events will be investigated. On the left side of Fig. 7.7 the typical time distribution for cluster events, including two patterns, is shown. Each point represents one event on the detector, separated for the patterns they arrive in. In this case, the two patterns clearly arrive consecutively on the detector, which is not valid for all clusters, as the respective arrival time ranges may overlap. The points in red represent the calculated temporal barycenter of the arrival times per pattern and they will represent the arrival time of the pattern on the detector in the following analyses. On the right side of Fig. 7.7 the time difference distribution of these two barycenters is shown for all detected two-pattern clusters. Similar to the total inter-arrival time distribution for all electrons in the previous chapter, the distribution can be separated into two sections with different behaviors. For small time differences below  $\Delta t_{patterns} \leq 0.1$  ms a distinct decrease in the relative rate is recognizable, indicating a high correlation between the two patterns. However, for larger time differences, a constant distribution is representing an uncorrelated poissonian behavior.

### 7.3.3 Spatial characteristics of large clusters

In order to find an explanation for the clusters containing two correlated patterns a so-called messenger particle is introduced. It theoretically starts on the surface of the spectrometer, accompanied by the emission of a bunch of secondary electrons. In connection with the theory of the  $\alpha$ -decay of implanted  $^{210}\text{Po}$  the eligible exchange particles are the  $^{206}\text{Pb}$ -nucleus and the emitted  $\alpha$ -particle. In both cases the emission is very likely isotropic and due to the relatively high masses, a linear trajectory in the spectrometer volume can be assumed. After the transition through the spectrometer, the theoretical particle hits

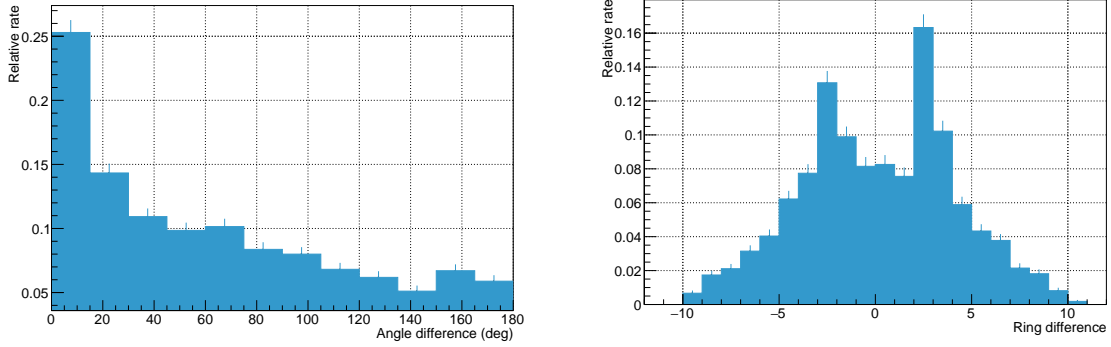


Figure 7.8: **Spatial characteristics of clusters on the detector.** **Left:** The distribution of the polar angle differences of the two patterns on the detector indicates an isotropic emission of the hypothetical messenger particle, except for the larger number of entries in the first bin, which is not conform with the theory. The cause is explained in the text. **Right:** The distribution of the ring differences of the two patterns on the detector confirms the theory of the connection, based on an exchange particle. The increased rates for  $d_R = \pm 2$  are explained in the text.

the surface of the spectrometer and creates another bunch of secondary electrons. In the case that both, the initial and final position of the particle are in the observed area of the spectrometer, the emitted electrons appear as a two-pattern cluster on the detector.

#### Angular distribution of two-pattern events

In order to get a better understanding of the spatial distribution of the pattern inducing events in the spectrometer, the angle and the radius of the patterns on the detector are observed. For the determination, the spatial barycenter of all electrons contained in one pattern is used, similar to the temporal analysis in the previous section. The analysis of two-pattern clusters shows no preferred polar angle (with regard to the center axis) for the initial positions of the two patterns in the spectrometer. Also, the pixel ring distribution on the detector, which represents the axial distribution in the vessel, shows only a small decrease in rate towards rings with larger radii, which is explainable with the effect of the magnetic mirror.

As the observed clusters respectively contain two patterns, also the angular and ring-dependent differences between the two patterns can be observed, as seen in Fig. 7.8. Due to the segmentation of the detector wafer, the bin sizes of the angular distribution are set to  $15^\circ$ . For both distributions distinct inhomogeneities are observable. The shape of the ring-difference distribution is consistent with the theory of a messenger particle, and indicates an emission of the latter with relatively small angles compared to the normal vector of the surface. However, the significantly higher rate for ring differences of  $d_R = \pm 2$  is only explainable in the context with the angular differences of the two patterns. The distribution of the latter shows a distinct increase for small angle differences, whereas the distribution for larger angle differences with  $d_\varphi > 15^\circ$  is consistent with the emission of messenger particles. However, the angle differences of  $0^\circ$  to  $15^\circ$  are not consistent with the theory, as it would imply that the emitted particle hits the spectrometer on a position with the same polar angle, which means that it is guided back to the spectrometer surface. One approach to explain these phenomena is the inner electrode system, which is not considered in the particle simulations. In this explanation, the particle is emitted at

the holding structures of the electrode system, accompanied by the emission of secondary electrons, with direction to the spectrometer surface. Due to the small flight distance of the messenger particle, the two resulting patterns appear close to each other on the detector with only a small angular difference. Patterns with a ring difference of  $d_R = 1$  are considered as a one-pattern cluster and can not be resolved by the pattern search algorithm. A further evidence for this theory is the increased rate of patterns with  $d_R = 2$ , as indicated before. For the further analyses, two pattern clusters with a angle difference of  $d_\varphi < 15^\circ$  are excluded, as they are not comparable to the performed particle simulations and the accuracy on the temporal resolution of the patterns can not be guaranteed.

### Distances between correlated events in the spectrometer

By comparison with simulations, the position on the detector can be translated into spectrometer coordinates and therefore, the distance between the two original locations of the patterns in the spectrometer can be calculated. The distance distributions are shown in Fig. 7.9 whereby the cluster events were separated by the inter-arrival time of the two patterns, according to the results in the previous section. For this purpose, the arithmetic mean of the angle and the radius on the detector for all electrons contained in a pattern is calculated. The first distribution shows the distances between two patterns in the spectrometer vessel that arrive on the detector within  $\Delta t \leq 0.1$  ms, representing time-correlated events. The second distribution represents the distances for temporal uncorrelated events with inter-arrival times of the patterns of  $0.1 \text{ ms} \leq \Delta t \leq 0.2$  ms. Both distributions show a characteristic shape, allowing to distinguish between correlated and uncorrelated events. The rate of clusters inducing correlated patterns is about twice as high as for the uncorrelated patterns, however, for a better comparability, the two distributions are normalized to unity. Both distributions show a characteristic behavior, especially in the region of small distances the correlated events are dominating.

In order to explain the different shapes of the distributions, particle simulations, using KASSIOPEIA, were performed. Expecting a coherence with the  $\alpha$ -decay of the implanted  $^{210}\text{Po}$ -atoms the simulations are adapted accordingly. For this purpose, neutral particles are started randomly on the inner surface of the spectrometer in the area that is observed with the measurements and with an isotropical angle distribution. In order to simulate correlated two-pattern clusters the final position of the simulated particle in the spectrometer is determined and therefore the flight distance of the exchange particle can be calculated. For the distance distribution of two uncorrelated positions on the inner spectrometer surface the distance between two randomly selected points was calculated. The simulation results can also be seen in Fig. 7.9 with the respective distributions from the measurements. For a better comparability they are also normalized to unity. The simulations confirm the idea of an messenger particle, creating the correlated two-pattern clusters, as for both distributions, the simulation results fit very well. In this theory the one-pattern clusters are explainable with exchange particles with only one, either the initial or the final position, in the observed area of the measurements. Based on that, the uncorrelated two-pattern clusters can be explained with two accidental one-pattern clusters. The discrepancy of the measurements and the simulations for distances of  $0 \text{ m} < d < 1.5 \text{ m}$  is based on the fact, that, for correlated events, the respective trajectory is physically not possible, and for uncorrelated events, the two patterns appear on adjacent pixels of the detector and hence, appear as a single-pattern cluster.

#### 7.3.4 Identification of the cluster creating mechanism

As mentioned above, the eligible candidates for the exchange particle, creating the clusters with relatively large sizes, are the products of the decay of  $^{210}\text{Po}$ , the  $^{206}\text{Pb}$ -nucleus and the emitted  $\alpha$ -particle. In theory, both particles can leave the stainless-steel material, the

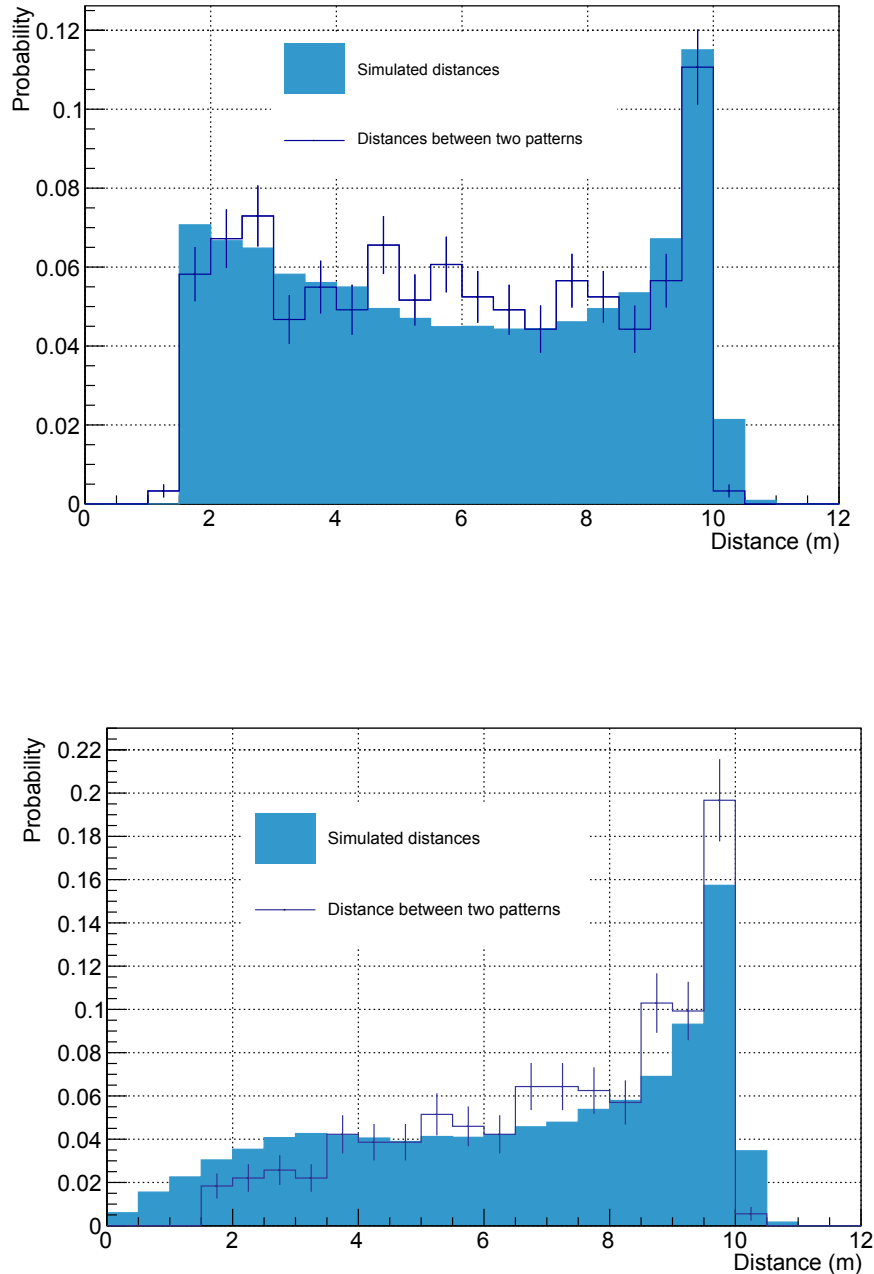


Figure 7.9: **Distance distribution of correlated and uncorrelated patterns in the main spectrometer** The distances are derived by translating coordinates on the detector to spectrometer coordinates by using KASSIOPEIA simulations. **Top:** The measurement data refers to the distance of patterns with  $\Delta t \leq 0.1$  ms. The simulated distances are derived from particles starting on random positions in the spectrometer with an isotropic direction. The length of the linear trajectory of the simulate particles defines the distance. **Bottom:** Here, the distance distribution of patterns with  $\Delta t > 0.1$  ms is shown. The simulated distribution refers to the distance between two randomly selected points on the spectrometer vessel surface.

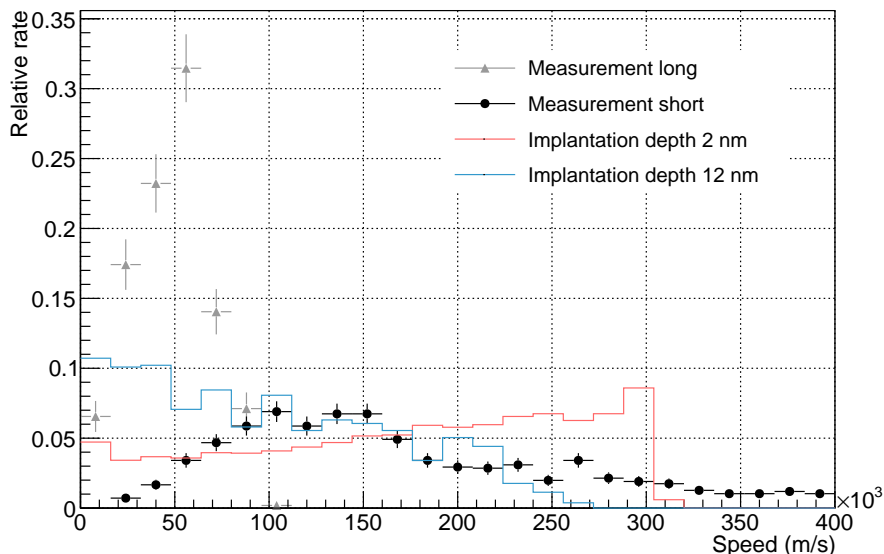


Figure 7.10: **Velocity distribution of the messenger particle.** The distribution shows the velocities of the exchange particle causing two patterns, for correlated (black) and uncorrelated (grey) patterns. Additionally the simulated velocity distribution of  $^{206}\text{Pb}$ , emitted in the  $\alpha$ -decay of  $^{210}\text{Po}$ , is shown. The comparison shows a good agreement for correlated patterns and the simulation with an implantation depth of  $d = 12$  nm for velocities with  $v \geq 100\,000$  m/s. In the case of smaller velocities, some of the events may be cut out due to the limitation on the interarrival time (see section 7.3.2). The simulated distribution for implantation depths of  $d = 2$  nm shows a completely different behavior than the measurement data.

$^{210}\text{Po}$ -atom is implanted in, due to the recoil energy of the decay, accompanied by up to 40 electrons. Derived from the recoil energy  $E_{210\text{Po},\alpha} = 7.59$  MeV the maximum speed of the two particles is:

$$\begin{aligned} v_{\max,^{210}\text{Po}} &\approx 308\,000 \text{ m/s} \\ v_{\max,\alpha} &\approx 15\,860\,000 \text{ m/s} \end{aligned} \quad (7.2)$$

As both, the temporal difference and distance of each pattern-pair is known, the velocity of the causing exchange-particle can be calculated. The velocity distribution is shown in Fig. 7.10 (black points). Here, the cuts from above, on the arrival time between the two patterns and the angle difference on the detector, are applied. The distribution shows a sharp increase with the maximum at  $v_{\max} \approx 150\,000$  m/s and a decrease towards higher velocities, which appears to be exponential. Additionally, the velocities for clusters, with inter-arrival times larger than  $\Delta t_{\text{patterns}} = 0.1$  ms are shown (grey triangles), which are excluded in the other data set. In order to find an evidence for the characteristics of the exchange particle, ion particle simulations were performed, again by using SRIM. For this purpose,  $^{206}\text{Pb}$ -ions were simulated with an initial kinetic energy of  $E_{\text{kin}} = 101.2$  keV (from the decay) and an isotropic emission angle, implanted into stainless-steel with different depths. The respective velocity distributions of the  $^{206}\text{Pb}$ -nuclei, that left the stainless-steel material are also shown in Fig. 7.10. The comparison of the two simulated velocity distributions, with different implantation depths of the decaying  $^{210}\text{Po}$  shows a good agreement with the

velocity distribution for the deeper implantation depth, at least for velocities larger than  $v \approx 100\,000\text{ m/s}$ . For lower velocities the distribution for clusters with larger interarrival times is dominant, indicating that due to the cut from above, concerning this matter, excludes some of the proper cluster events. The maximum velocity of the  $^{206}\text{Pb}$ -nuclei is limited to  $v_{\text{max}} \approx 308\,000\text{ m/s}$  due to the recoil energy from the  $\alpha$ -decay of  $^{210}\text{Po}$ . In the case of implanted nuclei, this maximum speed is reached by nuclei without an inelastic interaction with the stainless-steel material. However, nuclei that experience an energy loss due to an interaction with the solid state have lower velocities, when they enter the vacuum. For most of the observed two-pattern events, the velocity of the exchange particle is below this maximum velocity. This fact, and the shape of the velocity distributions confirm the theory that  $^{206}\text{Pb}$ -nuclei are the messenger particles that cause the clusters of secondary electrons from the spectrometer surfaces with larger cluster sizes, compared to the other investigated production mechanisms in the previous sections.

The atomic impact phenomena on metal surfaces are a well known and a profound investigated field. In [63] it is shown in detail that atoms and ions, hitting a metal surface, induce secondary electrons. The yield of secondary electrons depends on many parameters like, the nature of the impact particle and the target metal, the energy and incident angle of the particle etc. For this reason, it is very conceivable that  $^{206}\text{Pb}$ -nuclei, hitting the spectrometer surface emit numerous secondary electrons. Corresponding to this phenomenon, ions, leaving the metal, should show a similar behavior, also emitting secondary electrons. Considering these observations, the emission of  $^{206}\text{Pb}$ -nuclei appears to be a reasonable model for the explanation of the emission of secondary electrons in larger clusters. However, there are some characteristics that do not fit perfectly.

Apparently, the measurement data is in good agreement with the simulation of  $^{210}\text{Po}$ -nuclei, implanted 12 nm below the stainless-steel surface, whereas the velocity distribution for  $^{210}\text{Po}$ -nuclei, 2 nm below the surface shows no shared characteristics. One explanation for this phenomenon can be the increased energy loss of the emitted  $^{206}\text{Pb}$ -nuclei that are implanted deeper. In [63] it is shown that the yield of secondary electrons decreases for increased energies of the impact particles. In this context,  $^{206}\text{Pb}$ -nuclei, close to the surface, lose only a small amount of kinetic energy, by inelastic scattering with the solid state, and hence induce much less secondary electrons at the surface. For this reason, also  $\alpha$ -particles can be excluded as the dominating mechanism for the production of clustered secondary electrons. Additionally, simulations with the implantation distribution, illustrated in 7.6, were performed. Due to the increased escape probability of nuclei close to the surface, the according velocity distribution is dominated by the latter and shows a similar distribution, as the velocities from simulations with a implantation depth of  $d = 2\text{ nm}$ .

Furthermore, a fraction of the two pattern events indicates exchange particles with higher velocities than the allowed maximum velocity for  $^{206}\text{Pb}$ -nuclei from the  $^{210}\text{Po}$ -decay, with up to  $v \approx 2\,000\,000\text{ m/s}$ . This phenomenon may be explainable with accidental events, that appear as a two-pattern event, or by  $\alpha$ -particles, that lose enough energy in the solid state to cause the emission of secondary electrons at the spectrometer surfaces. Another impact on this behavior can be the sputtered chromium, nickel and iron ions (elements of stainless-steel), which are emitted along with the  $^{206}\text{Pb}$ -nucleus. The simulations showed that about 0.1 sputtered ions are emitted into the vacuum per  $^{206}\text{Pb}$ -nucleus, that leaves the metal surface. However, according to [64], the  $^{206}\text{Pb}$ -nucleus leads to a sputter yield of up to 30 ions with a wide energy range at the end point of the trajectory, where it hits the spectrometer surface again. For a deeper understanding, further simulations will have to be performed.

Finally, the cluster rate compared to the theoretical decay rate of implanted  $^{210}\text{Po}$ -nuclei in the spectrometer is compared. In [26] the decay rate of implanted  $^{210}\text{Po}$ -nuclei is estimated

Table 7.3: **Detected rate of clusters depending on the cluster size threshold  $N_0$**  with a time window of  $\Delta t = 0.2$  ms.

$N_0$	Cluster rate (cps)
5	$13.39 \pm 0.02$
6	$10.33 \pm 0.01$
7	$6.25 \pm 0.01$
8	$5.28 \pm 0.01$
15	$0.203 \pm 0.005$

with  $R = 998 \pm 117$  Bq in the entire spectrometer vessel. The ion simulations from above indicate, that about  $\frac{1}{6}$  of the  $^{206}\text{Pb}$ -nuclei leave the stainless-steel material into the vacuum for the implantation distribution, illustrated in 7.6. With this factor, and the observed area in the measurements, the theoretically observable rate of clusters is:

$$R_{vis} = R \cdot \frac{1}{6} \cdot \frac{A_{obs}}{A_{total}} = 14.4 \pm 1.7 \text{ Bq} \quad (7.3)$$

with  $A_{obs} = 107.7 \text{ m}^2$  as observed surface area in measurement set A and  $A_{total} = 1240 \text{ m}^2$  as the total inner surface of the spectrometer, including the holding structures and the inner electrode system. Regarding only the surface of the vessel ( $A_{total} = 690 \text{ m}^2$ ), the observable rate is  $R_{vis} = 25.9 \pm 3.0$  Bq. Of course, this calculation is only valid for the case, that each  $^{206}\text{Pb}$ -nucleus, leaving the vessel surface, causes the emission of secondary electrons with a sufficient number, that a cluster of electrons can be detected. In Tab. 7.3, the cluster rates for several relatively small cluster size thresholds are shown and they all are in about the same order of magnitude with the theoretically predicted value.

In this section, mainly clusters with a size threshold of  $N_0 = 8$  are investigated, so still no analyses on the very large clusters with sizes up to 30 electrons (see Fig. 6.6) are performed. This is due to the fact, that only a few of this clusters are detected in the measurement runs and therefore, only very poor statistics are given, which do not allow sophisticated analyses. However, the slope of the distribution in Fig. 6.6 suggests that all clusters larger than 8 electrons are generated by the same mechanism, but the magnetic mirror effect of the pinch magnet suppresses larger cluster sizes. In order to that, the cluster characteristics of this section should also be valid for the larger clusters with  $N_0 > 20$ , however a long-term background run should be performed in the upcoming measurement phase to confirm this statement.

## 8. Conclusion

The Karlsruhe TRItium Neutrino (KATRIN) experiment, as a next generation model-independent neutrino mass measurement, aims to determine the mass of the electron antineutrino with a sensitivity of  $m_{\bar{\nu}} \leq 200 \text{ meV}/c^2$ . For this purpose the  $\beta$ -decay spectrum of tritium close to the endpoint at 18.6 keV is precisely investigated. In order to achieve this high precision on the neutrino mass a large scale spectrometer, based on the MAC-E filter principle, is used. Since the electron rate close to the endpoint of the tritium  $\beta$ -spectrum is very low the experiment depends on a very low background rate of 10 mcps.

First background measurements with the KATRIN main spectrometer identified stored electrons from  $\alpha$ -decays of the two radon isotopes  $^{219}\text{Rn}$  and  $^{220}\text{Rn}$ , emitted by the high-performance getter pumps, as one of the major contributors to the background signal of the experimental setup. Due to a sophisticated countermeasure, based on a liquid nitrogen cooled baffle system, the number of radon decays in the sensitive volume of the spectrometer could be reduced to a minimum. Despite this great effort on the background reduction, the remaining level of electrons emitted in the spectrometer vessel still exceeded the design value by far.

In order to find the source of the remaining background signal, detailed measurements were performed. It was found that the remaining background shows a distinct correlation to the conditions of the inner surface of the spectrometer, but is not affected by an offset potential at the inner electrode system. In addition to this, the rate of observed background electrons strongly depends on the flux tube volume inside the spectrometer. One background model combining these properties is based on hydrogen Rydberg atoms. Due to the absorption and adhesion properties of stainless-steel, about  $2 \cdot 10^{15}$  hydrogen atoms per square centimeter are located on the inner spectrometer surface. From theory it is known that Rydberg atoms are excitable by several physical mechanisms such as the impact of ions and electrons or the influence of photons. According to the novel background model, the hydrogen atoms on the vessel surface are excited and emitted into the vacuum of the spectrometer. As they are electrically neutral, they pass the shielding provided by the inner electrode system and the magnet flux tube and enter the volume of the spectrometer, where they are ionized by the black-body radiation of the vessel at 300 K. The emitted electrons are guided to the detector, where they appear in the same energy region of interest as the signal electrons emitted in the tritium decay.

Despite this very detailed model, which could not be confirmed or excluded yet, the production process of the hydrogen Rydberg atoms at the spectrometer surface is unknown.

The main goal of this thesis was to identify potential production mechanisms of Rydberg atoms in the spectrometer and to compare them with the observed background signal. For this purpose, the emission of secondary electrons from the spectrometer surface was investigated, which very likely accompanies the Rydberg production process.

The analysis of the secondary electron emission from the surface revealed, that the electrons are emitted uniformly from the entire vessel surface with energies in the sub-eV to the low eV range. Additionally, it was found that the majority of the electrons arrives on the detector within very short time-scales and therefore, appear as clustered events of electrons with up to 30 events within a few milliseconds. As the spatial distribution of these clusters showed distinct characteristics, a sophisticated algorithm to detect and classify the properties of the electron clusters was implemented. It revealed that a distinct amount of clusters is arranged in spatially defined areas on the detector.

Using the cluster and pattern information of the detected background, several potential sources for the creation of Rydberg atoms were investigated. Due to the large scales of the main spectrometer, cosmic muons, which cross the spectrometer vessel with a very high flux were considered as a very presumable excitation particle for the Rydberg atoms. However, as it turned out they only create clusters with a maximum of two electrons, so they can be neglected.

For the investigation of the influence of  $\gamma$ -photons on the cluster creation of electrons, two temporary experimental setups were installed: the installation of a water shielding in the basement of the spectrometer building and reference measurements with an artificial  $^{60}\text{Co}$ -source. However, the cluster analyses revealed that only clusters with up to eight electrons are induced by  $\gamma$ -photons. Thus, they can not explain the production mechanism of larger clusters, which are associated with the emission of Rydberg atoms.

The investigation of the temporal and spatial characteristics of the clusters that create two patterns on the detector revealed, that a large amount of spatially separated patterns show a distinct time correlation, indicating a single process that induces clusters of electrons at two different locations in the spectrometer vessel. This characteristic behavior could be connected to  $^{206}\text{Pb}$ -nuclei, emitted in the  $\alpha$ -decay of  $^{210}\text{Po}$ , which had been implanted into the stainless-steel of the main spectrometer vessel. This model could be confirmed by the comparison of the theoretical decay rate of the implanted  $^{210}\text{Po}$ -atoms with the cluster rate observed by the detector for larger cluster sizes.

As a final conclusion it can be stated that the decay of implanted  $^{210}\text{Po}$  appears to be the source of clusters with a large number of electrons. As these are also believed to accompany the emission of Rydberg atoms from the spectrometer surface,  $^{210}\text{Po}$  decays are very likely the major source in the novel scenario of background processes in the KATRIN main spectrometer. In order to confirm this theory, a long-term measurement with asymmetric magnetic field settings is suggested, as this allows to investigate large-sized clusters with sufficient statistical accuracy.

# List of Figures

2.1	Flux of solar neutrinos generated in the different fusion processes in the sun	6
2.2	Normal and inverted neutrino mass hierarchy	9
2.3	Schematic neutrinoless double $\beta$ -decay	11
2.4	Schematic single $\beta$ -decay	12
3.1	Illustration of the MAC-E filter principle	14
3.2	Illustration of the KATRIN experiment	15
3.3	The KATRIN transport section components	17
3.4	Illustration of the Focal-Plane Detector system	18
4.1	Overview of the SDS-IIb experimental setup	22
4.2	Observed spectrometer surface areas for the asymmetric magnetic field settings in SDS-IIb	23
4.3	A hotography of a double-layer wire electrode module	25
4.4	A photography of the detector readout electronics in the HV chamber	26
5.1	Schematic drawing of a Penning trap	30
5.2	Trajectory of a stored electron in the KATRIN main spectrometer and the associated characteristic event pattern on the detector	31
5.3	Background rate measured at normal and elevated spectrometer pressure	32
5.4	Dependency of the background rate on the magnetic field strength in the analyzing plane	34
5.5	Influence of the IE offset potential on the measured background rate	35
5.6	Influence of the vacuum bake-out on the background in the main spectrometer	36
6.1	Asymmetric magnetic field setting "Center middle"	40
6.2	Emission of secondary electrons on the inner main spectrometer surface	41
6.3	Axial secondary electron emission from the spectrometer surface	42
6.4	Impact of the spectrometer potential on the measured secondary electron rate	44
6.5	Impact of the inner electrode potential on the measured secondary electron rate	45
6.6	Temporal behavior of the secondary electrons from the spectrometer surface	46
6.7	Typical cluster event distribution on the focal plane detector	47
6.8	Axial dependence of the emission of single and clustered secondary electron from the spectrometer surface	48
6.9	Graphical representation of the pattern identification algorithm	50
7.1	Correlation between the measured muon rate and the total electron rate	52
7.2	Correlation between the measured muon rate and the clustered electron background rate	53
7.3	The relative rate change per detector pixel due to the water shielding	55
7.4	The rate change per detector pixel, induced by a $^{60}\text{Co}$ -source	56
7.5	Multiplicity distributions for the measurements with a $^{60}\text{Co}$ -source	57

7.6	Simulated implantation profile of the $^{210}\text{Pb}$ recoil nuclei . . . . .	59
7.7	Temporal characteristics of the secondary electron background with larger cluster sizes . . . . .	60
7.8	Spatial characteristics of clusters on the detector . . . . .	61
7.9	Distance distribution of correlated and uncorrelated patterns in the main spectrometer . . . . .	63
7.10	Velocity distribution of the messenger particle . . . . .	64

# List of Tables

4.1	Magnet currents of the asymmetric magnetic field settings used in the SDS-IIb measurement phase . . . . .	24
6.1	Measurement settings to characterize the secondary electron emission from the inner spectrometer surface . . . . .	40
6.2	Results of the pattern identification test . . . . .	49
7.1	Background rates of the measurements with water shielding in the basement of the spectrometer hall . . . . .	54
7.2	Background rates of the measurements with a $^{60}\text{Co}$ -source in the basement of the spectrometer hall . . . . .	58
7.3	Detected rate of clusters depending on the cluster size threshold $N_0$ . . . .	66



# Bibliography

- [1] Becquerel, H., “The radio-activity of matter,” *Nature*, vol. 63, no. 1634, pp. 396–398, 1901.
- [2] Chadwick, J., “Intensitätsverteilung im magnetischen Spektrum der  $\beta$ -Strahlen von Radium B+C,” *Verhandlungen der Deutschen Physikalischen Gesellschaft*, vol. 16, pp. 383–391, 1914.
- [3] Pauli, W., “Dear radioactive ladies and gentlemen,” *Phys.Today*, vol. 31N9, p. 27, 1978.
- [4] Chadwick, J., “The existence of a neutron,” *Proceedings of the Royal Society of London A: Mathematical, Physical and Engineering Sciences*, vol. 136, no. 830, pp. 692–708, 1932. [Online]. Available: <http://rspa.royalsocietypublishing.org/content/136/830/692>
- [5] Fermi, E., “Versuch einer Theorie der  $\beta$ -Strahlen. I,” *Zeitschrift für Physik*, vol. 88, no. 3, pp. 161–177, 1934. [Online]. Available: <http://dx.doi.org/10.1007/BF01351864>
- [6] Bethe, H. and Peierls R., “The neutrino,” *Nature*, vol. 133, p. 532, 1934.
- [7] Cowan, C. L. et. al., “Detection of the free neutrino: a confirmation,” *Science*, vol. 124, no. 3212, pp. 103–104, 1956.
- [8] Danby, G. et. al., “Observation of high-energy neutrino reactions and the existence of two kinds of neutrinos,” *Phys. Rev. Lett.*, vol. 9, pp. 36–44, Jul 1962. [Online]. Available: <http://link.aps.org/doi/10.1103/PhysRevLett.9.36>
- [9] Perl, M. L. et. al., “Evidence for anomalous lepton production in  $e^+ - e^-$  annihilation,” *Phys. Rev. Lett.*, vol. 35, pp. 1489–1492, Dec 1975. [Online]. Available: <http://link.aps.org/doi/10.1103/PhysRevLett.35.1489>
- [10] Higgs, P. W., “Broken symmetries and the masses of gauge bosons,” *Phys. Rev. Lett.*, vol. 13, pp. 508–509, Oct 1964. [Online]. Available: <http://link.aps.org/doi/10.1103/PhysRevLett.13.508>
- [11] Povh et. al., *Teilchen und Kerne: Eine Einführung in die physikalischen Konzepte*, 8th ed. Berlin: Springer Berlin, 2008.
- [12] Wu, C. S. et. al., “Experimental test of parity conservation in beta decay,” *Phys. Rev.*, vol. 105, pp. 1413–1415, Feb 1957. [Online]. Available: <http://link.aps.org/doi/10.1103/PhysRev.105.1413>
- [13] The ALEPH Collaboration et. al., “Precision electroweak measurements on the  $Z$  resonance,” *Physics Reports*, vol. 427, no. 56, pp. 257 – 454, 2006. [Online]. Available: <http://www.sciencedirect.com/science/article/pii/S0370157305005119>
- [14] Pontecorvo, B., “Inverse beta processes and nonconservation of lepton charge,” *Sov. Phys. JETP*, vol. 7, pp. 172–173, 1958.

- 
- [15] Bahcall, John N., “Solar neutrinos. i. theoretical,” *Phys. Rev. Lett.*, vol. 12, pp. 300–302, Mar 1964. [Online]. Available: <http://link.aps.org/doi/10.1103/PhysRevLett.12.300>
- [16] Davis, R. D. et. al., “Search for neutrinos from the sun,” *Phys. Rev. Lett.*, vol. 20, pp. 1205–1209, May 1968. [Online]. Available: <http://link.aps.org/doi/10.1103/PhysRevLett.20.1205>
- [17] W. Hampel et. al., “Gallex solar neutrino observations,” *Physics Letters B*, vol. 447, no. 12, pp. 127 – 133, 1999. [Online]. Available: <http://www.sciencedirect.com/science/article/pii/S0370269398015792>
- [18] John N. Bahcall and Aldo M. Serenelli and Sarbani Basu, “New solar opacities, abundances, helioseismology, and neutrino fluxes,” *The Astrophysical Journal Letters*, vol. 621, no. 1, p. L85, 2005. [Online]. Available: <http://stacks.iop.org/1538-4357/621/i=1/a=L85>
- [19] Smirnov, O. et. al., “Solar neutrino with borexino: Results and perspectives,” *Physics of Particles and Nuclei*, vol. 46, no. 2, pp. 166–173, 2015.
- [20] Schmitz, N., *Neutrino Physik*, ser. Teubner Studienbücher Physik. Wiesbaden: Vieweg+Teubner Verlag, 1997. [Online]. Available: <http://dx.doi.org/10.1007/978-3-322-80114-2>
- [21] Iizuka et. al., “Parametrization of pontecorvo-maki-nakagawa-sakata mixing matrix based on cp-violating bipair neutrino mixing,” *Modern Physics Letters A*, vol. 30, no. 05, p. 1550019, 2015.
- [22] Mikheyev, S. P. and Smirnov, A. Yu., “Resonant amplification of  $\nu$  oscillations in matter and solar-neutrino spectroscopy,” *Il Nuovo Cimento C*, vol. 9, no. 1, pp. 17–26, 1986. [Online]. Available: <http://dx.doi.org/10.1007/BF02508049>
- [23] Foot, R. and Volkas, R. R. and Yasuda, O., “Testing maximal electron and muon neutrino oscillations with sub-gev superkamiokande atmospheric neutrino data,” *Phys. Rev. D*, vol. 57, pp. R1345–R1349, Feb 1998. [Online]. Available: <http://link.aps.org/doi/10.1103/PhysRevD.57.R1345>
- [24] Elsener et. al., *The CERN neutrino beam to Gran Sasso (NGS): conceptual technical design*. Geneva: CERN, 1998. [Online]. Available: <http://cds.cern.ch/record/359028>
- [25] An et. al., “Observation of electron-antineutrino disappearance at daya bay,” *Phys. Rev. Lett.*, vol. 108, p. 171803, Apr 2012. [Online]. Available: <http://link.aps.org/doi/10.1103/PhysRevLett.108.171803>
- [26] Harms, F., “Characterization and minimization of background processes in the katrin main spectrometer,” 2015, dissertation, Karlsruhe Institute of Technology.
- [27] Lesgourgues, J. and Pastor, S., “Neutrino cosmology and planck,” *New Journal of Physics*, vol. 16, no. 6, p. 065002, 2014. [Online]. Available: <http://stacks.iop.org/1367-2630/16/i=6/a=065002>
- [28] Hirata, K. S. et. al., “Observation in the kamiokande-ii detector of the neutrino burst from supernova sn1987a,” *Phys. Rev. D*, vol. 38, pp. 448–458, Jul 1988. [Online]. Available: <http://link.aps.org/doi/10.1103/PhysRevD.38.448>
- [29] Loredo, T. J. and Lamb, D. Q., “Bayesian analysis of neutrinos observed from supernova sn 1987a,” *Phys. Rev. D*, vol. 65, p. 063002, Feb 2002. [Online]. Available: <http://link.aps.org/doi/10.1103/PhysRevD.65.063002>

- [30] Majorana, E. and Maiani, L., “Ettore majorana scientific papers: On occasion of the centenary of his birth,” pp. 201–233, 2006.
- [31] Agostini, M. et. al., “Results on neutrinoless double- $\beta$  decay of  $^{76}\text{Ge}$  from phase i of the gerda experiment,” *Phys. Rev. Lett.*, vol. 111, p. 122503, Sep 2013. [Online]. Available: <http://link.aps.org/doi/10.1103/PhysRevLett.111.122503>
- [32] Phillips II, D. G. et. al., “The majorana experiment: an ultra-low background search for neutrinoless double-beta decay,” *Journal of Physics: Conference Series*, vol. 381, no. 1, p. 012044, 2012. [Online]. Available: <http://stacks.iop.org/1742-6596/381/i=1/a=012044>
- [33] Dirac, P. A. M., “The quantum theory of the emission and absorption of radiation,” *Proceedings of the Royal Society of London A: Mathematical, Physical and Engineering Sciences*, vol. 114, no. 767, pp. 243–265, 1927. [Online]. Available: <http://rspa.royalsocietypublishing.org/content/114/767/243>
- [34] Otten, E.W., “The mainz neutrino mass experiment,” *Progress in Particle and Nuclear Physics*, vol. 32, pp. 153 – 171, 1994. [Online]. Available: <http://www.sciencedirect.com/science/article/pii/0146641094900167>
- [35] Aseev, V. N. et. al., “Measurement of the electron antineutrino mass in tritium beta decay in the troitsk nu-mass experiment,” *Physics of Atomic Nuclei*, vol. 75, no. 4, pp. 464–478, 2012. [Online]. Available: <http://dx.doi.org/10.1134/S1063778812030027>
- [36] Olive, K. A. et. al., “Review of Particle Physics,” *Chin. Phys.*, vol. C38, p. 090001, 2014.
- [37] Angrik, J. et. al., “Katrin design report,” 2004, fZKA-7090.
- [38] Wolf, J., “The katrin neutrino mass experiment,” *Nuclear Instruments and Methods in Physics Research Section A: Accelerators, Spectrometers, Detectors and Associated Equipment*, vol. 623, no. 1, pp. 442 – 444, 2010, 1st International Conference on Technology and Instrumentation in Particle Physics.
- [39] Wandkowsky, N., “Study of background and transmission properties of the katrin spectrometers,” 2013, dissertation, Karlsruhe Institute of Technology.
- [40] “Katrin beamline,” datum: 06.03.2014. [Online]. Available: [http://fuzzy.fzk.de/bscw/bscw.cgi/d833092/Beamline%20kp\\_2\\_29.08.2013.jpg](http://fuzzy.fzk.de/bscw/bscw.cgi/d833092/Beamline%20kp_2_29.08.2013.jpg)
- [41] Babutzka, M. et. al., “Monitoring of the operating parameters of the katrin windowless gaseous tritium source,” *New Journal of Physics*, vol. 14, no. 10, p. 103046, 2012.
- [42] Schloesser, M. et. al., “Accurate calibration of the laser raman system for the karlsruhe tritium neutrino experiment,” *Journal of Molecular Structure*, no. 0, pp. 761 – 66, 2013.
- [43] Lukic, S. et. al., “Measurement of the gas-flow reduction factor of the katrin dps2-f differential pumping section,” *Vacuum - Surface Eng., Surface Instr. and Vacuum Techn.*, vol. 86, pp. 1126 – 1133, 2012.
- [44] Gil, W. et. al., “The Cryogenic Pumping Section of the katrin Experiment,” *IEEE Trans. on app. supercond.* 3, vol. 20, pp. 316 – 319, 2010.
- [45] Sturm, M., “Aufbau und test des inner-loop-systems der tritiumquelle von katrin,” 2007.
- [46] Fraenkle, F.M. et. al., “Radon induced background processes in the KATRIN pre-spectrometer,” *Astroparticle Phys. Issue 3*, vol. 35, pp. 128 – 134, 2011.

- 
- [47] Beglarian, A. et. al., “Prototype focal-plane detector system for the katrin experiment,” 2012.
- [48] Howe, M. et. al., “Sudbury Neutrino Observatory Neutral Current Detector Acquisition Software Overview,” *IEEE Trans. Nucl. Sci.*, vol. 51, pp. 878–883, 2004.
- [49] Arenz, M. et. al., “Commissioning of the vacuum system of the katrin main spectrometer,” *Journal of Instrumentation*, vol. 11, no. 04, p. P04011, 2016. [Online]. Available: <http://stacks.iop.org/1748-0221/11/i=04/a=P04011>
- [50] Harms, F., “Assembly and first results of the katrin focal-plane detector system at kit,” 2012, diploma thesis, Karlsruhe Institute of Technology.
- [51] Schwarz, J., “The detector system of the katrin experiment - implementation and first measurements with the spectrometer,” 2014, dissertation, Karlsruhe Institute of Technology.
- [52] Glück, F. and Drexlin, G. et. al., “Electromagnetic design of the large-volume air coil system of the KATRIN experiment,” *New Journal of Physics*, vol. 15, no. 8, p. 083025, 2013.
- [53] Adams, B., “Untersuchung magnetischer materialien und inbetriebnahme der magnetfeldüberwachung am katrin-hauptspektrometer,” 2015.
- [54] Erhard, M. et. al., “Technical design and commissioning of the katrin large volume air coil system,” 2016, in preparation.
- [55] “Agilent 34401a arbitrary waveform generator,” Datum: 13.05.2016. [Online]. Available: <http://www.keysight.com/en/pd-127539-pn-33220A/function-arbitrary-waveform-generator-20-mhz?cc=DE&lc=ger>
- [56] Fraenkle, F., “Background investigations of the katrin pre-spectrometer,” 2010, dissertation, Karlsruhe Institute of Technology.
- [57] Gallagher, T. F., *Rydberg atoms*, digitally print. 1. pbk version ed., ser. Cambridge monographs on atomic, molecular, and chemical physics. Cambridge: Cambridge Univ. Press, 2005, vol. 3.
- [58] Drexlin, G., “Excited molecules and atoms as background source,” 2016, internal KATRIN talk. [Online]. Available: <http://fuzzy.fzk.de/bscw/bscw.cgi/d950495/95-TRP-5833-D1.3-GDrexlin.pptx>
- [59] Amsbaugh, J.F. et. al., “Focal-plane detector system for the KATRIN experiment,” *Nuclear Instruments and Methods in Physics Research Section A: Accelerators, Spectrometers, Detectors and Associated Equipment*, vol. 778, pp. 40–60, 2015.
- [60] Linek, J., “Investigation of the muon induced background at the katrin main spectrometer,” 2015, master thesis, Karlsruhe Institute of Technology.
- [61] Engelkemeir, D. W. and Flynn, K. F. and Glendenin, L. E., “Positron emission in the decay of  $K^{40}$ ,” *Phys. Rev.*, vol. 126, pp. 1818–1822, Jun 1962. [Online]. Available: <http://link.aps.org/doi/10.1103/PhysRev.126.1818>
- [62] Wolf, J., “Gamma flux levels with water shielding,” 2015, internal KATRIN talk, 29th collaboration meeting. [Online]. Available: <https://fuzzy.fzk.de/bscw/bscw.cgi/d973608/95-TRP-5928-B2-JWolf.pptx>
- [63] Kaminsky, M., *Atomic and ionic impact phenomena on metal surfaces*. Heidelberg: Springer Verlag, 1965.
- [64] Osipowicz, A., “Srim simulations on pb-206 from po-210 decay,” 2016, internal KATRIN talk, 30th collaboration meeting. [Online]. Available: <https://fuzzy.fzk.de/bscw/bscw.cgi/d1007906/95-TRP-6025-S4-AOsipowicz.pdf>

# Danksagung

Abschließend möchte ich mich ganz herzlich bei allen bedanken, die mich im letzten Jahr begleitet und zum Gelingen meiner Masterarbeit beigetragen haben. Ein ganz besonderes Dankeschön gebührt hierbei folgenden Personen.

- Prof. Dr. G. Drexlin dafür, dass ich meine Masterarbeit bei KATRIN schreiben durfte und für die vielen interessanten Diskussionen, die diese Arbeit bereichert haben.
- Prof. Dr. U. Husemann dafür, dass er freundlicherweise das Korreferat übernommen hat.
- Dr. Fabian Harms für eine ausgezeichnete Betreuung, viele aufschlussreiche Diskussionen und spannende und lehrreiche drei Jahre bei KATRIN.
- Dr. Florian Fränkle für die vielen interessanten Diskussionen und die großartige Zusammenarbeit im Büro und während der Messphase.
- Thank you Prof. Dr. Peter Doe and Prof. Dr. Sanshiro Enomoto for giving me the opportunity to stay at CENPA for several weeks and for the great time I spent in Seattle.
- Dr. Bianca Keilhauer, stellvertretend für das i-Progress Programm, für die finanzielle Unterstützung während meines Aufenthalts in den USA.
- Dr. Stephan Groh, Dr. Marco Kleesiek, Nicolaus Trost und Florian Heizmann dafür, dass ich mit allen computer- und programmierspezifischen Fragen zu ihnen kommen durfte und mir stets hervorragend geholfen wurde.
- Allen Technikern, Doktoranden, Postdocs und weiteren beteiligten Personen, die für eine reibungslose und aufschlussreiche Messphase in den heißen Sommermonaten gesorgt haben.
- Moritz Erhard für die Gesellschaft während der Schreibphase, die Hinweise bei der Illustration dieser Arbeit und vor allem für das geteilte Leid im Abstiegskampf.
- Prof. Dr. Peter Doe, Dr. Joachim Wolf, Dr. Florian Fränkle, Dr. Fabian Harms, Hendrik Seitz- Moskaliuk, Carsten Röttele und Kilian Dengler für die ausführlichen und hilfreichen Kommentare, die zum Gelingen dieser Arbeit beigetragen haben.
- Allen, die in den letzten Jahren Kuchen mitgebracht, Pizza bestellt und geholt und für Kaffee gesorgt haben.

Ein besonderer Dank gilt meiner Familie, die mir das Physikstudium ermöglicht hat und zu jeder Zeit ein starker Rückhalt ist.

Abschließend möchte ich der wunderbaren Angelika Jochim danken, die immer für mich da ist und mich während des gesamten Studiums großartig unterstützt hat.